NOTE TO USERS

COMPARATIVE STUDY OF MEGAVOLTAGE IMAGING MODALITIES FOR DOSIMETRIC TREATMENT VERIFICATION

LALITH K. KUMARASWAMY

Medical Physics Unit
McGill University, Montreal
August 2003

A thesis submitted to the Faculty of Graduate Studies and Research in partial fulfillment of the requirements of the Degree of Master of Science in Medical Radiation Physics

Your file Votre référence
ISBN: 0-612-98676-4
Our file Notre référence
ISBN: 0-612-98676-4

Abstract

In this work, various megavoltage imaging modalities such as the Portal Vision aS-500 Amorphous Silicon EPID, Portal Vision LC-250 Liquid Matrix EPID, PortPro Flouro based EPID, Kodak XV film, Kodak EDR film, and SmartCR Computer Radiography system are examined in terms of detector parameters (acquisition time, minimum dose to obtain an image, saturation dose, and grey scale) and image quality parameters (subject contrast, signal-to-noise ratio, spatial resolution, modulation transfer function, and gantry angle dependence). We found that aS-500 EPID provides better image quality as compared to the other modalities investigated in terms of quantitative parameters. Qualitatively, it also outperformed the other systems, although the differences in image quality between the systems were sometimes marginal. The fast acquisition time and the requirement of only 1 MU to generate an image also made aS-500 EPID the most appropriate imager for static IMRT dose verification. The isodose comparison between the aS-500 EPID and Kodak XV film for several IMRT QA studies corresponded within acceptable tolerance levels of ± 2 mm in most cases.

Résumé

Lors de cette étude, nous avons approfondi le fonctionnement de plusieurs appareils d'imagerie en mégavoltage telles que le Portal Vision aS-500 Amorphous Silicon EPID, le Portal Vision LC-250 Liquid Matrix EPID, le PortPro Flouro based EPID, le film Kodak XV, le film Kodak EDR et le SmartCR Computer Radiography system. Ces dispositifs utilisés pour vérifier le traitement furent étudiées en leurs paramètres de détection (temps d'acquisition, nombre minimal de MU afin d'obtenir une image, dose de saturation et échelle grise) et leurs paramètres de qualité d'image (contraste du sujet, rapport signal-bruit-de-fond et dépendance de l'angle du portique). Cette étude confirme que le aS-500 EPID est l'appareil qui fournit la meilleure qualité d'image comparativement aux autres dispositfs étudiés. La rapidité d'acquisition et le nombre minimal de 1 MU pour obtenir une image font en sorte que le aS-500 EPID est un dispositf d'imagerie idéal pour la vérificatrion de dose en radiothérapie par intensité modulée (IMRT). La comparasion d'isodoses entre le aS-500 EPID et le film Kodak XV pour plusieurs études d'IMRT correspondent à l'intérieur d'assurance de qualité d'un niveau de tolerance acceptable de ± 2 mm dans la plus part des régions du champ.

Acknowledgments

I am grateful and indebted for having the opportunity to work under the supervision of Mr. William Parker. Thank you for your patience and giving me the freedom to work independently. Your good sense of humour, guidance during my thesis writing, and advises related to the field of medical physics are invaluable.

I also like to thank deeply my co-supervisor, Dr. Ervin Podgorsak, for opening the door for me into this wonderful opportunity. Thank you for trusting in me and giving me the confidence to pursue a career in Medical Physics.

I would also like to thank Dr. Slobodan Devic and Dr. Siobhan Ozard for always taking the time to talk to me and for giving me research tips on my project.

My sincere appreciation goes to the entire staff of the McGill Medical Physics Unit for creating a friendly and stimulating environment. I would like to send my innermost appreciation for my good friends Conrad Yuen, Edwin Sham (a.k.a Shame On Him Edwin) and George Tsimiklis. Thanks for making my life in Montreal fun and enjoyable. I'll never forget the wild nights. Many thanks to my other classmates, Hugo Bouchard, Svetlana Denissova, Emily Heath, Fadi Hobeila, Deborah Hodefi, Silvana Oliveira, Faradally Ollite, Yanic Bercier, and Nada Tomic. An acknowledgement is also due to Ms. Margery Knewstubb and Ms. Santina Fiocco, graduate secretaries, for their assistance in dealing with administrative issues.

My appreciation also goes to the staff of the Jewish General Hospital, especially Ms. Micheline Gosselin, and Dr. Robert Corns for letting me use their PortPro EPID and Pips software.

To my parents, Kandiah and Someswari Kumaraswamy, thanks for all your love and caring. I am grateful to my sisters for all their constant support and warm encouragement. Also, I would like to express my profound gratitude to my brother for giving me the opportunity to pursue my dreams in Canada and pushing me to realize my

potential. My lovely nephews and nieces, thanks for being the little brothers and sisters that I never had.

Last, but not least, I would like to extremely thank my wife, "pooki" Rega. Without your love, understanding, and commitment, life alone in Montreal would not have been possible.

Thank you God for being with me and giving me all that I needed.

Table of Contents

List of figures

List of tables

Chapter 1

Introduction

This chapter presents a basic overview of medical x-ray imaging and the concept of radiation therapy in the treatment of cancer. It explains the need for treatment verification in radiation therapy and the drawbacks of current techniques using portal imaging with megavoltage photon beams. The chapter introduces some techniques used for portal dosimetry and concludes with a discussion on the aims and goals of this work.

1.1. MEDICAL X-RAY IMAGING

Wilhelm Conrad Roentgen, a German physicist, discovered x-rays on November 8, 1895[1]. Since their discovery, x-rays have been used widely to diagnose and treat diseases. Roentgen discovered that x-rays could penetrate through the body, forming images of bony structures and parts of the anatomy. This is the principle on which x-ray imaging for medical diagnosis is based.

Standard radiographic imaging for diagnostic radiology involves generation of relatively uniform beam of penetrating x-rays. Different parts of a patient's body may absorb and scatter x-rays differently, thereby forming a primary x-ray image out of the uniform beam. The image is then detected by radiographic film in a cassette. Any spatial non-uniformity in the emerging image is recorded on the film and is revealed upon its development as varying shades of grey.

Fluoroscopy is another form of diagnostic x-ray imaging, which may be used for dynamic studies in which the motion of blood circulation or hollow internal structures is involved. In this imaging technique, x-ray photons emerging from the patient are transformed into an optical image by an image intensifier (II) tube located underneath the patient[2]. The resulting images are captured by a television camera effectively creating a "live" x-ray image.

A special type of fluoroscopic imaging known as angiography images vessels and arteries injected with contrast media[2]. The dye is injected under fluoro, and then high-resolution spot films are obtained for diagnostic purposes.

Sectional radiographic imaging techniques use x-ray projections to reconstruct anatomic data. Computed Tomography does not utilize ordinary image receptors, such as film or an image-intensifier tube. Instead, a collimated x-ray beam is directed towards the patient, and the attenuated beam is measured by a detector whose response is transmitted to a computer which back projects the response data to reconstruct an image of the cross-sectional anatomy[3]. The advantage of this kind of tomographic imaging is the high soft-tissue contrast not seen in x-ray films.

Finally, computed radiography refers to the use of photostimulable phosphor imaging plates and the associated hardware and software for the acquisition and display of projection radiographs. This photostimulable phosphor stores some of the x-ray energy in crystal structure. This trapped energy can be released if stimulated by additional light energy of the proper wavelength by the process of photostimulated luminescence. The stimulated light is then used to create a digital image[4].

Treatment of cancer with high energy x-rays dates back as far as 1910[1]. Over the past couple of decades, there have been significant improvements in radiation treatment techniques resulting in more accurate dose delivery. Next few sections introduce the basic concepts of radiation therapy and the importance of treatment verification. It also presents the historical developments of megavoltage imaging.

1.2. RADIATION THERAPY

After heart disease, cancer is the second leading cause of death in Canada[5], accounting for 66,000 victims annually[6]. In 2002, approximately 136,900 patients were expected to be diagnosed with cancer in this country[6]. A Majority of cancer patients will be subject to some combination of surgery, radiotherapy, and chemotherapy. Approximately, half of the cancer patients will be administered radiation at some point in the course of their treatment[7].

Radiation therapy aims at tumor eradication by means of ionizing radiations, the most commonly employed types being photons and electrons, with energies ranging from a few hundred keV to a few MeV. Among all cellular perturbations caused by the ionizing radiations[8], the double-strand break in the DNA is the predominant cause for radiation induced cellular death[9]. The number of double-strand breaks is related to the physical quantity *absorbed dose*[10] or simply *dose,* which is energy deposited by radiation per unit mass of material (The SI unit of *dose* is *gray* (Gy) defined as 1 Gy = 1 J/kg). With increasing dose to tumor volume, the number of killed cancer cells increases and so does the probability of cure.

There are two main types of radiation treatments: external beam radiation, known as teletherapy, and internal therapy known as brachytheraphy. For brachytherapy, a radioactive source is placed inside the patient close to cancer cells or the tumor mass[11], while external beam radiation directs ionizing radiation from a remote source aimed at the patient. A typical teletherapy treatment unit (a linear accelerator or a cobalt unit) uses a radiation source mounted on a rotating gantry capable of moving around the patient who lies on the treatment couch. Multiple-correctly-collimated beams from different directions can be used to deliver the necessary dose to the tumor and minimize the dose to the healthy structures surrounding the tumor.

The goal of radiation therapy is to kill cancerous cells while sparing healthy cells. Since emitted radiation does not distinguish between cancer cells and normal tissue, radiation fields are very carefully planned, to protect uninvolved tissue and vital organs[12]. A critical requirement in radiation therapy is accurate treatment setup. It is very crucial to reduce setup errors and an effective way to implement this is to increase the frequency of treatment verification.

1.3. TREATMENT VERIFICATION

Experimental and clinical evidence show that small changes in dose of 7 to 15% can either reduce local tumor control significantly, or, increase the rate of normal tissue complications[13]. As a result, recommendations by the International Commission on Radiation Units (ICRU) suggest that the accuracy in dose delivery be within ±5%[14]. Such

accuracy can be achieved only if field placement is precise during the entire course of radiation treatment[15].

Number of studies has shown that discrepancies in field placement occur frequently, especially for complicated treatment setups[16-36]. Furthermore, these geometric discrepancies can also influence the outcome of treatment. Over the last century, the treatment of cancer by means of external beam of megavoltage x-ray radiation has benefited from a variety of significant technical advances. These technical advances include:

i) The three-dimensional imaging modalities such as Computed Tomography (CT), Magnetic Resonance Imaging (MRI), Positron Emission Tomography (PET), and Ultrasound, which are capable of providing anatomical and functional information useful for treatment planning.

ii) Sophisticated treatment planning software systems, which provide 3D imaging information.

iii) The development of increasingly sophisticated radiation delivery equipment, which facilitate the delivery of complex treatment plans[37].

Because of these advances in radiotherapy, much effort has been devoted to the development of means to image the patient during the radiation treatment. These megavoltage images, also known as portal images, serve to verify the placement of treatment fields administered to the patients. During the course of the treatment, two possible kinds of portal images are taken of the patient. First is the *Localization image*, which is taken using a small fraction of the treatment dose prior to the delivery of the main dose. Second is the *Verification image*, which is the portal image taken during the actual treatment. In the case of *localization imaging*, the objective is to view the image before proceeding with the main treatment to allow for the possibility of adjustment of the treatment set-up. *Verification imaging*, on the other hand, serves to provide a record of how the treatment was performed[37].

Treatment setup verification can be divided into verification of the geometric configuration of the treatment unit, and verification of the patient and target position with respect to the treatment geometry. The placement of radiation fields relative to the

patient is generally verified with a portal image obtained at the beam exit side of the patient. A reference image, which documents the intended patient set up, is obtained either during a treatment simulation with a low energy x-ray beam or with Digitally Reconstructed Radiograph (DRR) (obtained from CT slices). Bony anatomy and parts of the internal structures could be used as control points to verify the field alignment with portal image and the reference image.

1.4. MEGAVOLTAGE IMAGING

Imaging with megavoltage beam dates back as far as 1904[15] when radiographs of human hands, mice and other objects had been made using radium source[38]. However, because of the high energy of radium gamma rays, the image suffered from low contrast. During the next few decades, imaging techniques improved with the utilization of contrast agents and double exposure radiographs to visualize anatomy outside the treatment fields[39]. One of the major discoveries occurred in 1960, when Perryman *et al.* described "Cobalt 60 radiography"[40]. This technique used Kodak type AA industrial film (Kodak Company, Rochester NY) placed in a cassette in which the standard intensifying screens had been replaced by two 0.01" lead sheets. However, the only setback of this system was the developing time which was approximately 30 minutes. Two years later, Springer *et al.* employed two fluorescent screens between the lead sheets and the film to improve the contrast and reduce the exposure time[41].

Another landmark discovery was described by Swain and Steckel in 1966[42] and was further enhanced by Marks and Haus[43]. The method used slow, wide latitude, film which was placed in cardboard film-holders and was exposed for the entire duration of the treatment. These cardboard film holders were much more comfortable for patients to lie on than the film screen cassettes, and the patients were not moved between the exposure of the film and the treatment. Marks and Haus's contribution resulted in a film (known as the Kodak XV-2) (Kodak Company, Rochester NY) compatible with the 90 second film processors[44]. Even at present, in a typical radiotherapy clinic, about 70% of portal imaging is performed through the use of radiotherapy film cassettes.

At about the same time as port films were being introduced into radiotherapy clinics, non-film imaging methods were also investigated. In 1958, "television-roentgen (TVR) system" for monitoring the position of patients during pendulum therapy was employed[45]. The patients lay on the treatment couch while the gantry mounted TVR system (consisting of an x-ray image intensifier and a T.V. camera) rotated around the patient during the treatment with a 200 kVp x-ray beam. The video signal was then sent to a monitor located in the control room of the treatment machine. The major limitation was that this TVR system had a field of view of only 5.0 inches. Some other non-film systems were also studied but due to the poor image quality were never implemented in the clinics at that time[46, 47].

Despite the fact that radiotherapy film cassettes represent a compact, lightweight technology and provide useful information, they suffer from several major disadvantages. Since the film must be removed from the cassette and developed in a film processor, there is a gap of several minutes between exposing the film and obtaining information from it. In the case of localization imaging, this introduces a significant delay during which the information content of the film may become invalid (e.g. due to patient movement). In addition, as this delay adds significantly to the overall treatment time for a given patient, it discourages frequent localization checks. In the case of verification imaging, the use of film cassettes does not provide the possibility of monitoring the accuracy of treatment during the course of the delivery of a given portal field. Although it is certainly possible to render the film image into digital form using a film digitizer, this seldom happens in a practical setting because it is laborious and time consuming. Finally, film systems offer a relatively limited range of exposures over which the image is neither under nor over exposed. Due to these limitations, in the early 1980's non-film systems emerged again[15]. These devices can be divided into two categories: scanning systems, where the radiation detector subtends only a small fraction of the radiation beam and must be scanned underneath the patient to form the image, and area systems, where the detector subtends the entire radiation beam. These devices, called Electronic Portal Imaging Devices (EPIDs), were initially developed "in house" in dedicated research facilities and later migrated to industry where they were developed as commercial products.

Various types of EPIDs were developed; however, only the video based (VEPIDS), scanning liquid ionization (SLIC) and amorphous silicon (aSi) type EPIDS have evolved into commercially available systems. With these digital systems, a small fraction of the radiation dose delivered on a given day can be used to produce a digital on-line image that is displayed in real time or near real time. They enable treatment beam alignment to be visualized with respect to patient anatomy before a full radiation dose is administered[48]. Despite these advantages, however, EPIDs have not yet widely replaced portal films. This has been attributed to poor image quality, bulkiness, limited field of view, maintenance issues, and price of EPIDs. Film systems (viewed with naked eye) have slightly better image quality than the EPID systems and many researchers are trying to improve the image quality of EPID systems. While the sizes of the x-ray detectors are often only slightly smaller than that of standard film cassettes, the EPIDs are deployed at much larger isocenter-to-detector distances, thereby reducing their effective field of view. One partial exception is the Portpro EPID. Because it is mounted on a mobile cart, similar to the film cassettes, the device has large flexibility in its positioning. Thus, it can be located to take best advantage of its detector's field of view. There are wide ranges of research being implemented to overcome these limitations. Once these barriers are full filled, EPID systems could replace the port films which are widely used today.

1.5. PORTAL IMAGING DOSIMETRY

There are many research activities geared towards implementing EPIDs as dosimeters, to measure transmitted dose through the patient. With advent increase in special techniques in treatment planning such as intensity modulated treatment techniques, using EPIDs to measure dose could be very practical where other methods of verifying dose are cumbersome.

A simple yet effective application to dose measurements discussed by some researchers, consists of a direct and real time comparison of a measured portal dose image with a theoretical predicted portal dose image[49]. Another dosimetric treatment verification application of EPIDs involves the removal of scatter from the measured portal image, and then back projecting the remaining primary component through the

patient computed tomography data set which allows a calculation of deposited dose in the patient[48]. Others have used simpler approaches to relate measured portal images with patient mid-plane and/or exit dose estimates, but still require separate primary and scatter estimates in the portal image. Much research has to be performed to incorporate EPIDs as dosimeters. In the future, if these systems are able to measure and calculate the transit dose through the patients, it can provide a convenient method of verifying both the geometric and dosimetric accuracy of radiation treatments.

1.6. GOALS OF THIS THESIS

The goals of this thesis are two fold: (1) To compare and evaluate various portal imaging devices used for patient imaging, and (2) To pick a suitable device, and to evaluate it in the context of Intensity Modulated Radiation Therapy (IMRT) dosimetry. There are several diverse imaging systems available in the market. These systems include the film, Computed Radiograpy, and EPIDs. As mentioned above, various types of EPIDS were developed; however, only the video based (VEPIDS), scanning liquid ionization (SLIC) and amorphous silicon (aSi) type EPIDS have evolved into commercially available systems. First part of the project involves a comparative study of these imaging systems in terms of image quality. A number of key quantities that give an objective measure of image quality are measured. Apart form obtaining these quantities such as subject contrast, signal-to-noise ratio, spatial resolution, and modulation transfer function (MTF), energy and dose response are measured for each imaging modalities. This in turn would give a clear understanding on which imaging modality would be suitable for portal dose verification. Second part of the project involves dose verification of static and dynamic Intensity Modulated Radiation Therapy (IMRT) fields with the chosen imaging modality.

References

1. A. B. Wolbarst, *Physics Of Radiology* (Appleton & Lange, East Norwalk, 1993).
2. S. C. Bushong, *Radiologic Science for Technologists* 6th Edition (Mosby-Year Book, 1997).
3. T. S. Curry III, J. E. Dowdey, and R. C. Murry. *Christensen's Physics of Diagnostic Radiology* 4th Edition (Lippincott Williams & Wilkins, Media, 1990).
4. J. A. Seibert, "Computed Radiography Overview," presented at the Radiological Society Of North America, 84th Scientific Assembly and Annual Meeting, Chicago, (1998).
5. Canadian Cancer Society Web Site. Web Page : Canadian Cancer Statistics (http://www.cancer.ca/ccs/internet/standard/0,3182,3172_12851__langId-en,00.html).
6. Statistics Canada Web Site. Web Page: Canadian Deaths (http://www.statcan.ca/Daily/English/020507/d020507b.htm).
7. A. H. Knowlton, *General principles of radiation therapy* (Hall Medical Publishers, Boston, 1982).
8. A. S. Lichter, and T. S. Lawrence, "Recent advences in radiation oncology," The New England Journal of Medicine. **332**, 370-372, (1995).
9. M. M. Elkind, "DNA damage and cell killing: cause and effect?," Cancer, **56**, 2351-2363, (1985).
10. ICRU Report No. 33: *Radiation Quantities and Units. Techinical report*, International Commision on Radiation Units and Measurements, Washigton, DC, (1980).
11. SEER's Training Web Site. Web page: Introduction To Radiation Therapy 2003 (http://training.seer.cancer.gov/module_cancer_treatment/unit2_radiation1 intro.html).
12. Healthy Lifestyle Centre. Web page: Treatment Procedures – Cancer 2002 (http://jhhs.client.web-health.com/web-health/topics/GeneralHealth/generalhealthsub/ Radiationtherapy.html).
13. A. Dutreix, "When and how can we improve precision in radiotherapy?," Radiother Oncol. **2**, 275-292, (1984).
14. M. Goitein, and J. Buss, "Immobilization errors: Some theoritical considerations," Radiology, **117**, 407-412, (1975).
15. P. Munro, "Portal imaging technology: Past, present, and future," Semin. Radiat. Oncol. 5, 115-133, (1995).
16. J. Rabinowitz, M. Broomberg, K. Goitein, J. McCarthy, and J. Leong, "Accuracy of radiation field alignment in clinical practice," Int. J. Radiat. Oncol., Biol., Phys. **11**, 1857–67, (1985).
17. S. A. Rosenthal, J. M. Galvin, J. W. Goldwein, A. R. Smith, and P. H. Blitzer, "Improved methods for determination of variability in patient positioning for radiation therapy using simulation and serial portal film measurements," Int. J. Radiat. Oncol., Biol., Phys. **23**, 621–625, (1992).
18. S. E. Griffiths, R. G. Pearcey, and J. Thorogood, "Quality control in radiotherapy: The reduction of field placement errors," Int. J. Radiat. Oncol., Biol., Phys. **13**, 1583–1588, (1987).
19. H. Huizenga, P. C. Levendag, P. M. De Porre, and A. G. Visser, "Accuracy in radiation field alignment in head and neck cancer: A prospective study," Radiother. Oncol. **11**, 184–187, (1988).

20. G. van Tienhoven, J. H. Lanson, D. Crabeels, S. Heukelom, and B. J. Mijnheer, "Accuracy in tangential breast treatment set-up: A portal imaging study," Radiother. Oncol. **22**, 317–322, (1991).

21. C. Mitine, A. Dutreix, and E. van der Schueren, "Tangential breast irradiation: Influence of technique of set-up on transfer errors and reproducibility," Radiother. Oncol. **22**, 308–310, (1991).

22. A. Ezz, P. Munro, A. T. Porter, J. Battista, D. A. Jaffray, A. Fenster, and S. Osborne, "Daily monitoring and correction of radiation field placement using a video-based portal imaging system: A pilot study," Int. J. Radiat. Oncol., Biol., Phys. **22**, 159–165, (1992).

23. J. Bijhold, J. V. Lebesque, A. A. Hart, and R. E. Vijlbrief, "Maximizing setup accuracy using portal images as applied to a conformal boost technique for prostatic cancer," Radiother. Oncol. **24**, 261–271, (1992).

24. C. Weltens, G. Leunens, A. Dutreix, J. Cosset, F. Eschwege, and E. van der Schueren, "Accuracy in mantle field irradiations: Irradiated volume and daily dose," Radiother. Oncol. **29**, 18–26, (1993).

25. C. Mitine, A. Dutreix, and E. van der Schueren, "Black and white in accuracy assessment of megavoltage images: The medical decision is often gray," Radiother. Oncol. **28**, 31–36, (1993).

26. P. B. Dunscombe, K. Fox, S. Loose, and K. Leszczynski, "The investigation and rectification of field placement errors in the delivery of complex head and neck fields," Int. J. Radiat. Oncol., Biol., Phys. **26**, 155–161, (1993).

27. P. Dunscombe, S. Loose, and K. Leszczynski, "Sizes and sources of field placement error in routine irradiation for prostate cancer," Radiother. Oncol. **26**, 174–176, (1993).

28. M. A. Hunt, G. J. Kutcher, C. Burman, D. Fass, L. Harrison, S. Leibel, and Z. Fuks, "The effect of setup uncertainties on the treatment of nasopharynx cancer," Int. J. Radiat. Oncol., Biol., Phys. **27**, 437–447, (1993).

29. C. L. Creutzberg, V. G. Althof, H. Huizenga, A. G. Visser, and P. C. Levendag, "Quality assurance using portal imaging: The accuracy of patient positioning in irradiation of breast cancer," Int. J. Radiat. Oncol., Biol., Phys. **25**, 529–539, (1993).

30. M. G. Herman, R. A. Abrams, and R. R. Mayer, "Clinical use of on-line portal imaging for daily patient treatment verification," Int. J. Radiat. Oncol., Biol., Phys. **28**, 1017–1023, (1994).

31. J. Gildersleve, D. P. Dearnaley, P. M. Evans, M. Law, C. Rawlings, and W. Swindell, "A randomised trial of patient repositioning during radiotherapy using a megavoltage imaging system," Radiother. Oncol. **31**, 161–168, (1994).

32. M. A. Hunt, T. E. Schultheiss, G. E. Desobry, M. Hakki, and G. E. Hanks, "An evaluation of setup uncertainties for patients treated to pelvic sites," Int. J. Radiat. Oncol., Biol., Phys. **32**, 227–233, (1995).

33. A. Bel, R. Keus, R. E. Vijlbrief, and J. V. Lebesque, "Setup deviations in wedged pair irradiation of parotid gland and tonsillar tumors, measured with an electronic portal imaging device," Radiother. Oncol. **37**, 153–159, (1995).

34. F. Van den Heuvel, W. De Neve, D. Verellen, M. Coghe, V. Coen, and G. Storme, "Clinical implementation of an objective computer-aided protocol for intervention in intra-treatment correction using electronic portal imaging," Radiother. Oncol. **35**, 232–239, (1995).

35. A. Lirette, J. Pouliot, M. Aubin, and M. Larochelle, "The role of electronic portal imaging in tangential breast irradiation: A prospective study," Radiother. Oncol. **37**, 241–245, (1995).

36. A. Bel, P. H. Vos, P. T. Rodrigus, C. L. Creutzberg, A. G. Visser, J. C. Stroom, and J. V. Lebesque, "High-precision prostate cancer irradiation by clinical application of an offline patient setup verification procedure, using portal imaging," Int. J. Radiat. Oncol., Biol., Phys. **35**, 321–332, (1996).

37. L. E. Antonuk, "Electronic portal imaging devices: a review and historical perspective of contemporary technologies and research," Phys. Med. Biol. **47**, R31-R65, (2002).

38. J. Leong, and D. Shimm, "A method for consistent precision radiation therapy," Radiother Oncol. **3**, 89-92, (1985).

39. H. F. Hare, S. W. Lippincott , and D. Sawyer, "Physical and clinical aspects of supervoltage rotational therapy," Radiology. **57**, 157-168, (1951).

40. C. R. Perryman, J. D. McAllister, and J. A. Burwell, "Cobalt 60 radiography," Am J Roentgenol. **83**, 525-532, (1960).

41. E. B. Springer, L. Pape, F. Elsner, et al., "High-energy radiography (Cobalt 60 and Cesium 137) for tumor localization and treatment planning," Radiology. **78**, 260-262, (1962).

42. R. W. Swain, and R. J. Steckel, "Beam localization in cobalt and megavoltage therapy during treatment," Radiology. **86**, 529, (1966).

43. A. G. Haus, S. M. Pinsky, and J. E. Marks, "A technique for imaging patient treatment area during therapeutic radiation exposure," Radiology. **97**, 653-656, (1970).

44. A. G. Haus, *Historical developments in film processing and medical imaging*, in Haus AG(ed):Film Processing and Medical Imaging (Wisconsin, Medical Physics Publshing, 1993).

45. H. Wallman, and N. Stalberg, "A television-roentgen system for pendulum therapy," Br J Radiol. **31**, 576-577, (1958).

46. R. H. Morgan, and R. E. Sturm, "The Johns Hopkins fluoroscopic screen intensifier," Radiology. **57**, 556-560, (1951).

47. S. Benner, B. Rosengren, H. Wallman, et al., "Television monitoring of a 30 MV x-ray beam," Phys Med Biol. **7**, 29-34, (1962).

48. A. L. Boyer, L. Antonuk, A. Fenster, M. Van Herk, H. Meertens, P. Munro. L. E. Reintein, J. Wong, "A review of electronic portal imaging devices (EPIDs)," Med. Phys. **19**, 1-16, (1992).

49. B. M. C. McCurdy, K. Luchka, S. Pistorius, "Dosimetric investigation and portal dose image prediction using an amorphous silicon electronic portal imaging device," Med. Phys. **28**, 911-924, (2001).

Chapter 2

Imaging Modalities

2.1. Introduction

This chapter introduces the imaging systems investigated in this study, which include: Film, amorphous silicon EPID, liquid matrix EPID, fluoro based EPID, and the computed radiography system. The basic concepts of each systems as well as method of operation also is discussed.

2.2. Film

The portal film cassette systems consist of an x-ray film sandwiched between a front plate and a rear plate made of either plastic or metal. X-ray film is a photographic film consisting of a photographically active, or radiation-sensitive, emulsion that is usually coated on both sides of a transparent sheet of plastic, called the base. Firm attachment between the emulsion layer and the film base is achieved by use of a thin layer of adhesive. The delicate emulsion is protected from mechanical damage by layers known as the supercoating[1] (Fig. 2.1).

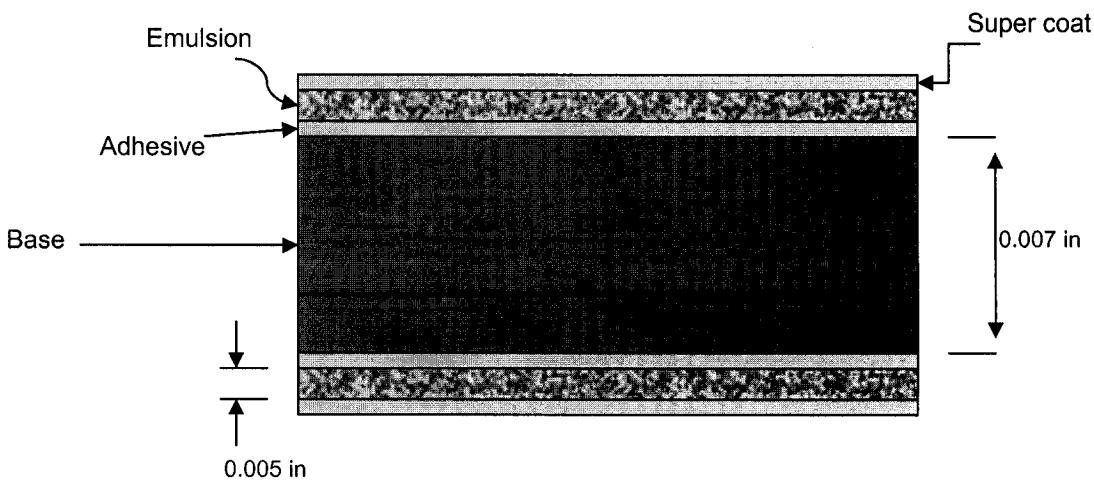

Fig. 2.1. Cross section of a double emulsion x-ray film.

As the figure above illustrates, the film base supports the emulsion coating on both sides of the film. It must be very flexible and should not produce any visible patterns when processed. At the beginning of the century, glass plate was used as film base. With much research and progress the composition of the film base was modified to polyester. Polyester gives improved dimensional stability even at varying humidity. Since the polyester base is clear and colorless, blue dye is added to produce a film that is "easier to look at." The polyester base is about 0.007 inches thick and a thin layer of adhesive substance is applied between the base and the emulsion to ensure perfect union[1].

The exact chemical composition of emulsion is very closely guarded but it is primarily composed of gelatin and silver halide. The emulsion thickness varies with film type but it is no thicker than 0.005 inches. A thicker emulsion would not be useful because of the inability of light to penetrate to the deeper layers. Gelatin in the film emulsion is mainly made from cattle bone and it has certain advantages over other suspension media. The gelatin keeps the silver grain uniformly dispersed. It is also available in large quantities and it does not lose its strength or permanence when the processing chemicals penetrate the emulsion layer. Silver halide is the light sensitive material in the emulsion. More than 90% of the x-ray films have bromide as its halide agent and less than 10% have iodide as its halide agent. Silver iodide films are more sensitive than silver bromide films. The silver iodo-bromide crystals are precipitated and emulsified in the gelatin under exacting conditions of concentration and temperature. The sequence and the rate at which these chemicals are added are also of utmost importance. The method of precipitation determines crystal size, structural perfection, and concentration of iodine. In general, the precipitation reaction involves the addition of silver nitrate to soluble halide to form the slightly soluble silver halide. The silver halide in a photographic emulsion is in the form of crystals suspended in the gelatin and is arranged in a cubic lattice as shown in figure 2.2[(1)].

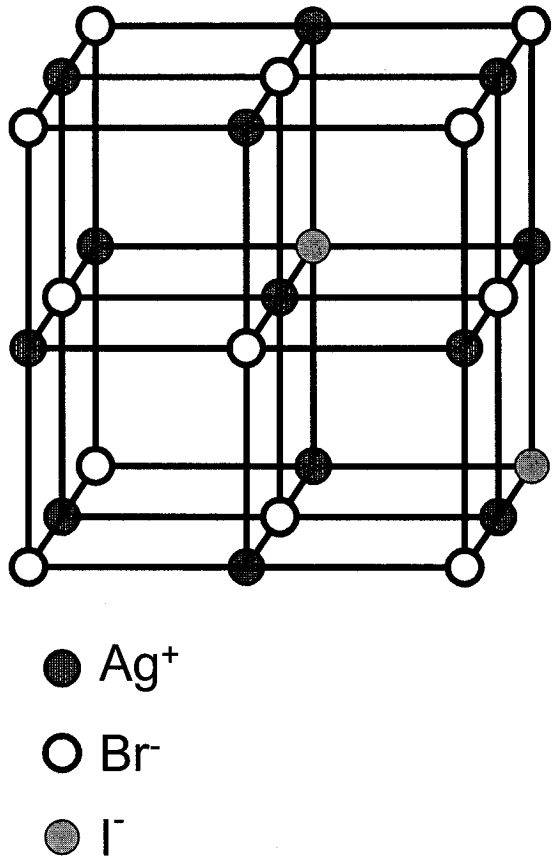

Fig. 2.2. Illustration of a silver iodobromide crystal lattice. These crystal lattice structures form the film emulsion layer of an x-ray film.

When these crystal lattice structures are exposed to light or direct x-rays, the formation of silver atoms darkens the area seen on a developed radiograph. A Silver atom is created when the energy from an absorbed light photon liberates an electron from a bromine ion. This ejected electron travels some distance in the lattice until it encounters an impurity or fault in the crystal. Impurities act as an electron trap where the electron is captured and temporarily fixed. The negative charge of the electron attracts the positive silver ion and neutralizes the ion to form the silver atom. Subsequently, the neutral silver atom acts as an electron trap to attract another electron which causes the migration of the second silver ion to the trap site to form two atom silver nucleus. This process continues to produce a cluster of silver atoms called latent image centers. The energy of one absorbed x-ray photon can produce thousands of silver atoms at latent image sites. When the radiograph is developed, the latent image is amplified by a factor of millions to form a visible silver pattern. During the developing process, the basic action of the developing

agents is to reduce silver ion into black metallic silver. The silver grains which are not part of the latent image are also developed, but at a slower rate. Larger the cluster, faster the developing process and hence the radiograph shows darker patterns where the silver atom clumps are the largest.

Individual conventional portal films can be purchased as loose or as packaged in envelopes. Packaged film inserted in the film cassette have a lower spatial resolution than the loose film inserted in the cassette because electrons generated in the metal plate spread before reaching the film emulsion in the former. However, spatial resolution of the current metal plate/film image receptor is so much higher than is required to image the bony anatomy that the reduction in spatial resolution due to lateral electron migration in the film wrapping has little visual impact on image quality. Moreover, individually wrapped films offer convenience because the portal cassettes can be daylight loaded, saving the effort of transporting the heavy cassettes to the dark room after irradiation. For these advantages over loose films, wrapped films are used more often for treatment verification than loose films. For therapy *localization*, either Kodak X-OMAT TL or Portal Pack PPL films are used and for therapy *verification* Kodak X-OMAT V films are used. *Localization* films are very sensitive to x-ray radiation so only 5 to 7 monitor units (~ 1.0 to 1.5 cGy at the image receptor) are required to produce a useful image, where as *verification* films are mush less sensitive and therefore require about 40 to 100 monitor units (~ 12 to 30 cGy at the image receptor). The dose reaching the image receptor depends upon energy of the x-ray beam, patient thickness, position of the image receptor, and various factors that influence scattered radiation reaching the image receptor. Often tables known as technique charts are calculated using empirical data to predict the monitor unit setting that will optimize the exposure at the image receptor[2]. An alternative to using portal films is to use EPIDs which are discussed in the next section.

2.3. ELECTRONIC PORTAL IMAGING DEVICES

Many different electronic portal imaging devices (EPID) have been developed as an alternative to film for megavoltage imaging. This section describes the three types of EPIDs that have become available commercially – the fluoro based EPID, the matrix ion chamber EPID and the amorphous silicon EPID. The practicality of these devices makes it feasible to verify treatment portals with much greater frequency than with films. Images acquired through the EPIDs are digital and hence geometric analysis, and image improvements can be performed through appropriate software. The aim of the EPIDs is to improve the geometric accuracy of radiation treatments through better and more practical imaging. Therefore, it is essential that the EPIDs do not make the setup of the patient more awkward, or complex which would lead to an increase rather than decrease in field placement errors[3]. A typical patient setup with EPID is shown in figure 2.3. The EPID is attached to the lower end of the gantry and it can be deployed during imaging process. When the EPID is not in use, it is retracted back into the gantry.

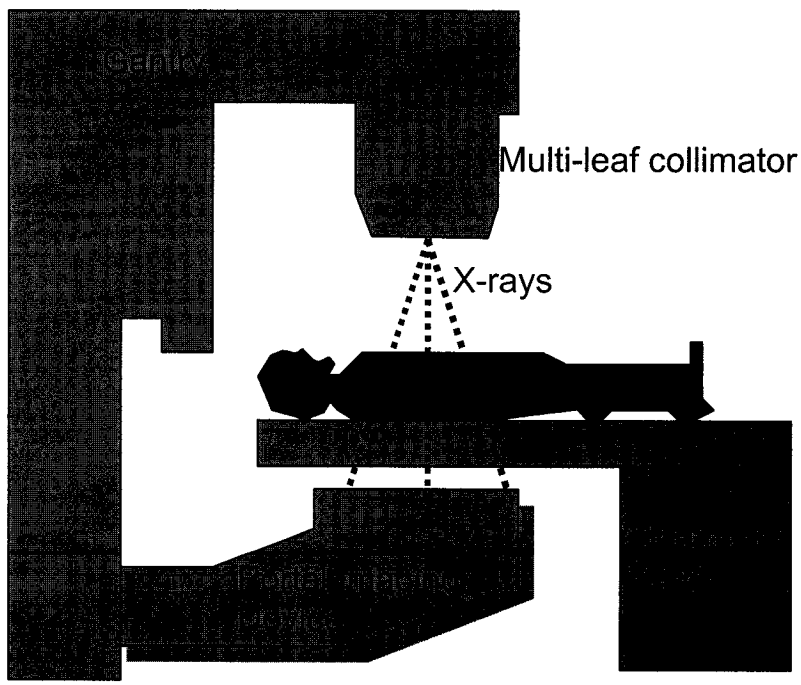

Fig. 2.3. Typical patient set up during portal imaging with EPID in radiotherapy.

Image formation by the EPIDs involves converting the incident high energy photons to measurable signal. For the amorphous silicon EPID and fluoro based EPID, the high energy photons interact with a metal plate and a phosphor screen resulting in generation of light photons. Image is formed when these light photons are detected by the flat panel light sensor of the amorphous silicon detector or by the CCD camera of the fluoro based EPID. On the other hand, the matrix ion chamber EPID has a matrix of ion chambers, which are filled with non-polar liquid. The incident high energy photons interact with the non-polar liquid to form ion pairs, which are then sampled by applying high-voltage pulses to each ion chamber to generate an image. More detail description of image formation by each of the EPIDs is discussed later.

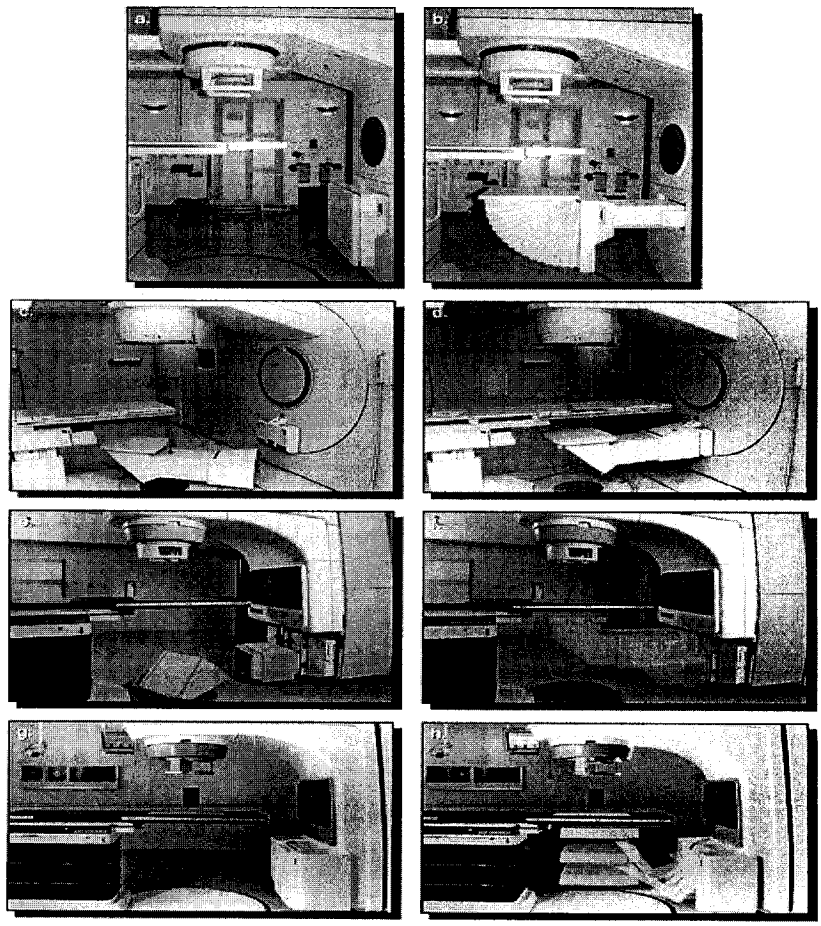

Fig. 2.4. Photographs showing the various commercially available EPIDs[3].

Photographs of EPIDs from different manufactures, while retracted and while deployed, are shown in figure 2.4. Clearly, widely differing designs have been used for the EPID assemblies. The mechanical assemblies are either retractable [figure 2.4 (a, b, g, h)], demountable [figure 2.4 (c, d)], or partly demountable and partly retractable [figure 2.4 (e, f)][3]. The following discussion will concentrate on the fluoro based EPID, matrix ion chamber EPID and the amorphous silicon array EPID.

2.3.1 *Fluoro Based EPIDs*

This approach has been under continuous, incremental development since the 1950s by a wide variety of investigators and institutions[4-6]. As illustrated in figure 2.5, the approach for fluoro based EPID involves the use of an x-ray converter that is optically coupled to a camera by means of a mirror and a lens. The converter consists of a flat metal plate (typically ~ 1 to 1.5 mm copper, steel or brass plate) and a gadolinium oxysulfide (Gd_2O_2S:Tb) phosper screen. When irradiated, high energy electrons generated in the metal plate and the Gd_2O_2S:Tb screen are converted into light. The light that diffuses through the screen and exits the rear surface of the x-ray detector is viewed by a television. Given the large amount of radiation associated with radiotherapy treatments, the electronics of the camera would quickly degrade if it was routinely exposed to the direct beam. For this reason, the mirror is set at a 45° angle to direct the light out of the radiation field towards the camera. The lens serves to collect a fraction of the light emitted by the phosphor and focus it on the surface of the camera sensor. The optical components are enclosed in a light-tight housing to exclude light signal from sources other than the phosphor. It is estimated that, depending on the thickness of the phosphor and the energy of the radiotherapy beam, on the order of only ~2-4% of the incident x-rays interact and generate measurable signal in such systems[7].

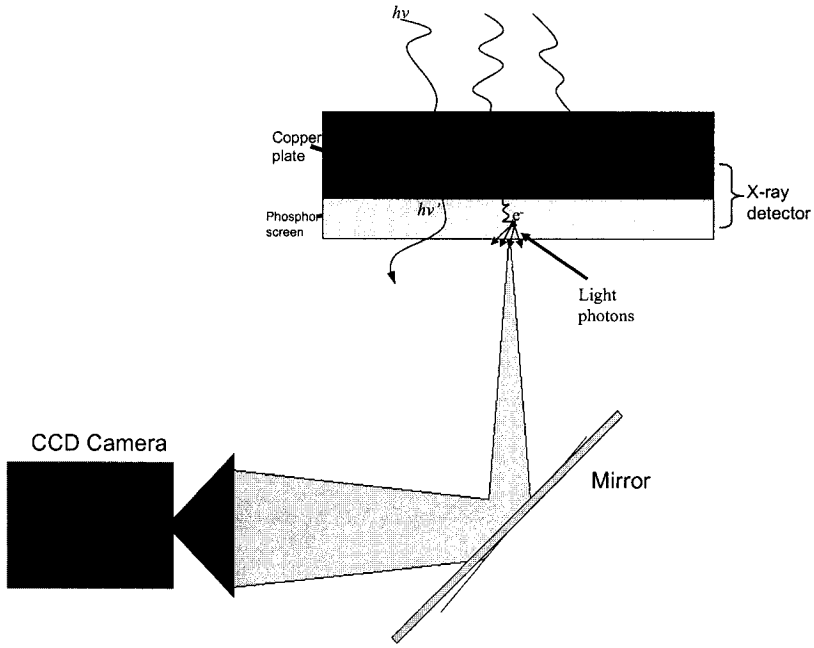

Fig. 2.5. Schematic illustration of imaging chain of the Fluoro based EPID.

2.3.1.1. Physics of imaging chain

During imaging, the incident x-rays can either interact with the flat metal plate or with the phosphor screen. The dominant interaction process is Compton scattering, creating an electron, which is forward scattered. The electron begins to travel and gradually loses its kinetic energy by ionizing the surrounding environment until it is stopped.

The energy, which is deposited in the phosphor, is partially transformed into optical light. Some of the optical photons will finally leave the front surface of the phosphor and get reflected by the 45° mirror on to the CCD camera as illustrated by figure 2.5. The camera serves to capture a fraction of this emerging light and transform it into a video signal that is then sent to other hardware for digitizing, processing, and display.

A major advantage of this approch is that the converter can cover all (or at least a very large fraction) of the portal field and the camera can sense the light signal from the entire converter simultaneously. Consequently, all of the radiation passing through the

patient and incident upon the converter has the potential of generating signal in the camera and clinically useful images can be produced with as few as couple of monitor units. A secondary, though important, practical advantage is that such system can be assembled from relatively common, commercially available components. As a result, the system has been made available by a number of manufacturers.

The major disadvantage of the approach is that the optics of the system only allows those light photons emerging from the phosphor within a small cone subtended by the lens of the camera to generate a signal as shown in figure 2.5. As a result, only 0.1-0.01% of the light emerging from the phosphor reaches the sensor of the camera. This effect reduces image quality. Some of the light emitted by the screen can reflect from the mirror so as to re-scatter from the phosphor screen and reach the camera. This signal then appears to have come from one part of the screen when, in fact, it originated form another part. This spurious signal, known as glare, can be more than 25% of the total measured signal, reducing contrast and complicating efforts to use the imager information for quantitative purposes. A related problem is the appearance of multiple images. The screen acts as a mirror which images its own reflection in the mirror. Moreover, the scattered signals may cause the pixels in the CCD camera to saturate. This effect known as "blooming" considerably reduces the spatial resolution of the images.

2.3.2 *Liquid matrix ionization chamber EPIDs*

This imaging system, which employs ion transport in a liquid, was developed at The Nederland Kankar Institute (NKI) by Meertens, van Herk and their colleagues[7]. Liquid ion matrix EPID consists of two sets of electrodes that are oriented perpendicular to each other separated by a 0.8 mm gap, which is filled with a non-polar liquid (2,2,4-trimethylpentane) that is ionized when the device is irradiated[3]. The electrode spacing is 1.27 mm and, since each set of electrode consists of 256 electrode cells, the active area of the matrix ion chamber array is 32.5 cm on a side. One set of electrodes is connected to 256 electrometers and other set of electrodes is connected to a high voltage supply which can apply a 300 volt potential to each electrode individually. Each electrode gets sampled sequentially during irradiation to form an image based on charge collection. This type of EPID is referred to as a scanning liquid ionization chamber (SLICE).

2.3.2.1. *Non-polar liquids for ionization chamber*

There are several properties of liquids for ionization chambers that are important. First, one needs to know the electron yield; that is, the number of charges that are produced and are collectable for a given amount of energy absorbed in the liquid. The higher the yield the better will be the signal to noise ratio. The electron yield is a function of both the applied electric field and the rate of energy loss of the ionizing particle. Other physical properties important to detector operation are electron mobility μ and the related conduction band energy. The drift velocity v_d of electrons is proportional to the mobility:

$$v_d = \mu E, \tag{2.1}$$

where E is the electric field. The velocity must be large enough so that charges will be cleared before the next event or shower. The conduction band energy must be low so that intrinsic trapping is minimal, and mobility high. The liquid used in our liquid matrix EPID is 2,2,4-trimethylpentane. This liquid has very low band energy of -0.36 eV and a high electron mobility of 30 cm^2/Vs [8].

2.3.2.2. *Physics of image formation in the Liquid matrix EPID*

During radiation, the non-polar liquid within the electrode plates gets ionized creating positive ions and free electrons as illustrated in figure 2.6. Since the liquid is not purified, the free electrons are quickly bound to water, oxygen, or some other electronegative contaminant, hence free electron transport does not occur[9]. This system solely relies on heavy-ion transport for the detection of ionizing radiation. The mobility of these ions is extremely low (2.9×10^{-4} cm^2/Vs), compared to the mobility of free electrons. With the relatively low ion mobility and the high density of the liquid, recombination loss in the chamber is significant. As a result, the ion pair concentration in the ionization chamber rapidly reaches a steady state in which ion-pair creation by the radiation field is balanced by ion-pair recombination. The steady state ion pair concentration in the 2,2 4-trimethylpentane liquid is sampled by the high-voltage pulses applied in turn to each pixel as seen in figure 2.6.

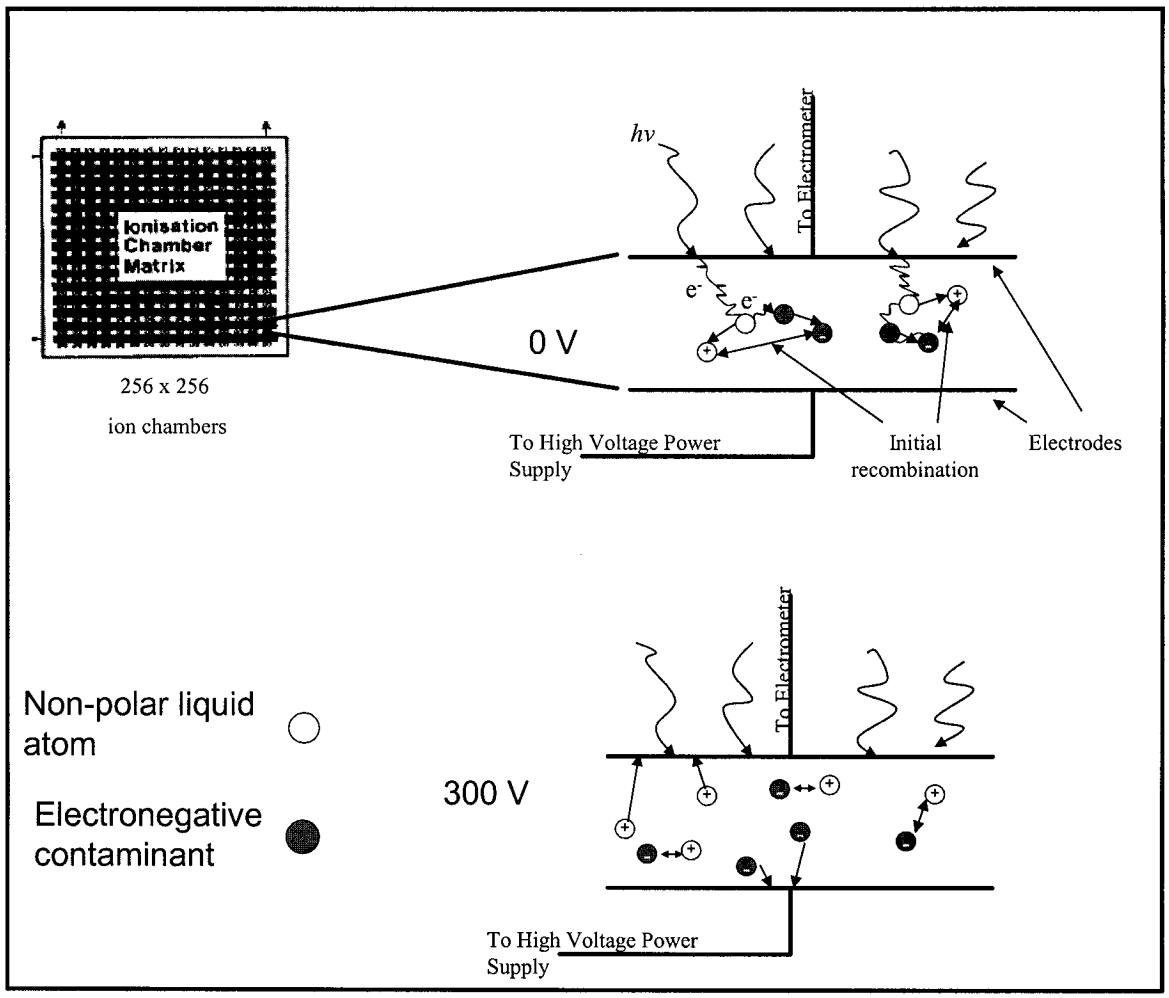

Fig. 2.6. Illustration of physics of image formation in Liquid ion chamber EPID.

2.3.2.3. Image acquisition

The imager can be operated in either *standard* acquisition mode or in *fast* acquisition mode. Following sequences illustrate the steps involved in acquisition of an image in *standard* mode following irradiation (with a help of figure 2.7).

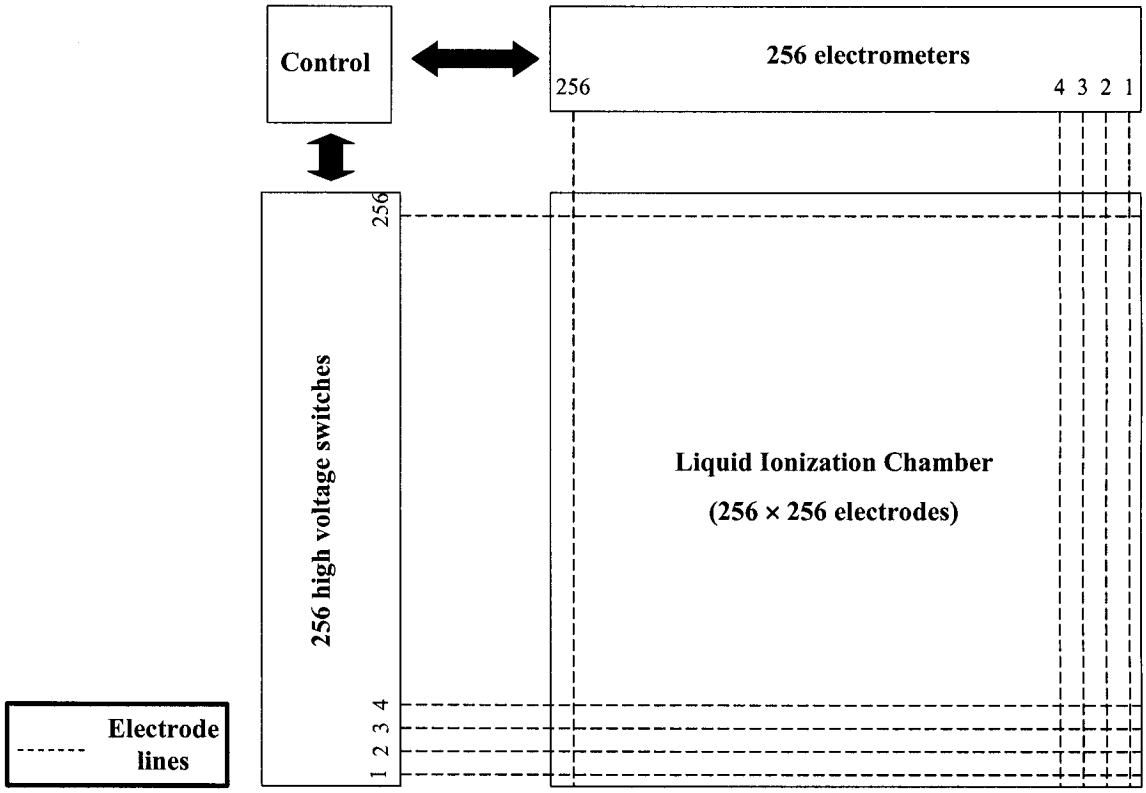

Fig. 2.7. Illustration of the image detection unit of the Liquid ion matrix EPID.

1. Electrode line #1 is set to 300 V by high voltage switch.
2. All 256 electrometers measure ionization current of electrode line #1.
3. Electrode line #2 is set to 300 V and electrode line #1 is set to 0 V.
4. All 256 electrometers measure ionization current of electrode line #2.
5. Electrode line #3 is set to 300 V and electrode line #2 is set to 0 V, etc...

This process continues until all the 256 electrode lines have been measured. The entire process takes about 2.76 seconds to acquire a single image. In the fast mode, pairs of electrodes lines are measured simultaneously, which reduces the total read-out time to 1.56 seconds but concurrently decreases the spatial resolution by a factor of two in the direction perpendicular to the electrode lines.

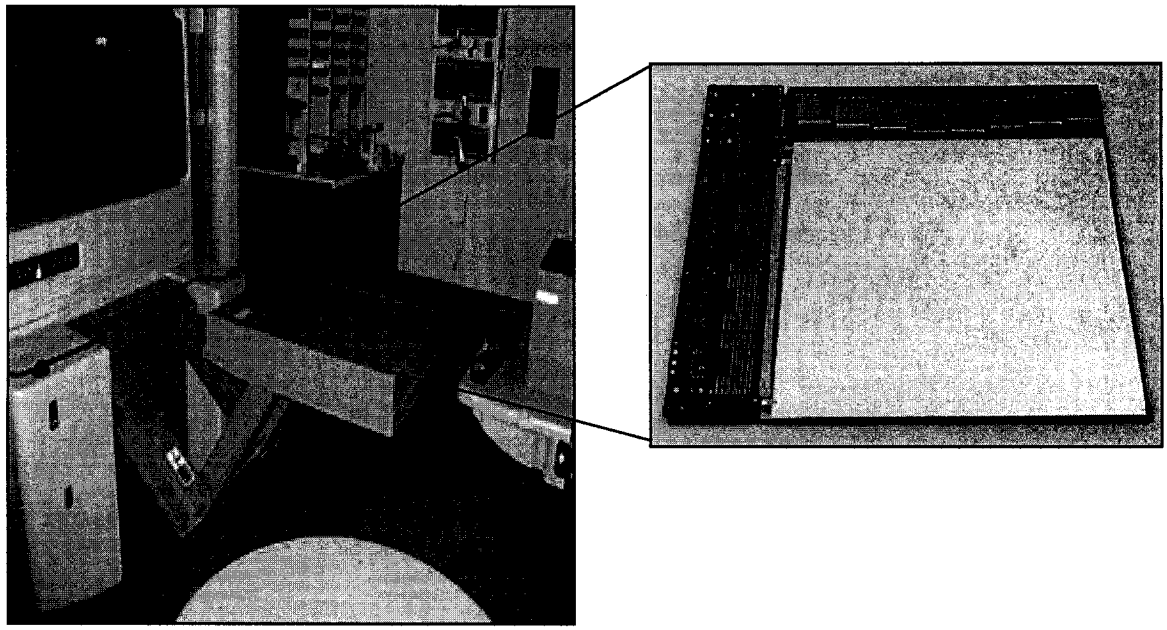

Fig. 2.8. Photos of the matrix ionization chamber EPID design.

The chamber and the peripheral electronics can be packaged compactly, as shown in figure 2.8. The most obvious advantage of the matrix ion chamber is its compact size, which makes the device a convenient replacement for film. Another advantage is geometric reliability – images acquired with this EPID have no geometric distortions.

The major limitation of most EPIDs that use a scanning radiation detector, such as the matrix ion chamber, is quantum utilization. Ideally, an image receptor should use all of the available radiation efficiently (even for megavoltage imaging) since this will improve image quality. Clearly, this is not the case for the matrix ion chamber, where only one high voltage electrode (out of 256) is active at any one moment[3].

Calculations have shown that after 0.5 seconds, a latent image has been formed over the entire irradiated region of the matrix ion chamber and, that irradiating for a longer time will not increase the size of the signal (i.e., will not improve image quality). These observations have both positive and negative implications. The measured signal is six to seven times greater than would be expected if no charge integration occurred in the 2,2,4-trimethylpentane. However, the effective period of the charge integration (~0.5 s) is still short compared to the total image acquisition time of 2.76 s. But the imager still needs to

be irradiated for the entire 2.76 s for the steady state ion concentration to be present for the entire duration of the sampling period. Therefore, a large fraction of the radiation that interacts with the matrix ion chamber does not generate any measurable signal. For this reason the matrix ion chamber requires higher doses to generate images than other portal imaging devices[3].

2.3.3 *Amorphous Silicon EPIDs*

Considerable research has been devoted to develop the technology of amorphous silicon flat panel array imager. This imager consists of the following subsystems: (a) a large area, pixilated array; (b) an overlying x-ray converter; (c) an electronic acquisition system which controls the operation of the array and extracts and processes analog signals from the array pixels and; (d) a host computer and information system which sends commands to, and receives digital pixel data from the acquisition system as well as processes, displays, and archives the resulting digital images.

The large pixilated array consist of 512 × 384 pixels forming a field of view of 40 × 30 cm^2, with a pixel pitch of 0.75 mm. The x-ray detector consists of a 1.5 mm copper plate overlying a scintillating layer of phosphor (Kodak Lanex Fast B- Gd_2O_2S:Tb, 134 mg/cm^2)[10]. The phosphor screen is attached to the amorphous silicon light sensor by use of transparent glue, which attaches the screen permanently to the array as illustrated in figure 2.9.

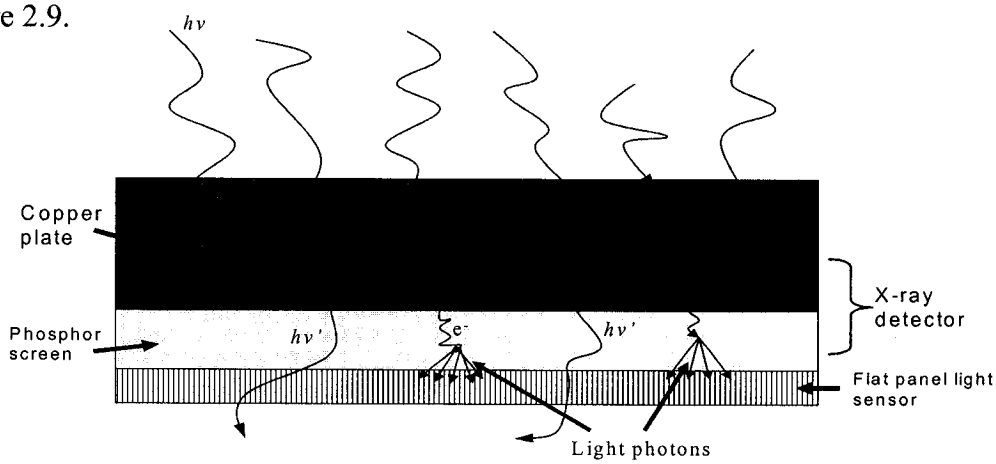

Fig. 2.9. Illustration of the image formation in amorphous silicon EPID.

Each pixel in the flat panel array sensor is composed of a photodiode and two thin film transistors (TFTs). The photodiode and the TFTs are made up of amorphous silicon (a-Si:H) semiconductor material. During imaging, incident high-energy photons are converted to electrons in the x-ray converter resulting in the generation of light photons. These light photons are detected by the a-Si:H semiconductor photodiodes incorporated in the flat panel light sensors. The principle behind light photon detection by a semiconductor is described in the next section.

2.3.3.1. Principle operation of semiconductors

The semiconductor material absorbs the incoming photons and converts them into electron-hole pairs as illustrated in figure 2.10. In this photogeneration step, the decisive parameter is the band gap energy E_{gap} of the semiconductor. In an ideal case, no photons with an energy $hv < E_{gap}$ will contribute to photogeneration, where as photons with an energy $hv > E_{gap}$ will contribute the energy E_{gap} to the photogenerated electron-hole pair with the excess energy (hv - E_{gap}) being very rapidly lost because of thermalization. For a-Si:H semiconductors, this band gap energy E_{gap} is about 1.8 eV[11].

In the second step of the energy conversion process, the photogenerated electron-hole pairs are separated, with electrons drifting to conduction band and holes drifting to the valence band, because of the internal electric field created by the diode structure. The output signal from semiconductor is read by collecting the electron-hole pairs in the depleted intrinsic region of the semiconductor.

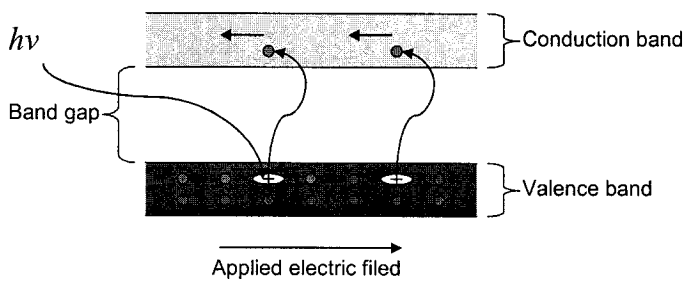

Fig. 2.10. Illustration of an intrinsic semiconductor.

2.3.3.2. *Hydrogenated Amorphous Silicon (a-Si:H) semiconductor*

Properties of a-Si:H are quit different from those of crystalline material. Amorphous silicon (a-Si), like common glass, is a semiconductor material with silicon atoms arranged disorderly, different from crystalline silicon (c-Si). The loss of structure order results in defects such as dangling bonds and distorted Si-Si bonds (in both lengths and angles). Defects yield energy levels in the energy gap where electrons recombine with holes thus limiting the flow of current. When amorphous silicon is deposited under hydrogenation conditions (like plasma enhanced chemical vapor deposition), the hydrogen atoms saturate the dangling and weak bonds thus removing defects and results in a defect free energy gap. It is a direct-gap semiconductor with the energy gap close to 1.8 eV and electron and hole mobility on the order of 10 cm^2/Vs[11]. It has a much larger absorption coefficient of light than the crystalline silicon, and it is resistant to radiation damage. Moreover, the amorphous silicon arrays can be made large with dimensions of 30×40 cm^2[12]. These above qualities makes a-Si:H a suitable semiconductor material for building x-ray image sensors.

2.3.3.3. *Image acquisition*

When the light photons are being detected by the a-Si:H semiconductor photodiode, which has a 5 V bias voltage applied before irradiation, the photodiode gets discharged gradually. The amount of discharge constitutes the integrated imaging information. During readout, the TFTs, which act like switches to control the readout of the signal, are made to conduct (by applying a control voltage) and this allows current to flow between the photodiode and an external amplifier. After readout, the corresponding photodiode is recharged to its original bias voltage and the external amplifier records the charge. This charge is proportional to the light reaching the photodiode during the irradiation. By activating the TFTs one column connected to a common external amplifier, the signals generated in the flat-panel light sensor can be read out one line at a time with a modest number of electronic components. Illustration of the active matrix array and its associated electronic circuitry is shown in figure 2.11. The above process is repeated for each row in the flat-panel light sensor until the entire sensor is read out, a process that

can, in principle, be done at ~ 25 frames/seconds. However, limitations in the computer interface reduce the continuous data transfer rate to ~ 5 frames/s for our device.

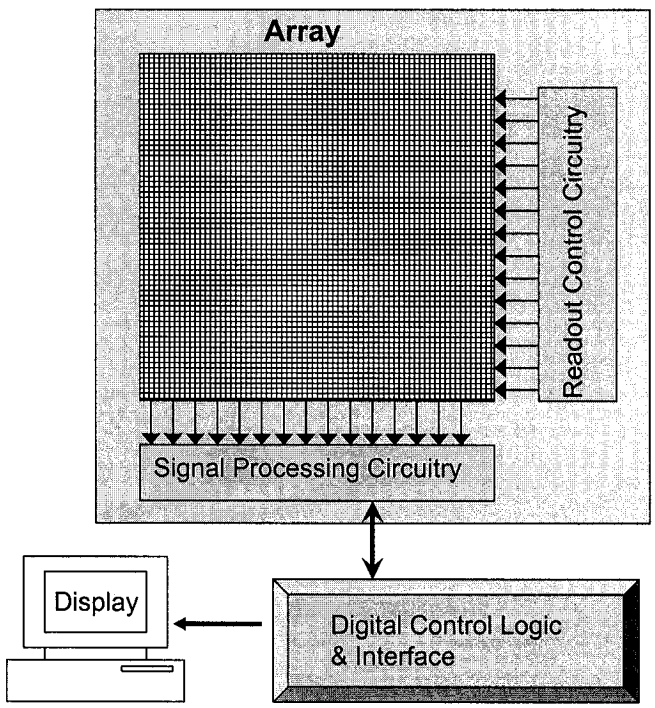

Fig. 2.11. Illustration of an active matrix array and its associated electronic circuitry housed inside the image receptor and connected to a digital image processor and image display device.

Perhaps one of the most important advantages of the flat panel light sensor technology for portal imaging is the high degree of image quality. For example, given: (a) that the array photodiodes are in close proximity to the scintillator; (b) that a large fraction of the pixel area is occupied by the photodiode for arrays designed for portal imaging; (c) the high efficiency of conversion of light entering the photodiodes into electron-hole pairs and (d) the high efficiency of readout of the signal from the pixels; then amorphous silicon EPIDs are capable of using on the order of 50% of the light emitted from the scintillator. This value is several orders of magnitude larger than optical transfer efficiencies for camera–mirror lens-based systems and the sampling efficiencies of ion-pair concentration in liquid matrix ion chamber EPID systems. The close proximity of the photodiodes to the scintillator also sharply limits glare in the flat panel light sensor—a problem for camera mirror–lens-based systems. Moreover, preliminary

studies comparing amorphous silicon EPID and matrix-ionization-chamber EPIDs strongly suggest superior image quality from the amorphous silicon EPID[13]. Finally, an observer-based contrast-detail study comparing amorphous silicon EPID and portal film systems indicates that amorphous silicon EPID may offer performance superior to that of a conventional portal imaging film system[11].

2.4. COMPUTED RADIOGRAPHY

Computed radiography refers to the use of photostimulable phosphor imaging plates and the associated hardware and software for the acquisition and display of projection radiographs. This system is primarily used for diagnostic radiology where x-ray energies are in the kilovoltage range. Computed radiography systems, also known more generically as photostimulable phosphor (PSP) imagers, work on the principle of photostimulated luminescence (PSL). In many ways, a PSP is similar to the conventional screen used in film-screen radiography. When the screen absorbs x-rays, the x-ray energy is converted to light energy by the process of fluorescence, with the intensity of the light being proportional to the energy absorbed by the phosphor. The conventional screen emits virtually all of this light energy immediately after exposure to the x-rays, and the light intensity is recorded on film which is then developed and used to display the image. While it also produces enough fluorescence to expose a conventional x-ray film, the PSP stores some of the x-ray energy in crystal structure "traps", so it is sometimes referred to as a "storage" phosphor. This trapped energy can be released if stimulated by additional light energy of the proper wavelength by the process of photostimulated luminescence. The stimulated light is used to create a digital image. Removal of any residual latent image is achieved by erasure with a high intensity light, so that the phosphor plated can be reused.

The phosphor plate is composed of a Europium-doped Barium-fluorohalide crystal, BaFX:Eu, where X= Br, Cl, or I. Figure 2.12 shows a cross section view of a phosphor plate. In the phosphor plate composition, some traces of impurities are added (also called doping) to the crystal to alter its structure. The trace impurity is also called an activator. A Europium ion (Eu^{2+}) replaces Barium (Ba) in the crystal and forms a *luminescence center.*

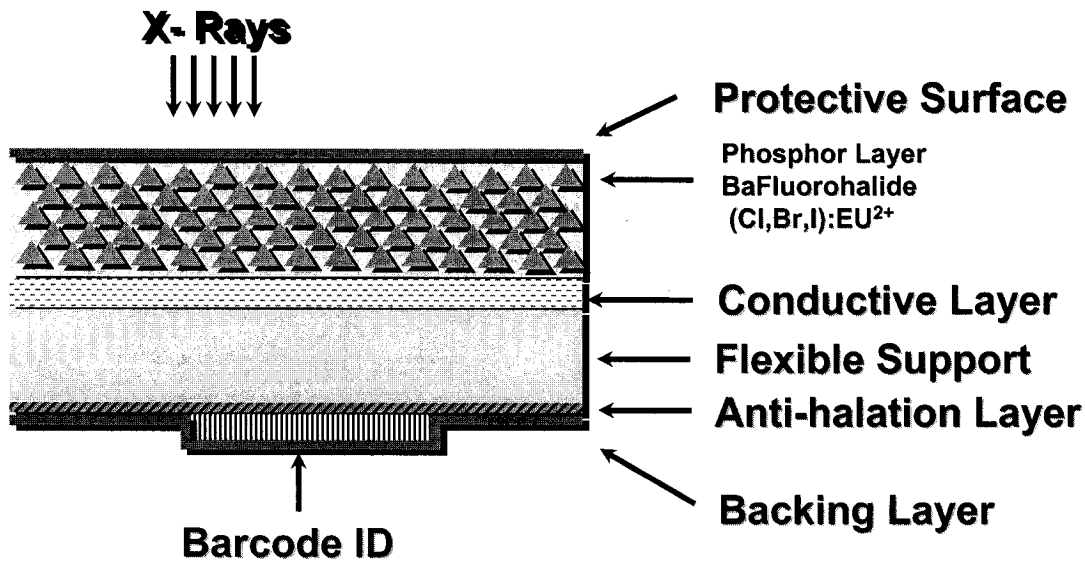

Fig. 2.12. Illustration of a basic composition of an imaging phosphor plate used in Computed Radiography.

Ionization by absorption of x-rays or UV radiation causes electron/hole pairs to be formed in the crystal as illustrated in figure 2.13. Some of these electron/hole pairs raise Eu^{2+} to an excited state and produce a prompt emission of visible light when Eu^{2+} returns to its ground state. Other energy is captured in a meta-stable state in empty lattice sites, called *F centers*. The captured electrons form the "latent image" are used to produce the computed radiograph. If the *F center* is exposed to visible light of the proper wavelength, energy is absorbed and light is emitted when the excited Eu^{2+} ions return to the Eu^{2+} ground state. This process is used to read out, in effect, to "develop", the latent image stored on the imaging plate.

Ba FX:Eu crystals have a rather broad visible absorption peak for *F center* stimulation with red light at about 600 nm. A HeNe laser (633 nm) is thus very efficient in producing the stimulating light. A semiconductor (diode) laser with output at 680 nm is also capable of harvesting the stored signal. The emitted light is blue-purple at 390 to 400 nm. Optical filtration effectively separates the stimulation and emission spectra. The emitted light intensity is significantly lower than the stimulation light intensity, thus requiring substantial amplification of the signal[14].

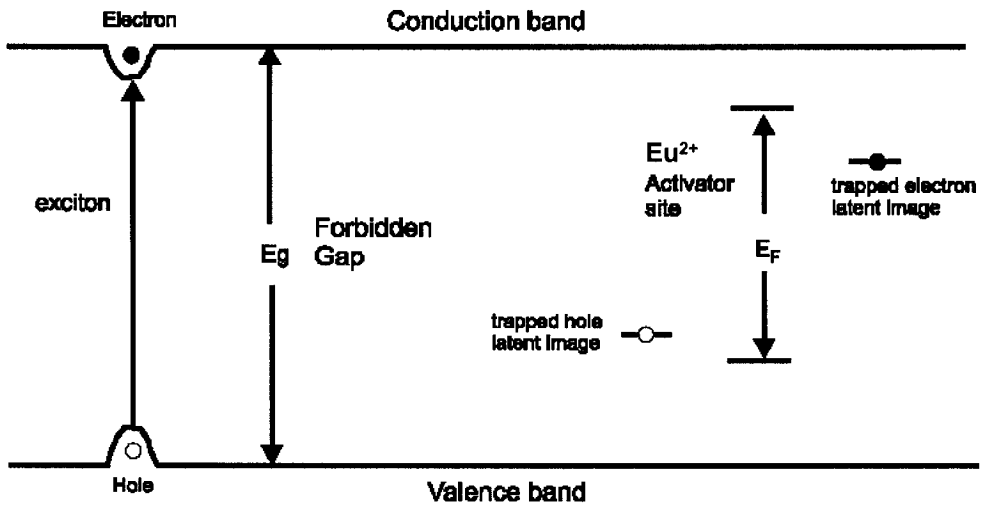

Fig. 2.14. The storage of energy and the subsequent generation of light of energy E_f in photostimulable phosphor.

The laser beam is directed at a mirror, which deflects the beam rapidly back and forth across the imaging plate either by a galvanometer or by a rotating polygon, as shown in Figure 2.15. The axis of beam deflection is called the *fast scan direction* or *scan direction*. At the surface of imaging plate the diameter of the laser distribution is approximately 100 μm. As the laser passes over the plate, the emitted intensity of blue-purple light is directly proportional to the x-ray energy absorbed in that specific area. During the scanning of the laser beam, the phosphor plate is continuously moving at a speed such that the next line scanned has sufficient sample spacing to provide equal pixel dimensions. The axis of motion of the plate is called the *slow scan direction*, or *sub scan direction*[14].

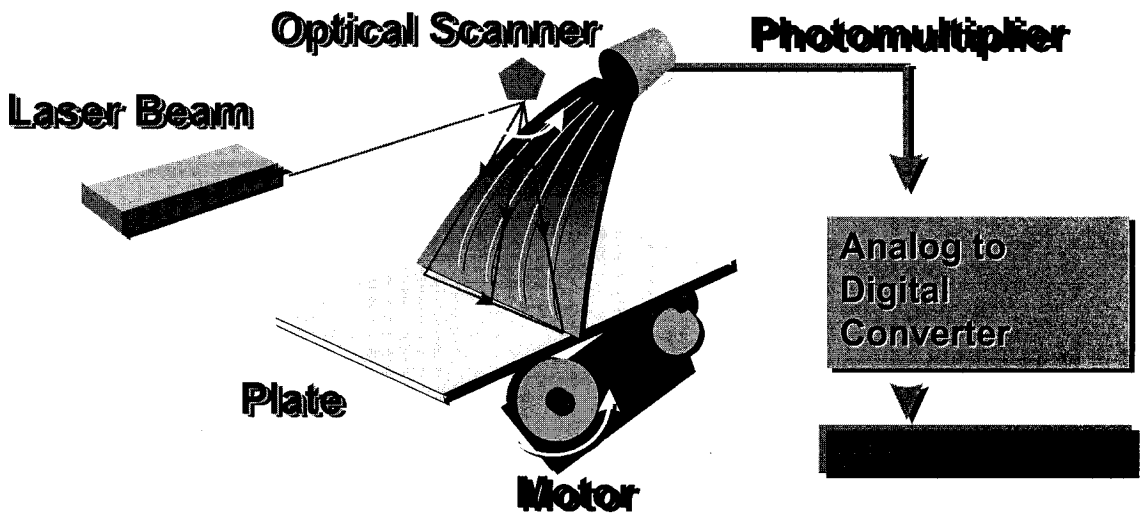

Fig. 2.15. Illustration of read out method of latent image on a Computed Radiography plate by a laser beam [14]

An optical collection system channels the emitted light to the input photocathode of one or more photomultiplier tubes (PMT). The light is filtered to have a high transmission at 390-400 nm, but is practically opaque in the vicinity of 600 nm. Light photons absorbed by the input photocathode of the PMT cause the emission of photoelectrons, which are amplified to produce a useable electrical current at the output end of the PMT. The voltage applied to the PMT (or multiple PMTs) determines the sensitivity of the system for conversion of photostimulated light intensity to electrical signal. In effect, the PMT voltage adjusts the "speed" of the system to the exposure on the imaging plate. The signal coming from the PMT will have a certain threshold value and range, determined by the voltage setting of the PMT and the range of the signal emanating from the imaging plate. An amplifier is then used to match the PMT signal range to the range of values encoded by a analog to digital converter (ADC). The amplifier is used to adjust the "latitude" of the system to the range of exposure on the imaging plate. Different strategies by the manufacturers in extracting the latent image exist. In early designs, a low energy laser beam scan of the exposed phosphor plate would determine the optimal adjustment of the PMT amplifier for subsequent digitization of the signal. In current designs, the range of the amplification is tuned and fixed to the amount of photostimulated luminescence signal expected from a typical clinical study (in

terms of incident exposure), and digitized to a wide range of possible digital values, on the order of 4000 discrete grey levels (12 bits)[14].

Computed radiography is the current state-of-the-art technology for digital image acquisition of projection images. This technology is becoming more widespread and clinically important, as it begins to replace the 100 year-old screen-film mainstay in diagnostic imaging. As mentioned above, this system was investigated with megavoltage energies in this study.

References

1. T. S. Curry III, J. E. Dowdey, R. C. Murry. *Christensen's Physics of Diagnostic Radiology* 4th Edition (Lippincott Williams & Wilkins, Media, 1990).
2. P. Munro. *The Modern Technology of Radiation Oncology*, J. Van Dyk Ed (Medical Physics Publishing, Madison, 1999).
3. P. Munro, "Portal Imaging Technology: Past, Present And Future," Semin. Radiat. Oncol. **5**,115-133, (1995).
4. H. P. Chan, and K. Doi, "Studies of x-ray energy absorption and quantum noise properties of x-ray screens by use of Monte Carlo simulation," Med. Phys. **11**, 37-46, (1984).
5. J. Leong, "Use of digital fluoroscopy as an on-line verification device in radiation therapy," Phys. Med. Biol. **31**, 985-992, (1986).
6. B. Wowk, and S. Shalev, "Thick phosphor screens for on-line portal imaging," Med. Phys. **21**, 1269-1276, (1994).
7. L. E. Antonuk, "Electronic portal imaging devices: a review and historical perspective of contemporary technologies and research," Phys. Med. Biol. **47**, R31-R65, (2002).
8. R. A. Holroyd, and D. F. Anderson, "The physics and chemistry of room-temperature liquid-filled ionization chambers," Nucl. Instr. and Meth. **A236**, 294-299, (1985).
9. M. van Herk, "Physical aspects of a liquid-filled ionization chamber with pulsed polarizing voltage," Med. Phys. **18**, 692-702, (1991).
10. Varian Oncology Systems, "Portal Vision aS500 Rel. 6 System Manual (I.D. #PV6005RM_aS500), (2000).
11. L. E. Antonuk, J. Boudry, W. Huang, D. L. McShan, E. J. Morton, and J. Yorkston, "Demonstration of megavoltage and diagnostic x-ray imaging with hydrogenated amorphous silicon arrays," Med. Phys. **19**, 1455-1465, (1992).
12. R. A. Street, R. B. Apte, S. E. Ready, R. L. Weisfield, and P. Nylen, "Amorphous silicon sensor arrays for x-ray and document imaging," Mater. Res. Soc. Symp. Proc. **487**, 1455-1466, (1997).
13. M. Partridge, P. M. Evans, M. van Herk, L. S. Ploeger, G. J. Budgell, and H. V. James, "Leaf position verification during dynamic beam delivery: a comparison of three applications using electronic portal imaging," Med. Phys. **27**, 1601-1609, (2000).
14. J. A. Seibert, "Computed Radiography Overview," presented at the Radiological Society Of North America, 84th Scientific Assembly and Annual Meeting, Chicago, (1998).

Chapter 3

Image Quality

3.1. FACTORS AFFECTING IMAGE QUALITY

It is generally accepted that the quality of images acquired using megavoltage x-rays is inherently poorer than those acquired with kilovoltage x-rays. Aside from the energy of the beam, other factors influencing the quality of the image are the acquisition time, patient motion, and the size of the x-ray source. Purpose of this section is to explain how these factors influence the portal image quality and to understand the fundamental limitations of imaging with megavoltage x-ray beams.

3.1.1. Beam Energy

Generally, the image quality in portal imaging is strongly constrained by the low contrast and limited spatial resolution possible given the nature of the high-energy radiation sources used for therapy. An important factor limiting contrast in portal imaging is the fact that x-ray attenuation is dominated by Compton interactions at therapy energies, as opposed to photoelectric interactions at diagnostic energies. The probability of Compton interactions is highly dependent on the electron density of the material, unlike photoelectric interactions, which show a strong dependence on atomic number. Since anatomical structures generally provide relatively small variations in electron density, the image contrast at therapy energies is inherently more limited than at diagnostic energies, where photoelectric interactions dominate, thereby producing high contrast between bone (high Z) and tissue (low Z) materials.

Another constraint relates to the fact that the x-ray photons that make up radiotherapy beams have a significantly lower probability of interaction with matter than the lower energy x-rays used in diagnostic imaging. As a consequence, the fraction of the radiotherapy beam that enters the detector and generates a detectable signal in the converter (called the x-ray quantum detection efficiency (*DQE*)) is typically low. For

example, it is only ~ 1% for conventional portal film used with a metal plate. By comparison, the maximum *DQE* values for diagnostic x-ray imaging systems commonly range from 20 to 80%[1].

3.1.2. *Patient motion*

Another factor that affects image quality is the patient motion. Patient motion causes an artifact called *motion blur* in the image. For example, the amount of blur in the object plane in Figure 3.1 is equal to the distance moved, *d*, during the acquisition of the image. The blur value at the receptor is larger and is in proportion to the patient detector distance. The effect of motion on each point within the object is to reduce contrast and spread the image over a larger area, as indicated in Figure 3.1.

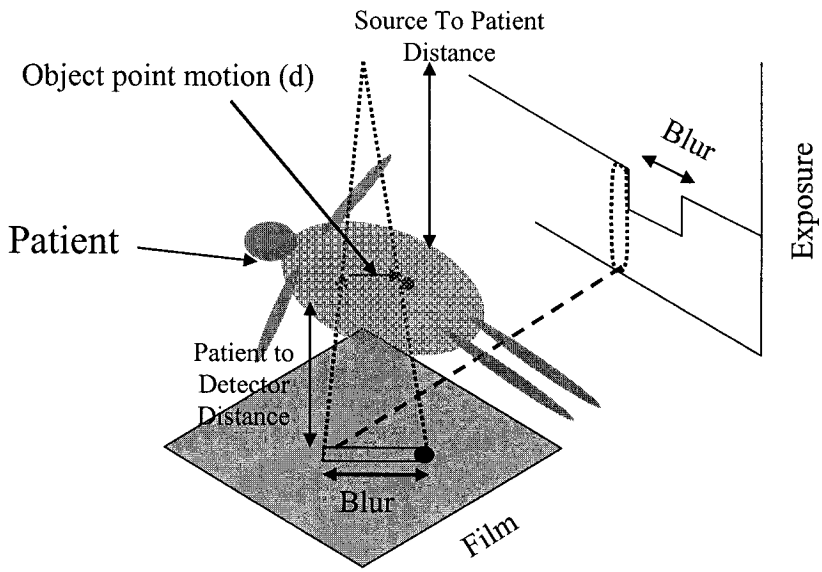

Fig. 3.1. Illustration of Motion Blur.

Motion blur can be reduced by: careful patient instruction to stay motionless during the irradiation time, short exposure times, large source to patient distance, and small patient to detector distance.

3.1.3. Source Size

All linear accelerator sources have some finite size, and this contributes to image blur and loss in spatial resolution. As mentioned before, source sizes of medical linear accelerators have been measured to be ~1 mm full width at half maximum, or smaller. Consider the example shown in figure 3.2. X-rays through each point of the object from the focal spot will diverge and form a blurred image of the object point. The blur value, with respect to the object size, is given by:

$$B_f = F \times s, \tag{3.1}$$

where F is the dimension of the source size and s is position of the object. It should be noted that the value of focal spot blur, for a given source size, is directly related to the position of the object on the s scale.

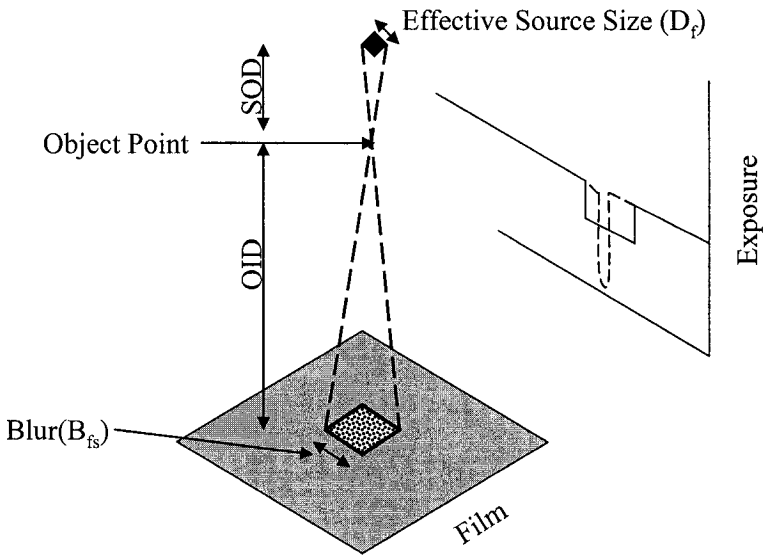

Fig. 3.2. Illustration of Blur produced by the finite source size.

where SOD is the source to object distance and OID is the object to imaging distance. If the object is in direct contact with the imager, the source size blur vanishes. As the object is moved away from the imaging plane, two things happen. Both the image and blur are magnified. The blur value is increased in proportion to the image size, causing

deterioration in image quality. This phenomenon gives another reason to position the imager as closely as possible to the patient in radiation therapy to minimize blurring.

3.2. IMAGE QUALITY PARAMETERS

Image quality of the imaging modalities is evaluated in terms of certain parameters which are measured or calculated. The rest of this section introduces these parameters.

3.2.1. Subject contrast

Contrast describes how well an object stands out from its surroundings and it is defined as:

$$C = \frac{\text{signal}}{\text{mean signal}} = \frac{\phi_{p2} - \phi_{p1}}{(\phi_{p2} + \phi_{p1} + 2\phi_s)/2}, \tag{3.2}$$

where ϕ_{p1}, ϕ_{p2}, are primary photon fluences and ϕ_s scatter photon fluence reaching the image receptor as illustrated in figure 3.2. The above equation is derived from the formalism developed by Motz and Danos[2] for their analysis of diagnostic imaging systems. In their approach, the detectability of a small anatomic structure embedded within a homogeneous body is determined. Their study considered an idealized imaging situation in which x-ray pass through a homogeneous medium of uniform thickness L having attenuation coefficient μ. On average, some photons are attenuated in the medium, some photons exit the medium without interacting at all, and a number, ϕ_s, scatter in the medium and yet are detected exiting the medium. On average, $\phi = \phi_{p1} + \phi_s$ x-ray quanta are detected as an image background of which a fraction, $SF = \phi_s/(\phi_s+\phi_{p1})$, known as the scatter fraction, is scattered.

As the figure 3.3 illustrates, embedded within the homogenous medium there is an anatomic structure having attenuation coefficient μ_x and thickness L_x such that $\phi_{p2} + \phi_s$ total x-ray quanta are detected behind the anatomic structure.

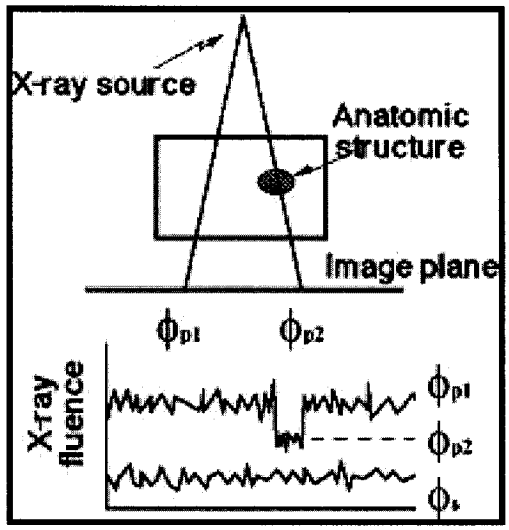

Fig. 3.3. Illustration of the image formation process and its relation to some key indicators of image quality[3].

As mentioned above, the subject contrast is defined as the ratio of signal difference between the anatomic structure and the background, to the mean carrier signal. Equation 3.2 can be rewritten as[2]:

$$C = \frac{2(1-e^{-\Delta})}{1+e^{-\Delta}+\dfrac{2SF}{1-SF}}, \tag{3.3}$$

where $\Delta = L_x(\mu_x - \mu)$ represents the difference in attenuation between the anatomic structure and the background. The equation 3.3 shows that the subject contrast increases if the difference in attenuation between the anatomic structure and the background increases, or if the scatter fraction (SF) decreases[1].

The subject contrast for 1-cm-thick cortical bone structure embedded in a 20 cm thick body of water, as a function of monoenergetic beam energy, is plotted in figure 3.4. These results have been calculated using the attenuation coefficients for bone, air, and water found in Appendix A of Johns and Cunningham[4]. For simplicity, the contrast has been calculated assuming that no x-ray scatter occurs (SF = 0). It is clear from figure. 3.4 that one of the major limitations of imaging with high energy radiation beams is low subject contrast. The subject contrast for the bony object is about 40 % when irradiated by a 50 keV x-ray beam; however, it drops to less than 4 % when irradiated by

megavoltage beams. The subject contrast is 10-20 times less at radiotherapy energies than at diagnostic energies[5].

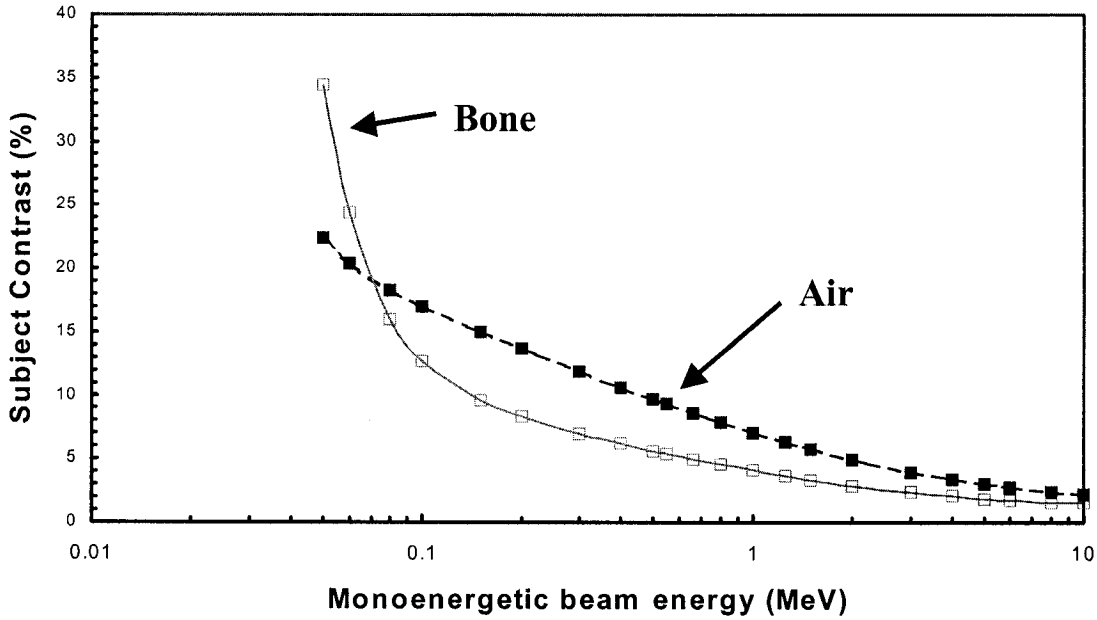

Fig. 3.4. Subject contrast as a function of monoenergetic beam energy for a 1 cm bony structure and 1 cm air cavity embedded in a 20 cm thick water medium.

Contrast is the result of difference in x-ray attenuation within the patient. As discussed above, at low energies, the photoelectric process dominates. Since the photoelectric cross section is proportional to the atomic number raised to the third power (Z^3), the higher atomic number of bone results in a larger attenuation coefficient compared to that of water. However, the photoelectric cross section is also inversely proportional to the energy cubed ($1/E^3$). Compton scattering becomes the dominant interaction process above 20 keV for soft tissues and above 50 keV for bone. The Compton scattering cross section is dependent on the electron density of a material, which, except for hydrogen, varies only slightly with atomic number. The electron density of water [ρ_e (water) = 3.34×10^{23} electron/cm^3] is comparable to that of bone [ρ_e (bone) = 5.81×10^{23} electron/cm^3]. Therefore, the difference in attenuation, and hence the contrast, reduces significantly at megavoltage energies.

3.2.2. Signal-to-Noise Ratio

The most important parameter that determines the image information content is the signal-to-noise ratio (*SNR*). A number of sources of noise contribute to *SNR*. A limiting source of noise is due to the x-ray quantum statistics. This is best explained again with the figure 3.3, which shows the process of x-ray image formation. The difference in attenuation between an object and its surroundings results in different number of x-rays reaching and interacting in an image receptor. The subject contrast is determined by the energy of the x-ray beam, the radiological properties of the object being imaged, and the amount of x-ray scatter reaching the image receptor. However, since the image formation is a statistical process involving the detection of discrete x-ray quanta, there will be a statistical uncertainty (known as x-ray quantum mottle) in the number of photons that interact in the image receptor. The detectability of the object therefore depends not only on how large the difference in attenuation is between the object and its surroundings, but also on how large this signal difference is compared to the uncertainty in the signal[3].

The number of x-ray quanta detected in some time interval follows Poisson counting statistics. For a Poisson distribution, the variance in the number of detected x-ray quanta is equal to the mean number of detected photons. Therefore, if the mean fluences are known, a signal-to-noise ratio can be calculated. The *SNR* is given by the ratio of the signal difference between an anatomic structure and its background to the statistical noise associated with detection of the x-ray quanta necessary to form this signal difference. Hence, *SNR* can be written as[3]:

$$SNR = \frac{\text{image signal}}{\text{noise}} = \frac{\phi_{p2} - \phi_{p1}}{\sqrt{(\phi_{p2} + \phi_{p1} + 2\phi_s)/2}}, \tag{3.4}$$

where all the parameters have the same meaning as defined in equation 3.2. Motz and Danos[1] have shown that the *SNR* can be rewritten as:

$$SNR = \sqrt{A\Phi_i T\eta}\,\frac{2(1-e^{-\Delta})}{\sqrt{1+e^{-\Delta}+\dfrac{2SF}{1-SF}}}, \tag{3.5}$$

where A is the area of the detector element, Φ_i is the incident fluence, T is the patient transmission, and η is the x-ray detector efficiency. Equation 3.5 shows that the *SNR*, like

the contrast, decreases as the difference in attenuation between the object and the background decreases. However, unlike the contrast, the *SNR* is proportional to the number of x-rays detected ($A\Phi_i T\eta$). In addition, scatter reduces the *SNR* by adding noise without contributing to the signal.

A typical diagnostic imaging procedure delivers a dose of 0.05 cGy to the patient[6]. For the same patient dose at megavoltage energies, the *SNR* would be ~ 100 times smaller. While the diagnostic *SNR* would satisfy the Rose's criteria for visibility (*SNR* = 5), the megavoltage beam would not. However, for the same photon fluence, a megavoltage beam delivers more dose. This simple model demonstrates, the *SNR* of the bone signal decreases rapidly with increasing energy. For the same dose to the patient, the *SNR* is much lower at megavoltage energies (2 MeV) than that at diagnostic energies (50 keV). For typical diagnostic and therapy doses of 0.05 and 10 cGy, respectively, the gap in *SNR*s is reduced. The *SNR* for diagnostic energy would be around 71 while the SNR for the therapeutic energy would be around 15[(3)].

3.2.3. *Spatial Resolution*

Another important factor that influences image quality, but which is not included in the above-described model, is spatial resolution. Spatial resolution is a measure of how the image signal is blurred by the imaging system. For example, the spatial resolution of the system influences how well the edges, such as those resulting from bones, will be detected. The spatial resolution of commercial EPIDs depends on factors that are common to all EPIDs as well as factors that are device specific. The spread of high energy particles in the metal plate is common to all commercial EPIDs and is quite modest[7, 8]. In addition to the lateral migration of high energy electrons, other processes such as x-ray scatter, bremsstrahlung, and positron annihilation, also contribute to the signal spread in the metal plate[8-10]. Once the high energy particles exit from the metal plate they can spread in the converter (phosphor screen, ionizing fluid). But the primary factor influencing the spatial resolution of the EPID systems is the pixel size of the imagers[11]. Different EPID systems provide different pixel dimensions. The smaller the pixel size of the imagers, the better the spatial resolution.

The spatial resolution of an imaging system is often characterized by examining how well the system reproduces a point object (infinitesimally small). Acquiring an image of such a point object measures the system's point spread function. Conventionally, this spread of signal is represented in the form of the modulation transfer function (*MTF*). The *MTF* describes how well the system passes different spatial frequencies and is calculated from the Fourier transform of the point spread function. Any complete characterization of an imaging system requires an examination of both the signal-to-noise characteristics and the spatial frequency response of the system.

It is a common misconception that the spatial resolution of the imaging system is the major factor limiting the image quality of portal films and portal images. Apart from the spatial resolution of the image receptor, the image quality of any portal image also depends upon the size of the x-ray source, and image magnification. Source sizes of medical linear accelerators have been measured to be ~1 mm full width at half maximum, while Co-60 sources measure approximately 2 cm in diameter. Measurements have shown that the line-spread functions for camera-based EPIDs are 0.8–1.0 mm[10, 11] full width at half maximum while that for the matrix ion chamber EPID is 1.5–2.0 mm[11]. Image magnification is variable and can have an important effect on the spatial resolution of the system. As the magnification increases, geometric blurring due to the x-ray source increases, while the size of the patient anatomy projected at the plane of the image receptor also increases, reducing the effect of blurring by the image receptor. Thus, there is an optimal image magnification where the blurring due to both the image receptor and the x-ray source is minimized.

3.2.4. *Detective Quantum Efficiency*

The detective quantum efficiency, or *DQE(f)*, gives the *SNR* transfer characteristics of an imaging system as a function of spatial frequency. Consider a system for which $SNR_{in}(f)$ is the input *SNR* and $SNR_{out}(f)$ is the output *SNR*. Then the *DQE* produced by the imaging system is defines as[1]:

$$DQE(f) = \left[\frac{SNR_{out}(f)}{SNR_{in}(f)}\right]^2, \tag{3.6}$$

The *DQE(f)* gives a measure of how efficient the imaging system is at transferring the *SNR* (i.e. information) contained in the radiation beam[1].

The image receptor should always have high quantum efficiency so that a large fraction of the incident x-ray quanta actually will interact in the receptor. In reality, portal imaging generally operates with low quantum efficiency. All commercial portal imaging systems use a metal plate (x-ray converter) to convert photons to Compton electrons. In video-based EPIDs and amorphous silicon EPIDs, a phosphor screen is used to convert the electrons into optical photons. A scanning liquid ion chamber directly detects ionization due to the electrons. While ~4% of the incident x-ray quanta interact in the metal plate, less than 1% of the incident x-ray quanta will generate electrons that exit from the metal plate, propagating quanta further down the imaging chain[5]. In fluoro based systems, quantum efficiency can be increased by increasing the thickness of the phosphor screen because the incident x-ray quanta can also interact directly with the phosphor screen[7]. Therefore, the need for phosphor screen thickness increases to increase the *DQE* of commercial EPIDs. For example, a phosphor screen thickness of 200 mg/cm^2 (in a fluoro based EPID) has a quantum efficiency ~2.5 times greater than the conventional cassettes used for portal films. A similar argument can be made for the liquid in the scanning ion chamber systems, with a liquid thickness of ~80 mg/cm^2, yielding a quantum efficiency of 1.5 relative to film[1].

However, direct approaches to increase quantum efficiency by increasing the thickness and/or density of the metal plate x-ray detectors are often ineffective. Typically, spatial resolution deteriorates due to the increased extent of the x-ray deposition region. For the commercial fluoro based EPIDs, thick phosphor screens are often employed, and in addition to the loss of spatial resolution and optical light transmission, thick screens are prone to non-uniformity in phosphor content, and thus add to the structure noise of the imaging system. It is unlikely that increasing the thickness of the phosphor screens will yield further benefits.

Even with such low detection efficiencies, much larger numbers of x-ray quanta interact with the radiation detector when forming a radiotherapy image, which partly compensates for the low subject contrast at higher x-ray energies. There are number of reasons why larger numbers of x-ray quanta reach the detector in portal imaging. Much

larger doses are delivered to a patient during a radiotherapy treatment than is considered acceptable in diagnostic radiology, resulting in a much larger photon fluence impinging on the patient. The high-energy radiation is much more penetrating so that a larger fraction of the radiation exits from the patient. In addition, primary x-ray quanta are not attenuated in the grids, as in diagnostic radiology. All of these factors result in a much greater photon fluence reaching the radiation detector in a radiotherapy beam.

3.2.5. X-ray Scatter

Scattered X rays, or any "nonprimary" photons, can reduce the subject contrast and the signal-to-noise ratio of portal images by generating signals in the image receptor that carry no geometric information about the patient's anatomy but add noise to the images. The reduction of contrast by x-ray scatter is of serious concern for portal films, since the display contrast of film cannot be adjusted to compensate for any reduction in subject contrast. For EPIDs, the reduction in signal-to-noise ratio due to x-ray scatter is more important than the reduction in contrast. While x-ray scatter has long been a major concern in kilovoltage x-ray imaging, it has been shown that it is much less of a problem for megavoltage portal imaging. As the energy of the x-ray beam increases, the scatter fraction (the fraction of the total fluence reaching the image receptor that is due to scattered x rays) decreases from 0.9 at 100 keV to less than 0.6 for a 6 MV spectrum (at the exit surface of the patient)[2]. On the other hand, the scattered component of kilovoltage beams can be reduced substantially by using grids, which is not possible for megavoltage beams. As in diagnostic radiology, geometric factors are quite important in influencing the scatter fluence reaching the image receptor at megavoltage energies. The scatter fraction increases as the patient thickness increases, as the field size increases, and as the air gap between the patient and the image receptor decreases. Apart from extreme situations such as very large patient thicknesses and field sizes, and small air gaps, x-ray scatter generally does not degrade the image quality of portal image significantly. Jaffray *et al.* have shown, using Monte Carlo calculations, that the signal-to-noise ratio would improve by less than 10% if all x-ray scatter were eliminated before reaching the image receptor when a moderately thick (20 cm) patient is irradiated[12].

3.2.6. Characteristic Curve

It is necessary to understand the relationship between the incident radiation intensity a portal image receives and the intensity or pixel value produced by this incident radiation. The relationship between the incident radiation and intensity is plotted as a curve, known as the "characteristic curve" and it can provide information about dose response of the detector. In addition, it also gives a crucial understanding on detector contrast, and imaging applications other than position verification, such as monitoring exit dose of patient treatment, automating compensator design, and conducting various quality assurance programs[13]. The amorphous silicon EPID and the fluoro based EPID respond linearly with incident radiation while the liquid matrix EPID and the film system respond non-linearly with incident radiation[13-16]. The curves also vary with varying energies for the same imaging systems illustrating that dose response is also dependant on the photon energy. In addition, the characteristic curves may also vary with acquisition modes of the EPIDs.

References

1. A. L. Boyer, L. Antonuk, A. Fenster, M. Van Herk, H. Meertens, P. Munro, L. E. Reinstein, and J. Wong, "A review of electronic portal imaging devices (EPIDs)," Med. Phys. **19**, 1-16, (1992).
2. J. W. Motz, and M. Danos, "Imaging information content and patient exposure," Med. Phys. **5**, 8-22, (1978).
3. M. G. Herman, J. M. Balter, D. A. Jaffray, K. P. McGee, P. Munro, S. Shalev, M. Van Herk, and J. W. Wong, "Clinical use of electronic portal imaging: Report of AAPM Radiation Therapy Committee Task Group 58," Med. Phys. **28**, 712-737, (2001).
4. H. E. Johns and J. Cunningham, The Physics of Radiology 4th Edition (Charles C. Thomas, Sprignfield, 1983).
5. L. E. Antonuk, "Electronic portal imaging devices: a review and historical perspective of contemporary technologies and research," Phys. Med. Biol. **47**, R31-R65, (2002).
6. D. W. Rogers, "Fluence to dose equivalent conversion factors calculated with EGS3 for electrons from 100 keV to 20 GeV and Photons from 11 keV to 20 GeV," Health Phys. **46**, 891-914, (1984).
7. R. T. Droega, "A megavoltage MTF measurement technique for meatl screen-film detectors," Med. Phys. **6**, 272-279, (1979).
8. P. Munro, J. A. Rawlinson, and A. Fenster, "Therapy imaging: Limitations of imaging with high energy x-ray beams," Proc. SPIE. **767**, 178-184, (1987).
9. B. Wowk and S. Shalev, "Thick phosphor screens for on-line portal imaging," Med. Phys. **21**, 1269-1276, (1994).
10. P. Munro, J. A. Rawlinson, and A. Fenster, "Therapy imaging: A signal-to-noise analysis of a fluoroscopic imaging system for radiotherapy localization," Med. Phys. **17**, 763–772, (1990).
11. M. van Herk and H. Meertens, "A matrix ionization chamber imaging device for on-line patient setup verification during radiotherapy," Radiother. Oncol. **11**, 369–378, (1988).
12. D. A. Jaffray, J. J. Battista, A. Fenster, and P. Munro, "X-ray scatter in megavoltage transmission radiography: Physical characteristics and influence on image quality," Med. Phys. **21**, 45–60, (1994).
13. F. F. Yin, M. C. Schell, and P. Rubin, "Input/output characteristics of a matrix ion-chamber electronic portal imaging device," Med. Phys. **21**, 1447-1454, (1994).
14. E. E. Grein, R. Lee, and K. Luchka, "An investigation of a new amorphous silicon electronic portal imaging device for transit dosimetry," Med. Phys. **29**, 2262-2268, (2002).
15. B. M. C. McCurdy, K. Luchka, and S. Pistorius, "Dosimetric investigation and portal dose image prediction using an amorphous silicon electronic portal imaging device," Med. Phys. **28**, 911-924, (2001).
16. Y. Zhu, X. Q. Jiang, and J. Van Dyk, "Portal dosimetry using a liquid ion chamber: Dose response studies," Med. Phys. **22**, 1101-1106, (1995).

Chapter 4

Portal Imaging Dosimetry

4.1. Dosimetric Treatment Verification

In addition to geometric precision, the treatment outcome also depends critically on the dose delivered to the target volume and healthy tissue. The overall accuracy in delivered dose can only be assessed directly by means of *in vivo* dosimetry: measurement during treatment. The dose can be measured in or at the entrance and/or at the exit side of the patient.

As early as in 1932 routine patient dose measurements using small ionization chambers were performed by Sievert[1]. In 1960s and 1970s thermoluminescene dosimetry (TLD) was introduced for the determination of absorbed dose in routine therapy[1, 2, 3]. Rudén evaluated the use of TLDs for *in vivo* dosimetry and reported an average deviation between measured entrance dose and prescribed dose of 0.6% for 619 measurements[3].

In 1990s, encouraged by the work of Rikner *et al.*[4, 5], the use of semiconductor detectors for *in vivo* dosimetry was investigated[6-21]. The main advantage of semiconductor detectors over TLD detectors is the absence of a time delay between patient irradiation and availability of measurement results, allowing an immediate check of all treatment parameters when an error in dose delivery is detected. This eases identification of the sources of the error. Nilsson *et al.* reported on entrance dose measurements by means of semiconductor detectors for 1,918 treatment fields with high energy x-ray beams, involving 43 patients[19]. They found on average, the deviation between measured absorbed dose to prescribed absorbed dose was about 5.0%. This large deviation between the measured and the prescribed dose was attributed to an incorrect estimation of the scatter dose contribution by treatment planning system.

There are several drawbacks of using TLDs and semiconductor detectors for *in vivo* dosimetry. For example, both types of detectors act as build-up material and thus

increase the skin dose. Moreover, placing a semiconductor on the skin of a patient leads to an increase in temperature and consequently a change in sensitivity of the detector. Finally, the treatment time increases due to the time needed to position the diodes on the patient. The increase in treatment time per session is reported to be 1-2 minutes if only the entrance dose is measured[22].

Because of the drawbacks that are mentioned above for *in vivo* dosimetry using TLDs and diodes, much research is being done to implement EPID systems to perform *in vivo* dosimetry in clinics.

4.2. DOSIMETRIC APPLICATION OF EPIDS

Several studies on dosimetric applications of EPIDs have been performed: Kirby and Williams have evaluated the possibilities for the assessment of the field flatness of a treatment unit with a Philips SRI-100 (Philips Medical Systems, Crawley, UK) EPID[23]. They also programmed the SRI-100 to act as an integrating dosimeter by manually controlling gain and black level settings[29]. This mode allowed the verification of segmented modulated treatment fields. Yin *et al.*[24] have studied the use of an EPID for measurement of patient transmissions for the design of tissue compensators for breast and lung cancer patients. Dirkx *et al.* used the SRI-100 for daily quality control of the absolute output and field flatness of the 25 MV photon beam of an MM50 racetrack microtron; daily measurements were performed for four different gantry angles[25]. Heijmen *et al.*[26-28], Leong[30], Swindell[31], Wong *et al.*[32] and Ying *et al.*[33] have also performed studies related to the use of an EPID for on-line dosimetric quality control of treatments *(in vivo* dosimetry).

Using an EPID for *in vivo* dosimetry has the following potential advantages in comparison with the usually applied silicon diodes: (i) Dosimetric data are obtained for a full plane, i.e. not only in a single or a few points. (ii) Dosimetric data are simultaneously obtained with patient positioning data which facilitates the interpretation of the dosimetric data. (iii) *In vivo* dosimetry with an EPID that is already in use for patient positioning verification does not lead to increased treatment times. (iv) There is no physical contact between the patient and the detector.

Moreover, exit dosimetry has also proven to be a useful approach to the verification of dynamic collimation used in the delivery of intensity modulated fields, as well as the verification of compensator design with the goal of comparing the integrated dose with planned dose distribution. In addition, the patient mid-plane or exit dose can be predicted from the portal dose distribution generated by EPIDs, if a 3D CT data-set is known and the model for calculating the exit portal dose is accurate. However, the primary radiation cannot be simply ray traced through the 3D CT data-set to get the patient mid-plane dose since the contribution of scattered radiation must be included. In the next section, we'll look at how each imaging systems acquires the images and the physics relating the acquired signal to mid-plane dose.

4.3. AMORPHOUS SILICON EPID

4.3.1. Signal response

Studies have shown that amorphous silicon EPID respond linearly with dose[34, 35]. As mentioned previously, the charge collected by the amplifier is proportional to the light reaching the photodiode. Number of light photons generated in the phosphor screen is proportional to the energetic electrons interacting with the screen. Finally, the number of energetic electrons created is proportional to number of incident photons interacting with the copper plate. This leads to the conclusion that number of charges collected by the amplifier is proportional to the number of incident photons interacting with the copper plate. In theory, if we were to increase the number of photons impinging on the detector by increasing MUs delivered by the linear accelerator, the central axis intensity or the pixel value of the image should increase linearly. But in practice, all the imagers have gain corrections to ensure that an image does not become saturated.

In order to verify this linear response of the detector, images have to be taken with increasing lead thicknesses. Ion chamber readings can be taken with an identical set up to obtain the dose at the detector position. Central pixel value of the images can be plotted with corresponding dose values obtained by the ion chamber to give the signal response of the detector as a function of dose received by the detector.

4.3.2. *Application to dosimetry*

Intensity modulated radiotherapy (IMRT) is a rapidly evolving field and it requires extensive quality assurance. Since amorphous silicon EPIDs can acquire about 20 frames per second, it is conceivable that these devices could be employed for step and shoot dose distribution measurements in IMRT. An IMRT treatment can contain about 40-60 sub-fields with each delivering about 3-4 MUs. Because of the fast acquisition time, frames could be acquired for the entire duration of the treatment giving a final intensity map. Unlike ion chamber measurements, which give only point measurements, the final intensity map gives an intensity distribution for the entire plane. A single point in the intensity map could be normalized with an ion chamber measurement at the same location to give a dose map of the IMRT treatment.

Another simple, yet effective application for a-Si EPID was discussed by Wong *et al.*, [32] and more recently demonstrated by Kroonwijk *et al.*, [36] consists of a direct comparison of a measured portal dose image with a theoretically predicted portal dose image. Discrepancies between the measured and predicted image indicate treatment delivery errors, which may be corrected once identified. Ideally the comparison step would be fully computerized using software and performed within the first few monitor units delivered in a treatment fraction.

Another dosimetric treatment verification application of a-Si EPID involves the removal of scatter from the measured portal image, then backprojecting the remaining primary component through the patient computed tomography (CT) data set which allows a calculation of deposited dose in the patient[37, 38]. Others have used simpler approaches to relate measured portal images with patient mid-plane and/or exit dose estimates. Some studies have been done for determination of pseudo-CT slices for breast cancer patients for derivation of tissue compensators to obtain a homogeneous dose distribution in the target[39, 40].

Hansen *et al.* derived the primary fluence from a measured a-Si portal dose image and back projected that fluence through patient to yield the primary fluence distribution in the patient[41]. This distribution was then convolved with dose deposition kernels to derive the dose distribution in the patient. Moreover, Boellaard *et al.* have developed a

convolution model to convert measured portal dose images into exit dose distributions[42]. Later the model was extended to derive the mid-plane dose in the patient, which then can be compared with the dose calculated by treatment planning software.

4.4. LIQUID ION MATRIX EPID

4.4.1. *Signal response*

Due to the relatively long scan time (2.76 seconds) to acquire an image, liquid matrix EPID can only measure dose rate. To derive absolute dose, a conversion of the measured dose rate image is necessary, which requires a continuous read out of the monitor chamber signal of the accelerator during image acquisition and number of MU given during the irradiation fraction[44]. The Relationship between the pixel value I of the image obtained with LC-250 liquid matrix EPID and the dose rate $\dot{D}$ is given by[45]:

$$I = a\dot{D}^{1/2} + b\dot{D}, \tag{4.1}$$

where a and b are parameters with units $(\text{min/cGy})^{1/2}$ and (min/cGy), respectively. At low dose rates (< 100 cGy/min) the dependence is accurately described by a square root term is determined by the ionization of the liquid and recombination of the ions in the liquid. Application of a high voltage on the chambers disturbs the ion concentration resulting in the linear term.

4.4.1.1. *Dependence of ion pair concentration on dose rate*

The variation of free ion pair concentration $n(t)$ with time for the liquid filled ion chambers of the EPID is given by van Herk[46]:

$$\frac{dn(t)}{dt} = N_{in} - \alpha n(t)^2, \tag{4.2}$$

where N_{in} is the number of free ion pairs per unit volume produced per unit time in the liquid of the EPID and α is a recombination constant. The first part of the right hand side of the equation represents the production of free ion pairs in the liquid and it is proportional to the dose rate $\dot{D}$. The second term represents the loss of ion pairs due to recombination. By solving the differential equation (4.2), the free ion pair concentration

is found. In the steady state, $dn(t)/dt = 0$ and the ion pair concentration, using equation (4.2), reaches the equilibrium value n_{eq} given by:

$$n_{eq} = (N_{in} / \alpha)^{1/2}. \tag{4.3}$$

The free ion pair concentration in the liquid-filled chambers of the EPID is thus proportional to the square root of the dose rate.

4.4.2. *Application to dosimetry*

The dosimetric characteristics of this EPID have been investigated by several groups[43-48] but so far no applications of the liquid filled EPID have been published. One of the major reasons being the long acquisition time of this EPID. Even in the fastest acquisition mode, the read-out time for one image is about 1.5 seconds and this makes it almost impossible to verify intensity profiles for treatments such as IMRT. Maximum leaf speeds during Dynamic Multileaf Collimator (DMLC) treatments on various treatment machines are between 1 and 3 cm per second at isocenter. Acquisition time is too long to acquire enough frames of the beam to accurately reconstruct the arbitrary intensity profiles produced with DMLC.

Moreover, liquid chamber EPID is a non-linear device as illustrated above and it responds to dose rate, not dose. For this reason, the dose rate of the linear accelerator has to be constant during any dosimetry measurement. Plus, the relative sensitivity of individual pixels in the device can vary. In order to measure accurate dosimetric quantities, the liquid ion chamber EPID has to be calibrated carefully.

4.5. FLUORO BASED EPID

4.5.1. *Signal response*

The fluoro EPID also responds linearly with dose as do amorphous silicon EPID. Several studies have shown this relationship between pixel value and dose[49, 50]. The authors start by showing that the signal received by the camera is proportional to the total light output during irradiation. This effect is demonstrated by increasing the integration time on the CCD camera and the number of video frames over which the image is

averaged. Since fluoro EPIDs use the same mechanism to create light photons as a-Si EPID, the explanation on how generation of light photons are proportional to incident x-rays interacting with the metal plate is valid here as well.

4.5.2. *Application to dosimetry*

Considerable empirical and theoretical research has been directed toward optimizing the performance of conventional camera–mirror–lens-based EPID systems. For example, variations in the thickness or geometry of the metal plate and/or the phosphor screen have been studied in order to understand the effect upon DQE[51-53]. They found that thicker metal plate stop more x-rays but do not necessarily lead to more electrons entering the phosphor; thicker phosphor screens stop more x-rays and generate more light signal but degrade spatial resolution. In addition, the use of a large aperture lens improves the optical transfer efficiency but such large lenses introduce spherical aberrations (which reduce spatial resolution) and distortion, among other effects. An alternative strategy to partially compensate for poor light collection efficiency involves the reduction of system noise so as to improve the signal-to-noise ratio. This has been explored through extended integration of the light signal on the sensor of the camera (as opposed to digital averaging of frames acquired at the normal video rate)[51]. Yet another approach to improving the performance of camera–mirror–lens-based systems involves the incorporation of a high-gain camera (incorporating avalanche-multiplication) so as to reduce the relative importance of the camera noise[54]. As a result of such efforts, the maximum DQEs achieved for camera–mirror–lens based EPID systems using a metal plate/phosphor screen are reported to be as high as ~1%.

Several studies on dosimetric applications of this type of EPIDs have been performed. As mentioned previously Kirby and Williams have evaluated possibilities for the use of the SRI-100 EPID for quality control checks on the beam profile of a treatment unit[23]. Leong[30] and Wong *et al*[32]. have proposed to compare a portal dose image (PDI) - i.e. a dose distribution behind a patient in a plane perpendicular to the beam axis, measured during treatment with an EPID - with a corresponding predicted PDI. For a Co 60 beam, Wong *et al.* have assessed the accuracy of the delta volume method for prediction of PDIs in a plane close behind the patient[32]. McNutt *et al.* have used the

convolution/superposition method, based on precalculated Monte Carlo data, to predict the dose distribution throughout an extended volume which includes the patient and the EPID[55]. The calculated dose distribution in the EPID is then extracted, yielding a predicted PDI. These studies have been limited to small field sizes where glare is a small fraction of the total signal. These encouraging results cannot be extrapolated to other clinical dosimetric studies where glare would be expected to be larger fraction of the total optical signal. Therefore, the use of Fluoro based EPID for transit dosimetry has been very limited. Research has to be done to over come the glare issue for Fluoro based EPID to be used as a transit dosimeter device.

4.6. FILM

Film dosimetry has some important advantages over the widely applied thermoluminescent, and semiconductor techniques. Advantages are: (i) An enormous reduction in measuring time due to the simultaneous measurements for all points in the plane of the film. (ii) A very high spatial resolution. (iii) The possibility of dose measurements in full planes in heterogeneously composed solid phantoms.

Compared to EPID systems, films have been very well established for dosimetric purposes. For quality assurance for techniques such as IMRT, films are being used widely in the clinics. It is necessary to understand the relationship between the exposure or dose received by the film and film blackness called *density*.

4.6.1. Hurter and Driffield curve (H & D curve)

The relationship between exposure a film receives and density is plotted as a curve, known as H & D curve (named after F. Hurter and V. C. Driffield, who published such a curve in England in 1890)[56]. Film density is plotted on the vertical axis and film exposure or dose is plotted on the horizontal axis. These curves are derived by giving a film a series of known doses, developing the film, and plotting the resulting density against the known doses. The actual dose a film receives can be determined by irradiating an ion chamber in the same location and with same set-up as the film.

Studies have shown that the H & D curve for Kodak XV (Kodak Company, Rochester NY) film is concave down in shape and starts to saturate at a dose around 150 cGy[57-59] as illustrated in figure 4.1. Kodak has released a new type of film, Kodak extended dose range (Kodak EDR) for dosimetry purposes. Compared to most x-ray films, it is relatively insensitive to x-ray energies and has a response which extends to very high exposures. A recent study shows that sensitometric response of Kodak EDR film increases linearly with dose until approximately 350 cGy[57]. Above 350 cGy, the gradient of the curve decreases as evident from figure 4.1. This study also shows that EDR film increases in sensitivity with increase in energy at higher doses.

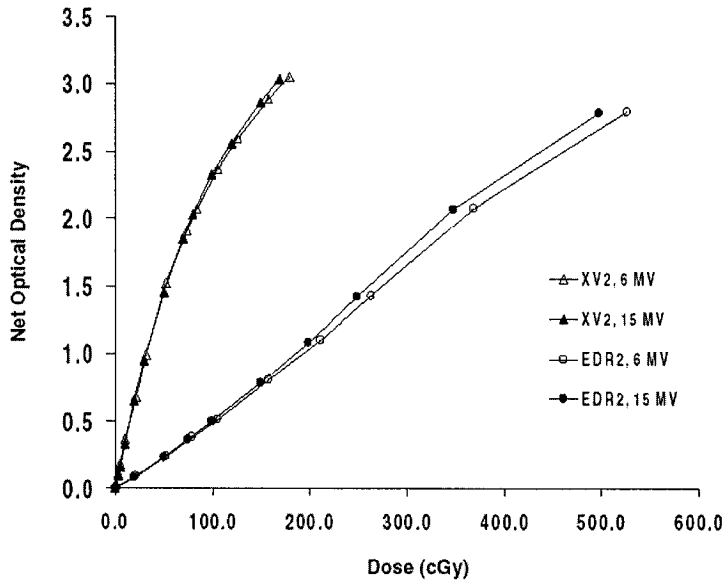

Fig. 4.1. Illustration of sample H & D curve for both Kodak XV and Kodak EDR films at 6 and 15 MV photon beam.

4.6.2. Application to dosimetry

Radiation therapy dosimetric studies using radiographic film have been performed since the introduction of cobalt-60 teletherapy and high energy betatrons for clinical use. As mentioned previously, films can be used to obtain 2 dimensional exit dose distributions. Film is potentially the ideal detector for determining dose distributions of dynamic beams and for studying combinations of stationary beams.

Films are used widely for IMRT quality assurance since 2-D dose distributions can be obtained at different planes. The integrating capability, and high resolution, makes film an ideal dosimeter for IMRT dynamic delivery quality assurance.

References

1. J. Chavaudra, G. Marinello, A. M. Brule, and J. Nguyen, "Practical use of lithium borated in thermoluminecent dosimetry," J Radiol Electrol Med Nucl. **37**, 435-445, (1976).

2. J. R. Cameron, N. Suntharalingam, and G. N. Kenney, *Themoluminecent Dosimetry* (University Wisconcin Press, Madison, 1968).

3. B. I. Rudén, "Evaluation of the clinical use of TLD," Acta Radiol. Ther. Phys. Biol. **15**, 447-464, (1976).

4. E. Grusell, and G. Rikner, "Evaluation of temperature effects in p-type silicon detectors," Phys. Med.Biol. **31**, 527–534, (1986).

5. A. Rizzotti, C. Compri, and G. F. Garusi, "Dose evaluation to patients irradiated by 60 Co beams, by means of direct measurement on the incident and on the exit surfaces," Radiother. Oncol. **3**, 279–283, (1985).

6. AAdeyemi, and J. Lord, "An audit of radiotherapy patient doses measured with in vivo semiconductor detectors," The Brit. J of Radio. **70**, 399–408, (1997).

7. M. Ciocca, L. Landoni, C. Italia, P. Montanaro, P. Canesi, and R. Valdagni, "Quality control in the conservative treatment of breast cancer: patient dosimetry using silicon detectors," Radiother.Oncol. **22**, 304–307, (1991).

8. M. Essers, R. Keus, J. H. Lanson, and B. J. Mijnheer, "Dosimetric control of conformal treatment of parotid gland tumors," Radiother. Oncol. **32**, 154–162, (1994).

9. M. Essers, J. H. Lanson, G. Leunens, T. Schnabel, and B. J. Mijnheer, "The accuracy of CT-based inhomogeneity corrections and in vivo dosimetry for the treatment of lung cancer," Radiother.Oncol. **37**, 199–208, (1995).

10. M. Essers, J. H. Lanson, and B. J. Mijnheer, "In vivo dosimetry during conformal therapy of prostatic cancer," Radiother. Oncol. **29**, 271–279, (1993).

11. M. Essers and B. J. Mijnheer, "In vivo dosimetry during external photon beam radiotherapy," Int. J.Radiat. Oncol. Biol. Phys. **43**, 245–259, (1999).

12. S. Heukelom, J. H. Lanson, and B. J. Mijnheer, "Comparison of entrance and exit dose measurements using ionization chambers and silicon diodes," Phys. Med. Biol. **36**, 47–59, (1991).

13. S. Heukelom, J. H. Lanson, G van Tienhoven, and B. J. Mijnheer, "In-vivo dosimetry during tangential breast treatment," Radiother. Oncol. **22**, 269–279, (1991).

14. T. Lahtinen, H. Puurunen, P. Simonen, A. Pekkarinen, and A. Väänänen, *Dosimetry in radiotherapy* (International Atomic Energy Agency, Vienna, 1988).

15. G. Leunens, J van Dam, A. Dutreix, and E van der Schueren, "Quality assurance in radiotherapy by in vivo dosimetry. 1. Entrance dose measurements, a reliable procedure," Radiother. Oncol. **17**, 141–151, (1990).

16. G. Leunens, J van Dam, A. Dutreix, and E van der Schueren, "Quality assurance in radiotherapy by in vivo dosimetry. 2. Determination of the target absorbed dose," Radiother. Oncol. **19**, 73–87, (1990).

17. G. Leunens, J. Verstraete, J van Dam, A. Dutreix, and E van der Schueren, "In vivo dosimetry for tangential breast irradiation: role of the equipment in the accuracy of dose delivery," Radiother.Oncol. **22**, 285–289, (1991).

18. C. Mitine, G. Leunens, J. Verstraete, N. Blanckaert, J. Van Dam, A. Dutreix, and E. van der Schueren, "Is it necessary to repeat quality control procedures for head and neck patients?," Radiother. Oncol. **21**, 201–210, (1991).

19. B. Nilsson, B. I. Rudén, and B. Sorcini, "Characteristics of silicon diodes as patient dosemeters in external radiation therapy," Radiother. Oncol. **11**, 279–288, (1988).

20. A. Noel, P. Aletti, P. Bey, and L. Malissard, "Detection of errors in individual patients in radiotherapy by systematic in vivo dosimetry," Radiother. Oncol. **34**, 144–151, (1995).

21. A. Rizzotti, G. Anselmo, and G. P. Glasgow, "Multiple simultaneous bilateral urothelial tumours of the renal pelvis," Br. J. Urol. **4**, 312–315, (1987).

22. P. C. Lee, J. M. Sawicka, and G. P. Glasgow, "Patient dosimetry quality assurance program with a commercial diode system," Int. J. Radiat. Oncol. Biol. Phys. **29**, 1175–1182, (1994).

23. M. C. Kirby and P. C. Williams, "The use of an electronic portal imaging device for exit dosimetry and quality control measurements," Int. J. Radiat. Oncol. Biol. Phys. **31**, 593–603, (1995).

24. F. F Yin, M. C. Schell, and P. Rubin, "A technique of automating compensator design for lung inhomogeneity correction using an electronic portal imaging device," Med. Phys. **21**, 1729–1732, (1994).

25. M. L. P. Dirkx, M. Kroonwijk, J. C. J. deBoer, and B. J. MHeijmen, "Daily dosimetric quality control of the MM50 racetrack microtron using an electronic portal imaging device," Radiother. Oncol. **37**, 55–60, (1995).

26. B. J. M. Heijmen, K. L. Pasma, MKroonwijk, A. GVisser, and H. Huizenga, "Prediction of portal dose images for in vivo dosimetry in radiotherapy," Med. Phys. **22**, 992, (1995).

27. B. J. M. Heijmen, J. C. Stroom, H. Huizenga, and A. G. Visser, "Application of a fluoroscopic portal imaging system with a CCD camera for accurate in-vivo dosimetry," Med. Phys. **20**, 870, (1993).

28. B. J. M. Heijmen, A. G. Visser, and H. Huizenga, "In-vivo dose measurements using an electronic portal imaging device: a feasibility study," Radiother. Oncol. **24**, (supplement):S25, (1992).

29. M. C. Kirby and P. C. Williams, "Clinical aaplications of composite and realtime megavoltage imaging," Cli. Oncol. **7**, 308–316, (1995).

30. J. Leong, "Use of digital fluoroscopy as on-line verification device in radiation therapy," Phys. Med. Biol. **31**, 985–992, (1986).

31. W. Swindell, "Transit dosimetry," Brit J. Radiol. **66**, 1077, (1993).

32. J. W. Wong, E. D. Slessinger, R. E. Hermes, C. J. Offutt, T. Roy, and M. W. Vannier, "Portal dose images I: Quantitative treatment plan verification," Int. J. Radiat. Oncol. Biol. Phys. **18**, 1455–1463, (1990).

33. X. Ying, L. Y. Geer, and J. W. Wong, "Portal dose images II: Patient dose estimation," Int. J. Radiat. Oncol. Biol. Phys. **18**, 1465–1475, (1990).

34. E. E. Grein, R. Lee, and K. Luchka, "An investigation of a new amorphous silicon electronic portal imaging device for transit dosimetry," Med. Phys. **29**, 2262-2268, (2002).

35. B. M. C. McCurdy, K. Luchka, and S. Pistorius, "Dosimetric investigation and portal dose image prediction using an amorphous silicon electronic portal imaging device," Med. Phys. **28**, 911-924, (2001).

36. M. Kroonwijk, K. L. Pasma, S. Quint, P. C. M. Koper, A. G. Visser, and B. J. M. Heijmen, "In vivo dosimetry for prostate cancer patients using an electronic portal imaging device (EPID); detection of internal organ motion," Radiother. Oncol. **49**, 124-132, (1998).

37. V. N. Hansen, P. M. Evans, and W. Swindell, "Extraction of primary signal from EPIDs using only forward convolution," Med. Phys. **24**, 1477-1484, (1997).

38. T. McNutt, T. R. Mackie, P. Reckwerdt, and N. Papanikolaou, "Calculation of portal dose distributions from portal dose images using the convolution/superposition method," Med. Phys. **23**, 1381-1392, (1996).

39. P. M. Evans, E. M. Donovan, N. Fenton, V. N. Hansen, I. Moore, M. Partridge, S. Reise, B. Suter, J. R. Symonds-Tayler, and J. R. Yarnold, "Practical implementation of compensators in breast radiotherapy," Radiother. Oncol. **49**, 255–265, (1998).

40. P. M. Evans, V. N. Hansen,W. P. MMayles, W. Swindell, M. Torr, and J. R. Yarnold, "Design of compensators for breast radiotherapy using electronic portal imaging," Radiother. Oncol. **37**, 43–54, (1995).

41. V. N. Hansen, P. M. Evans, and W. Swindell, "The application of transit dosimetry to precision radiotherapy," Med. Phys. **23**, 713–721, (1996).

42. R. Boellaard, M. van Herk, and B. J. Mijnheer, "A convolution model to convert transmission dose images to exit dose distributions," Med. Phys. **24**, 189–199, (1997).

43. M. van Herk, "Physical aspects of a liquid-filled ionization chamber with pulsed polarizing voltage," Med. Phys. **18**, 692-702, (1991).

44. R. Boellaard, "In vivo dosimetry with a liquid-filled electronic portal imaging device," PhD thesis, Free University, Amsterdam, (1998).

45. M. Essers, B. R. Hoogervorst, M. van Herk, H. Lanson, and B. J. Mijnheer, "Dosimetric characteristic of a liquid-filled portal imaging device," Int. J. Radiat. Oncol. Biol. Phys. **33**, 1265-1272, (1995).

46. R. Boellaard, M. van Herk, and B. J. Mijnheer, "The dose response relationship of a liquid-filled electronic portal imaging device," Med. Phys. **23**, 1601-1611, (1996).

47. Y. Zhu, X. Q. Jiang, and J. V. Dyk, "Portal dosimetry using ion chamber matrix: Dose response studies," Med. Phys. **22**, 1101-1106, (1995).

48. R. Boellaard, M. van Herk, and B. J. Mijnheer, "First clinical test using a liquid-filled electronic portal imaging device and convolution model for the verification of the midplane dose," Radiother. Oncol. **47**, 303-312, (1998).

49. J. Leong, "A method for consistent precision radiation therapy," Radiother. Oncol. **3**, 89-92, (1985).

50. M. C. Kirby, and P. C. Williams, "The performance of a fluoroscopic electronic portal imaging device modified for portability," Br. J. Radiol. **72**, 1000-1005, (1999).

51. P. Munro, J. A. Rawlinson, and A. Fenster, "Therapy imaging: A signal to noise analysis of a fluoroscopic imaging system for radiotherapy localization," Med. Phys. **17**, 673-772, (1990).

52. T. Radcliffe, G. Barnea, B. Wowk, R. Rajapakshe, and S. Shalev, "Monte Carlo optimization of metal/phosphor screens at megavoltage energies," Med. Phys. **20**, 1161-1169, (1993).

53. B. Wowk, S. Shalev, and T. Radcliffe, "Grooved phosphor screens for on-line portal imaging," Med. Phys. **20**, 1641-1651, (1993).

54. G. Pang, and J. A. Rowlands, "Electronic portal imaging with an avalanche-multiplication-based video camera," Med. Phys. **27**, 676-684, (2000).

55. T. R. McNutt, T. R. Mackie, P. Reckwerdt, and B. R. Paliwal, "Modeling dose distributions from portal dose images using the convolution/superposition method," Med. Phys. **23**, 1381–1392, (1996).

56. T. S. Curry III, J. E. Dowdey, R. C. Murry. *Christensen's Physics of Diagnostic Radiology 4th Edition* (Lippincott Williams & Wilkins, Media, 1990).

57. I. J. Chetty, and P. M. Charland, "Investigation of Kodak dose range (EDR) film for megavoltage photon beam dosimetry," Phys. Med. Biol. **47**, 3629-3641, (2002).

58. R. L. Stern, B. A. Fraass, A. Gerhardson, D. L. McShan, and K. L. Lam, "Generation and use of measurement-based 3-D dose distributions for 3-D dose calculation verification," Med. Phys. **19**, 165-173, (1992).

59. L. J. van Battum, and B. J. M. Heijmen, "Film dosimetry in water in 23 MV therapeutic photon beam," Radiother. Oncol. **34**, 152-159, (1995).

Chapter 5
Materials And Method

5.1. INTRODUCTION

In this chapter, procedures to obtain and evaluate the image quality parameters of each of the detectors are outlined. Moreover, all the radiation delivery devices as well as the imaging devices employed in this project will be discussed. A method is proposed for performing IMRT dose verification for patient plans with the aS-500 EPID, employing Kodak XV film as a standard for comparison.

5.2. RADIATION DELIVERY SYSTEMS

A total of four linear accelerators were used for this work. All linear accelerators were manufactured by Varian (Varian Oncology Systems, Palo Alto, CA), and include a Clinac 6 EX, a Clinac 21 EX and a Clinac 2300 C/D accelerator housed at the Radiation Oncology department of the Montreal General Hospital, and a Clinac 21 EX at the Jewish General Hospital (JGH).

The 6 EX machine produces a 6 MV photon beam only, whereas the other machines produce 6 and 18 MV photon beams. In addition, all Varian dual photon energy linear accelerators produce various electron beams as well. All of the beams are calibrated as per the AAPM TG-51 calibration protocol[1] to deliver 1.0 cGy/MU at a depth of dose maximum in water, for a 10×10 cm^2 field at a source to surface distance of 100 cm. All of the accelerators are capable of delivering dose-rates in the range of 100 – 600 MU/minute, as well as dynamic beams. All accelerators are equipped for dynamic wedging, and the EX series accelerators are also equipped with the 120 leaf Millenium multi-leaf collimator (MLC) capable of IMRT beam delivery. The Clinac 2300 C/D has a 52 leaf MLC, and is also capable of IMRT beam delivery.

5.3. IMAGING SYSTEMS

The physics and a full description of the imaging systems can be found in Chapter 2. The following describes the implementation of the imaging systems for this thesis.

5.3.1. *a-Si EPID*

The amorphous silicon detector used for this study is a Varian aS500[2] (Varian Oncology Systems, Palo Alto, CA). The detector is mounted on a retractable arm connected to the gantry of the Clinac 21 EX accelerator at the MGH as illustrated in figure 5.1. The retractable arm can be moved vertically to vary the source to detector distance (SDD), or laterally and longitudinally to be placed under the radiation beam. The imager is contained within a light-tight enclosure with dimensions of 52 × 52 × 4 cm^3, with a detector area of 40 × 30 cm^2.

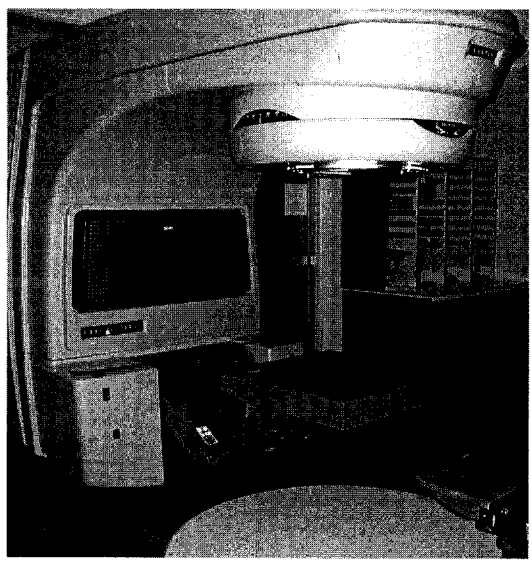

Fig. 5.1. Varian aS-500 EPID mounted on a retractable arm connected to the gantry of the linear accelerator.

5.3.2. *Matrix Ion chamber EPID*

A Varian PortalVision LC250[3] (Varian Oncology Systems, Palo Alto, CA) is a second generation matrix ion chamber EPID and is also called PortalVison Mk2 (Mark 2)[2]. It is installed on the Clinac 2300 C/D at the MGH. Like the aS500, PortalVision LC250 is also attached on a retractable arm connected to the gantry of the linear

accelerator. This system is also enclosed in a light tight box with dimensions of $52 \times 52 \times 4$ cm^3, and providing an imaging area of 32.5×32.5 cm^2.

5.3.3. *Fluoro based EPID*

The Fluoro based EPID studied in this work is an Eliav PortPro[4] (Eliav Medical Systems, Haifa, Israel) imaging system. PortPro is an independent, stand alone, and portable system which has a base dimension of 65×65 cm^2 for the image detection unit, and can be easily moved between treatment rooms as illustrated in figure 5.2. The unit in question is based at the JGH and was used on the Clinac 21 EX at that facility. The imaging area is 43×32 cm^2.

Fig. 5.2. Eliav PortPro fluoro based EPID. PortPro is an indepebdent, stand alone system[4].

5.3.4. *Computed radiography*

The Computed radiography unit employed for this thesis project was loaned as an experimental system for 1 week by Fuji (FujiFilm Medical Systems, Stamford, CT). The system is called SmartCR[5] and is equipped with image reader unit, and an assortment of imaging plates and cassettes. Imaging plates come in a standard size (35×43 cm^2) and in sizes such as 35×35 cm^2, 24×30 cm^2, and 18×24 cm^2. Like the PortPro system, SmartCR is also an independent, stand alone system, and for this work was used with the Clinac 21 EX accelerator at the JGH.

5.3.5. *Film*

The films for this study included the Ready-Pack film Kodak XV (Kodak Company, Rochester NY) and Ready-Pack extended dose range Kodak EDR (Kodak Company, Rochester NY). Kodak XV and Kodak EDR films employed have a dimension of 33×41 cm^2. In order to minimize potential experimental errors with film dosimetry, all irradiated films were taken from the same batch for any particular experiment. For any given experiment, the measurements were conducted on the same day and processed at the same time, the day after irradiation.

The films were processed using an AFP Imaging Mini-Med 90 film (AFP imaging Corp., Elmsford, NY) processor with a film processing time of approximately 90 seconds. One test film was developed before the start of processing in order to stabilize the processing conditions. Right after processing, the films were scanned and digitized using a Vidar VXR-12 film scanner (Vidar Systems Corporation, Herndon, VA) with a 0.017 cm/pixel, 8 bit resolution.

5.4. IMAGE QUALITY EVALUATION

5.4.1. *Subject contrast*

A contrast detail phantom was constructed using the specifications given by Munro *et al.*[6] and Falco[7] to obtain contrast detail curves for the imaging modalities investigated in this study. The phantom was constructed with an aluminum slab having the dimensions of $25 \times 25 \times 1.3$ cm^3 with a 10×10 array of holes with decreasing diameters in each row and decreasing depths in each column as seen in figure 5.3. The depths and diameters of the holes are listed in Table 5.1. Contrast detail curves were obtained for both 6 MV and 18 MV photon beams in which different hole depths can give primary subject contrast variation ranging from 0.37 % to 5.9 % for 6 MV photon spectrum.

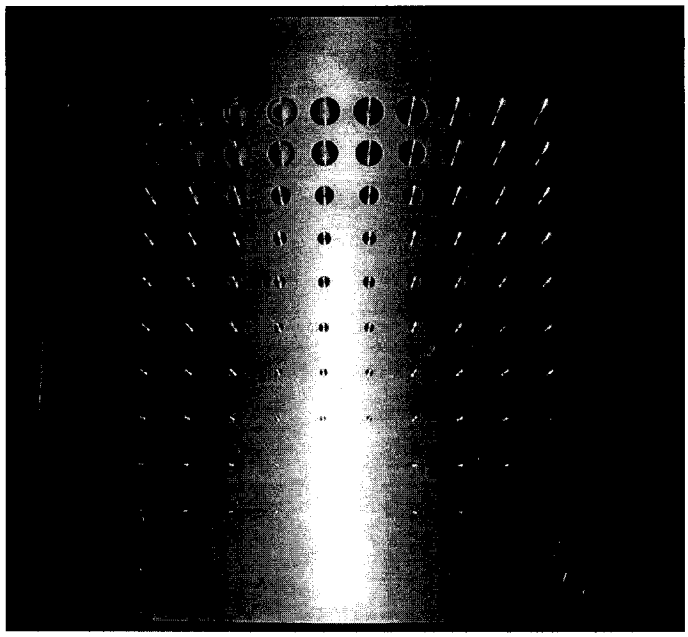

Fig. 5.3. Contrast-detail-phantom made from an aluminum slab having the dimensions of 25 × 25 × 1.3 cm^3 with a 10 × 10 array of holes with decreasing diameters in each column and decreasing depths in each row

Row	Hole diameter (mm)	Column	Hole depth (mm)
1	12.8	1	4.57
2	11.4	2	3.23
3	8.17	3	2.29
4	5.63	4	1.63
5	5.18	5	1.14
6	4.11	6	0.76
7	3.37	7	0.51
8	2.39	8	0.43
9	1.61	9	0.36
10	1.24	10	0.29

Table 5.1. List of the depths and the diameters of the holes forming the contrast detail phantom.

The contrast detail phantom was positioned at a source to phantom distance of 100 cm and imaged with all the imaging systems described in section 5.3 with a source to

detector distance of 120 cm. For all the detectors, three images were taken for each photon beam and three observers viewed each image in order to reduce the variations in the results. All the participants viewed the images on the display equipment that came with the respective EPID, where as the film images were viewed on a light box. The observers windowed the digital images and adjusted the room-lighting for the film to obtain what they considered to be the best image for a particular region of the phantom[7]. All the participants were asked to determine the smallest hole diameter that was observable for each column of hole depth. The average value of the three observers was used to plot the contrast detail curve.

Standard mode was used to obtain the images by amorphous silicon detector which received approximately 9.6 cGy of dose. Images from Matrix ion chamber and Fluoro based EPIDs were also obtained using the standard mode, each receiving approximately 13.4 cGy and 9.0 cGy of dose respectively. The CR plate received about 3.6 cGy during imaging and the Kodak XV (Kodak Company, Rochester NY) and Kodak EDR (Kodak Company, Rochester NY) received about 50.0 cGy and 160.0 cGy of dose respectively. During irradiation, films were placed in a film cassette with a 1.0 mm of copper plate at the front. Dose values were determined using a calibrated ion chamber on the central axis at the depth of dose maximum in solid water. The ion chamber was placed at the same source to surface distance as the detector source to surface distance.

5.4.2. Signal-to-noise ratio

Signal-noise-ratio (SNR) was investigated as a function of source to detector distance for both 6 MV and 18 MV photon beams. At each source-to-detector distance (SDD), two images were taken with a field size of 10 × 10 cm^2 and with fixed MUs. Images were acquired with all the imaging modalities mentioned in section 5.3. For EPIDs, all the images were taken with open beam without any build up placed on the detector. Both the Kodak XV (Kodak Company, Rochester NY) and Kodak EDR (Kodak Company, Rochester NY) films were irradiated using the film cassette (1.0 mm of copper plate at the front to generate high energy electrons). The CR images were obtained by irradiating the CR plate inserted in the CR cassette as described in section 5.3.4. For all the imaging modalities, the source to detector distance was varied between 80 cm and 170

cm during imaging. To simulate the imaging conditions in the clinic, all the images were taken in standard mode. To determine the SNR of the images, the mean value and the standard deviation of the middle 9 × 9 pixels were calculated. As shown in section 3.1.1.2 the SNR is the ratio of the mean signal to the standard deviation. All the images were analysed with Matlab software (MathWorks Inc., Natick, MA) which has the necessary tools to determine the mean and the standard deviation of the images.

5.4.3. Spatial resolution

The QC-3V quality assurance phantom (Masthead Imaging Corp, Nanaimo, B.C) developed by Shalev[8] was used to determine the spatial resolution of all the imaging modalities being investigated. A schematic diagram of this phantom is shown in figure 5.4. It consists of five sets of high-contrast rectangular bars with spatial frequencies of 0.1, 0.2, 0.25, 0.4, and 0.75 lp/mm respectively. The frame of the phantom is made of aluminum, and five test sections are made of lead and Delrin (Acetal) plastic (density: 1.42 g cm^{-3})[10]. The phantom is 15 mm thick and has 3 mm acrylic and 2 mm aluminum cover plates on the top and bottom, respectively.

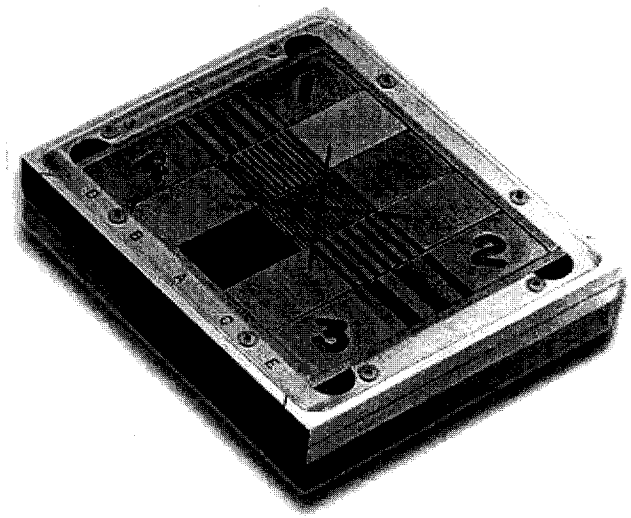

Fig. 5.4. Illustration of QC-3V phantom which contains five sets of high contrast rectangular bars used to determine spatial resolution of imaging systems.

The study was performed with phantom placed directly on top of the detector. This was done to minimize blurring due to the beam penumbra. This test is intended to monitor the performance of the detector and to be independent of the linac source size.

With the phantom located directly on the detector, images were taken with varying source to surface distances. The source to surface distance was varied between 110 cm and 160 cm and two images were obtained at each location. The phantom was rotated to 45° relative to the video scan lines to prevent aliasing in the images of the bar pattern.

The first measurements were done on the Fluoro based EPID. Four video frames were acquired for each image with about 2.0 cGy dose delivered to the phantom at SSD 100 cm. For the Liquid matrix EPID, only one frame was acquired per image since time needed to acquire one image is about 3.5 seconds resulting in 9.6 cGy of dose received by the phantom at SSD 100 cm. Four frames were averaged for the amorphous silicon detector for duration of 0.8 seconds (about 5.6 cGy to the phantom surface at SSD 100 cm). Films were inserted in the film cassettes during irradiation to simulate the clinical set-up procedure. During irradiation of Kodak XV film, the phantom received about 40 cGy where about 175 cGy of dose was subjected to the phantom surface for imaging of Kodak EDR films. It should be noted that higher dose than this is delivered to the phantom for each measurement, since image acquisition starts only after stabilization of the beam.

For the analysis of spatial resolution, all the images were imported into the Portal Imaging Processing System (PIPS) software (Masthead Imaging Corp, Nanaimo, B.C). After all the images have been imported, the position of the phantom is delineated automatically by the software searching for the outer edges of the phantom and identifying the corners. One set of images is needed for determining the spatial resolution at each particular location. The software determines the spatial resolution by the line pair frequency at which the Modulation transfer function falls to 0.50.

5.4.4. Modulation transfer function

The same QC-3V phantom was used to determine the modulator transfer function (MTF) of all the imaging modalities. The same set-up was used to acquire the images as was used to acquire images to determine the spatial resolution. In this case, only one source to detector distance of 120 cm was used. The images were again imported into the PIPS software program to determine the MTFs of each system.

The program determined the MTF as follows. A region of interest is placed over each set of bars of the phantom image and the MTF is determined by method proposed by Droege[10] and Barnes[11]. The MTF of an imaging system is given by Barnes[11]:

$$MTF(f) = \frac{\Delta E(f)}{\Delta E(f_1)}, \tag{5.1}$$

where $\Delta E(f_1)$ is the output modulation for the lowest frequency and $\Delta E(f)$ is the output modulation of the imaging system. For a sinusoidal output, $(\Delta E)^2$ is proportional to the variance $(M)^2$ within an ROI containing the bar pattern, and the above relation can be rewritten as:

$$MTF(f) = \frac{M(f)}{M(f)_1}, \tag{5.2}$$

and the function $M(f)$ is:

$$M^2(f) = \sigma_m^2(f) - \sigma^2(f). \tag{5.3}$$

Here $\sigma_m^2(f)$ and $\sigma^2(f)$ are the measured total variance and the variance due to random noise, respectively. The total variance $\sigma_m^2(f)$ is obtained by measuring the variance of the pixels in the ROI corresponding to frequency f. In order to measure the random noise in an image, a pair of similar images is subtracted, and standard deviation is obtained from the difference, thus avoiding contributions from noise. Therefore by measuring the standard deviation of pixels in the ROI for each bar pattern for pair of images, the MTFs for each spatial frequency can be calculated using equations 5.3.

5.4.5. *Gantry angle dependence*

This experiment was designed to determine the response of the imaging modalities at various gantry angles. Only the EPID systems fixed to the gantry were considered for this study since the film and the CR can be oriented in any position at a given gantry angle during imaging. For all the images, the detectors were positioned at a source to detector distance of 120 cm with a field size of 10 × 10 cm^2 at the isocenter. Two images were taken for each gantry angle and the average pixel value for 9 × 9 pixel section was determined for each image. The area represented by this pixel array is about 1 × 1 cm^2 at

the detector surface. This array size was chosen to minimize statistical fluctuations in pixel response while maintaining adequate spatial resolution.

For a-Si and Matrix ion chamber EPIDs, images were taken for gantry angles between 0° and 360° with 45° intervals. Since PortPro (Fluoro EPID) is not directly attached to the gantry of the linac, only gantry angles between 0° and 180° have to be considered for this particular EPID. Film systems are independent of gantry motion.

5.5. PORTAL DOSIMETRIC EVALUATION

5.5.1. Characteristic curves

The relationship between the pixel value and dose was investigated for the EPID systems used in the study. Since the systems are sensitive to different photon energies, repetition rates, and acquisition modes, the input/output characteristics of the imaging devices were investigated for all the different combinations of accelerator settings and EPID's acquisition modes. All the images were obtained without any buildup materials placed on the detectors. The components inside the detector provided buildup of about 1 cm of solid water equivalent thickness. Prior to the measurement of characteristic curves, EPIDs were calibrated for all the acquisition modes at an SDD of 140 cm with gantry oriented at 0°. These acquisition modes are generated using photon energies of 6 and 18 MV, repetition rate settings of 100, 200, 300, and 400 MU/min, and different sampling modes of the EPID systems.

For the measurement of characteristic curves, the EPIDs were positioned at a distance of 120 cm from the source. Two images were taken for each acquisition mode with increasing lead slabs. Irradiating the imager with various thicknesses of lead slabs (up to a combined thickness of 35 mm) will ensure that images are produced with photon beams of various intensities. Lead slabs were placed on a Lucite tray held by a holder near the head of the gantry to ensure that electrons produced by the interactions of photon with lead would not reach the detector surface and contribute to the image signal. All the images were taken with field size of 10×10 cm^2. After obtaining all the images, a Farmer type ion chamber was positioned at the same distance as the EPID and solid water was used to provide 1.5 and 3.5 cm build up at 6 and 18 MV, respectively. Ion chamber

measurements were acquired with 50 MU exposures with increasing lead thickness to determine the absolute dose on the central axis. The mean pixel values of the images were calculated by selecting a 9 × 9 matrix of pixels centered on the beam central axis. This reduced the effects of pixel by pixel fluctuation on the measurement curve.

The relationship between the dose and optical density was investigated for both Kodak XV and Kodak EDR films. Films were exposed perpendicular to the beam central axis with field size of 10 × 10 cm^2. The films were sandwiched between slabs of solid water with 5 cm of solid water placed beneath the film to ensure adequate back scatter for these experiments. All films were irradiated in the perpendicular geometry with the radiation beam incident at right angles to the surface of the solid water phantom at a depth of dose maximum with an SSD of 100 cm. For Kodak EDR films, exposures were taken between 0 and 500 MUs with 6 and 18 MV photon beams at a depth of dose maximum. Kodak XV films were irradiated between 0 and 170 MUs. This corresponded roughly to a dose range of 0 to 510 cGy for Kodak ERD film and 0 to 175 cGy for Kodak XV film. The 0 MU film corresponded to a film from each type that was developed without being irradiated, to determine base fog optical density levels. To minimize potential experimental errors with film dosimetry, films were developed and scanned as explained in section 5.3.5. Optical density for each film was determined by a calibrated Sakura PDA-11 (Konishiroku Photo Ind. Co. Ltd, Tokyo, Japan) manual densitometer. To reduce the point to point variation in density measurements, optical densities were measured for several points on the film near the central axis of the beam.

5.5.2. Field size dependence

The influence of side scatter on the aS-500 EPID was investigated by performing dose measurements as a function of field size. The scattering properties were studied for 6 MV photon beam at an SSD of 100 cm with filed sizes ranging from 4 × 4 cm^2 to 20 × 20 cm^2. A total of two images were taken for each field size and the middle 9 × 9 pixels were averaged to obtain the mean pixel at the beam central axis. The mean pixel value was compared with the dose measured with an ion chamber positioned at the depth of dose maximum in the solid water phantom.

5.5.3. *Static field dosimetry*

In the first part of the thesis, image quality parameters were investigated for all three types of EPIDs to select the most appropriate imaging system to perform dosimetric studies. Amorphous silicon EPID was chosen because it has very low image acquisition time, high resistance to radiation, and the image quality parameters produced by this type of EPID were superior to Matrix ion chamber EPID and Fluoro based EPID. All the open field, static wedge, and dynamic wedge studies were conducted only with amorphous silicon EPID.

5.5.3.1. *Open and static wedge field measurements*

When acquiring static fields, the default image acquisition process is controlled by a trigger board incorporated into the imager. The trigger board of the imager activates the EPID as the accelerator begins delivering the radiation beam. The trigger board also halts the EPID as soon as the radiation is stopped. If the radiation is on for a long period of time, the imager halts after acquiring a total of four frames, each lasting about 300 milliseconds, to produce a single image that is to be displayed on the computer monitor.

In order to test the relative dosimetric capabilities of the flat-panel detector, a series of data frames were acquired for various field sizes for open field with 6 and 18 MV photon beams. Images were taken for field sizes 10×10 cm^2 and 20×20 cm^2 with the detector positioned at a distance of 100 cm from the source. Total of four frames were averaged for each image with detector receiving about 8.0 cGy of dose for the 10×10 cm^2 field size. Images were also acquired with 60° and 45° static wedges with field size of 10×10 cm^2 for both 6 and 18 MV photon beams. From these images, one dimensional profiles can be extracted in any direction at any position within the radiation field. Beam profiles along the centre of the field were extracted using Scion image software (Scion Corp., Ferderick, MA). For comparison with the flat-panel data, beam profiles along the center of the field were obtained with an ion chamber immersed in a water tank (Welhoffer, Nurnburg, Germany). The profile scans were performed in a continuous fashion across the field while the accelerator was delivering the radiation. Wedge profiles were also scanned using the water tank.

5.5.4. *Dynamic field dosimetry*

To perform dynamic field studies, the image acquisition process of the a-Si EPID has to be configured differently. In dynamic fields, the beam is continuously modulated during the entire course of the beam delivery. For a dynamic wedge field, for example, the beam pauses just before the moving jaw begins its motion to create the wedge effect. If the trigger board controls the image acquisition process, as in static field image acquisition mode, the pause in beam delivery will cause the imager to stop acquiring further frames; hence resulting in incomplete image acquisition. To overcome this problem, the image acquisition process had to be controlled manually by the operator. For the aS-500 EPID, the device can be controlled manually by changing the trigger and synchronization mode of the imager from "ACQ enable & ACQ Trigger" mode to "Immediate & Internal Frequency" mode.

With this setting, images were acquired with 60° and 45° enhanced dynamic wedges with a field size of 10 × 10 cm^2 for 6 MV photon beam and 60° enhanced dynamic wedge for 18 MV photon beam. Two images were acquired per wedge angle with detector positioned at SDD 100 cm. From the images, one dimensional beam profiles were extracted perpendicular to central axis at depth of dose maximum. Dynamic wedge profiles were also obtained from water tank measurements to be compared with the dynamic wedge profiles obtained from the aS-500 EPID.

To employ film as a standard to compare aS-500 EPID images, the film system was validated. Films experiments were performed with 60° and 45° dynamic wedges with a field size of 10 × 10 cm^2. The films were sandwiched between solid water blocks and irradiated with a 6 MV photon beam. Profiles acquired on a film were compared with ion chamber scans in a water tank to validate our choice of film as the standard.

5.6. INTENSITY MODULATED RADIATION THERAPY (IMRT) STUDY

At the MGH, IMRT is implemented on a Varian Clinac 21 EX linear accelerator equipped with a 120 leaf dynamic MLC system. The leaf sequencing file produced by the leaf sequencing algorithm is used by the MLC control computer to control the motion

of the MLC leaves during treatment delivery. Our goal was to develop a reliable and convenient procedure to ensure that the beam fluence patterns in the beam eye's view match those specified by an IMRT plan.

Four IMRT treatment studies containing 43, 51, 8, and 37 segments respectively were investigated using aS-500 EPID and Kodak XV film. Films were placed between solid water slabs at a depth of dose maximum and irradiated with 6 MV photon beam. After the films were scanned using the Vidar-12 scanner, the sensitometric dose calibration curve was applied to the scanned film images. This procedure resulted in dose calibrated digitized film images. Next, the images were obtained with aS-500 EPID positioned at a distance of 120 SDD with gantry at 0°. The imager was turned on 2 seconds before the linac delivered the beam and turned off 2 seconds after the beam stopped. The images were calibrated using the dose response curve of the aS-500 EPID.

Both aS-500 image and the film image were registered using PIPS software. Field edges were used as control points on each image for registration as illustrated in figure 5.5. The film image was used as a reference image to register the amorphous silicon image.

Both images were imported into Microcal Origin (Microcal Software Inc., Northampton, MA) software for normalization and relative iosodose comparison. Choosing the normalization point is very crucial when comparing isodose curves form two images. The normalization point has to be chosen on the same location for both images and it is generally selected in a high dose/low gradient region. Choosing a low dose gradient region for normalization will ensure that a small spatial misalignment of the normalization point on both images will not cause a large spatial discrepancy in overlaid isodose curves. After normalization, relative isodose curves are plotted for both images and compared.

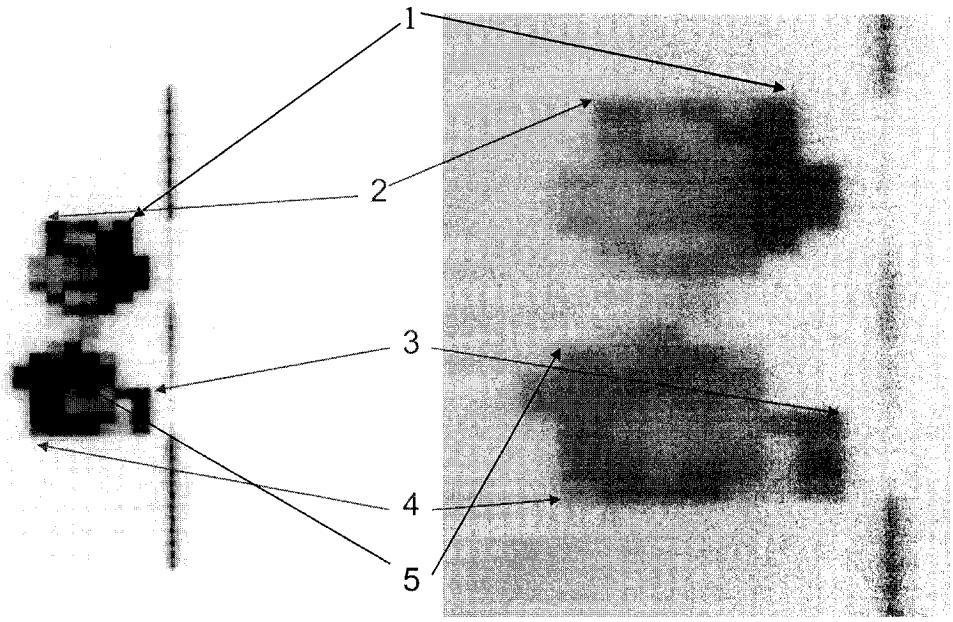

Fig. 5.5. Illustration of control point selection for registration of aS-500 EPID images with Kodak XV film images.

References

1. P. R. Almond, P. J. Biggs, B. M. Coursey, W. F. Hanson, M. S. Huq, R. Nath, and D. W. O. Rogers, "AAPM's TG-51 protocol for clinical reference dosimetry of high-energy photon and electron beams," Med. Phys. **26**, 1847-1870, (1999).
2. Varian Oncology Systems, "Portal Vision aS500 Rel. 6 System Manual (I.D. #PV6005RM_aS500) (2000).
3. Varian Oncology Systems, "Portal Vision LC250 Rel. 6 System Manual (I.D. #PV6004RM_LC250) (2000).
4. Eliav – Medical Imaging Syatems Web Site. Web Page: PortPro – Digital imaging for radiotherapy (http://www.eliav.com/portpro.htm).
5. Fuji Medical Imaging Web Site. Web Page: Computed Radiograpys SmartCR (http://www.fujimed.com/medical/cr_smartcr_specs.html).
6. P. Munro, J. A. Rawlinson, and A. Fenster, "Therapy imaging: A signal-to-noise analysis of a fluoroscopic imaging system for radiotherapy localization," Med. Phys. **17**, 763-772, (1990).
7. T. Falco, "Analysis of metal/film and novel metal/a-SE portal detectors," PhD thesis, McGill University, Montreal, (1999).
8. S. Shalev, R. Rajapakshe, K. Luchka, Thechniques for commisioning electronic portal imaging devices Proc. XII Int. Conf. on the use of computers in radiation therapy (Medical Physics Publishing, Madison, 1997).
9. R. Rajapakshe, K. Luchka, and S. Shalev, "A quality control test for electronic portal imaging devices," Med. Phys. **23**, 1237-1244, (1996).
10. R. T. Droege, "A practical method to routinely monitor resolution in digital images," Med. Phys. **10**, 337-343, (1983).
11. G. T. Barnes, "The use of bar pattern test objects in assessing the resolution of film/screen systems," in The Physics of Medical Imaging: Recording System Measurements and Techniques, edited by A. G. Haus (AIP, New York, NY, 1979).

Chapter 6

Results and Discussion I: Image Parameters

6.1. INTRODUCTION

This chapter discusses the results obtained from the image quality experiments. In the first part of the chapter, results for the detector parameters are given for all six imaging modalities investigated in this project. The detector parameters include acquisition time, saturation dose, minimum dose to obtain an image, and the pixel depth for the acquired images.

In the second part of the chapter, the image quality parameters are discussed for all the modalities. Parameters such as subject contrast, signal-to-noise-ratio, spatial resolution, modulation transfer function (*MTF*), and gantry angle dependence were compared amongst the imaging systems.

6.2. DETECTOR PARAMETERS

6.2.1. Acquisition time

A short acquisition time is essential to reduce blurring effects caused by patient motion. Also, the acquisition time of an imager may be very crucial for determining whether it can be employed as a dosimetric verification device. To accurately reconstruct the fluence intensity map of a treatment, the imager should be able to acquire an adequate number of frames in a short period of time. Table 6.1 lists the acquisition times for all the EPIDs employed in this thesis project. For the aS-500 amorphous silicon (a-Si) EPID (Varian Oncology Systems, Palo Alto, CA), the acquisition time to obtain one frame is 200 milliseconds. In a clinical setting, a total of six and ten frames are acquired for *standard* resolution and *high* resolution acquisition modes, resulting in a total acquisition time of 1.2 seconds and 2 seconds respectively. For dosimetric purposes, the acquisition time for an aS-500 EPID can be reduced to 200 milliseconds by obtaining one frame

instead of six or ten frames to form an image. The Portal Vision LC250 (Varian Oncology Systems, Palo Alto, CA) has two acquisition modes. As mentioned in section 2.3.2.3, in the *standard* acquisition mode, 256 HV lines are activated line by line sequentially, yielding the highest resolution but a long scanning time of 2.94 seconds. In the *fast* acquisition mode, two adjunct HV lines are activated simultaneously, yielding a shorter scanning time of 1.56 seconds. For the PortPro (Eliav Medical Systems, Haifa, Israel) EPID, the acquisition requires four frames, where each frame last for 135 milliseconds, are averaged to form an image.

As mentioned in section 1.3, treatment localization is very important to avoid inaccuracies in patient set-up. For verification of patient set up, a short acquisition time would result in fewer motion artifacts on the image as described in section 3.1.2. Therefore, it may be beneficial to have an imager with short acquisition time not only for dosimetric, but also for treatment localization purposes. PortPro has a very short acquisition time and a high number of frames may be acquired in "real time" to produce live images. For the Matrix ion chamber, the acquisition time is fairly high causing possible motion artifacts to be present on the acquired images. "Live" fluoro requires 25 frames per second (fps), therefore the PortPro EPID system is the most appropriate for this use.

	a-Si Portal Vision (aS-500)	Liquid Portal Vision (LC250)	Fluoro PortPro	Film - XV Kodak XV	Film - EDR2 Kodak EDR2	CR SmartCR
Acquisition Time *Standard Mode*	1.2 s	2.94 s	0.135 s	N/A	N/A	N/A
Acquisition Time *High Mode*	2 s	1.56 s				
Min dose to get an Image	1 cGy	3 cGy	3-4 cGy	5 cGy	25 cGy	1 cGy
Saturation Dose	~140 cGy	~140 cGy	~5 cGy	~200 cGy	~650 cGy	~20 cGy
Grey Scale	16 bit	16 bit	8 bit	Analogue	Analogue	16 bit

Table 6.1. List of detector parameters for the imaging modalities employed in this thesis project.

6.2.2. *Minimum dose to obtain an image*

Obviously, it is desirable to limit any extra dose the patient would receive from localization images. Table 6.1 lists the minimum dose required by the imagers to obtain a visible image. Treatment localization is usually performed with a low dose rate, so for an imager such as Portal Vision LC-250, which requires about 4-5 MUs (4 cGy) to acquire an image, motion artifacts caused by the patient could be an issue. Usually, an image is obtained by performing double exposures in order to visualize the treatment field in relation to the surrounding patient bony anatomy. Therefore, the Portal Vision LC-250 EPID requires a delivery of 8 to 10 MUs to the patient for treatment localization, which corresponds to roughly one tenth of the actual MUs given during a treatment fraction. This would result in a significant dose delivered to the patient if localization images are acquired frequently with the liquid matrix EPID during the entire course of treatment.

Even though the PortPro has a very short acquisition time, it still requires about 3 to 4 cGy of dose delivered to the imager to generate an image. This is due to the fact that the first few frames acquired by the PortPro are unstable and only stable frames are captured.

The aS-500 amorphous silicon EPID and the SmartCR computed radiography system only require about 1 MU to generate an image, thus making them the fastest imagers for treatment localization.

As mentioned in section 2.2, Kodak XV films are used for therapy verification. It is an ideal imaging modality for patient treatment verification. Kodak EDR film is used for dosimetric verification purposes only since it has a fairly long dose range, as evident from table 6.1. Essentially, patient localization is performed with Kodak X-OMAT TL or Portal Pack PPL films. These films typically require between 1 and 5 MUs to obtain suitable image localization.

6.2.3. *Saturation dose*

The full sensitometric curves of the imaging modalities are described in chapter 7. Saturation dose is not relevant for patient localization because we want to deliver minimum dose to patient and a wide dynamic range is not needed. But saturation dose of all the imaging modalities were determined to verify whether they could be employed for dosimetry verification. As shown in table 6.1, the PortPro EPID and the SmartCR (FujiFilm Medical Systems, Stamford, US) have a very low saturation dose. The saturation dose for the PortPro was determined by increasing the exposure time for a single frame until the image saturated. Once a saturated image was obtained, ion chamber measurements were taken with the same acquisition time to obtain the corresponding dose value. Using the optimum gain setting to produce the best quality image, the saturation dose was found to be around 5 cGy. The SmartCR has a saturation dose around 20 cGy, which makes it adequate for treatment verification.

The sensitometric response of Kodak EDR is seen to increase linearly with dose until approximately 350 cGy, beyond which the curve appears to deviate from linearity and eventually saturating at a dose value of 650 cGy. Kodak XV film saturates at a much lower dose, 200 cGy, in comparison to Kodak EDR film. As mentioned before, due to large dynamic dose range of EDR films, they can be used for IMRT dose verification.

Up to about 140 cGy can be delivered to the a-Si and Liquid Matrix EPIDs before the gain corrected images saturate. For these EPIDs, the final image is displayed by adding all the acquired frames and setting the optimum gain to obtain the best quality image. Above 140 cGy, the imager sets the same gain for all the images and thus the pixel value does not increase after the detector receives about 140 cGy, effectively dose saturating the detector.

6.3. IMAGE QUALITY PARAMETERS

6.3.1. Subject Contrast

Subject contrast is of interest in the implementation of patient localization and verification portal imaging. Figure 6.1(a) shows the contrast detail curves for all the imaging modalities when the contrast detail phantom is irradiated with 6 MV photon beam. The closer the contrast detail curve comes to the lower, left hand corner of the figure, the better the imaging system. The Portal Vision aS-500 amorphous silicon EPID performs especially well for low subject contrast holes with diameters between 2 mm and 4 mm.

Due to the limitation of the phantom which does not offer subject contrast less than 0.37 %, the minimum subject contrast needed to detect larger hole diameters (> 4 mm) cannot be determined for aS-500 EPID. This limitation of the phantom also limits the evaluation of the imaging modalities for object diameters less than 1.21 mm. If the phantom had smaller hole diameters for each subject contrast depth, more deviation between the curves could have been observed.

The curve for the Portal Vision LC-250 liquid matrix EPID starts to the left of the PortPro fluoro EPID offering better subject contrast for very small, high contrast objects. Both curves correspond between hole diameters 2 mm and 3.5 mm, implying that both imagers present the same subject contrast for small, high contrast objects. For hole diameters greater than 3.5 mm, the primary subject contrast for PortPro falls below the liquid matrix EPID curve, giving better subject contrast for large, low contrast objects. For very large objects with low subject contrast, liquid matrix EPID offers better subject contrast than PortPro EPID as evident by the liquid matrix falling below the PortPro after 6 mm on figure 6.1(a).

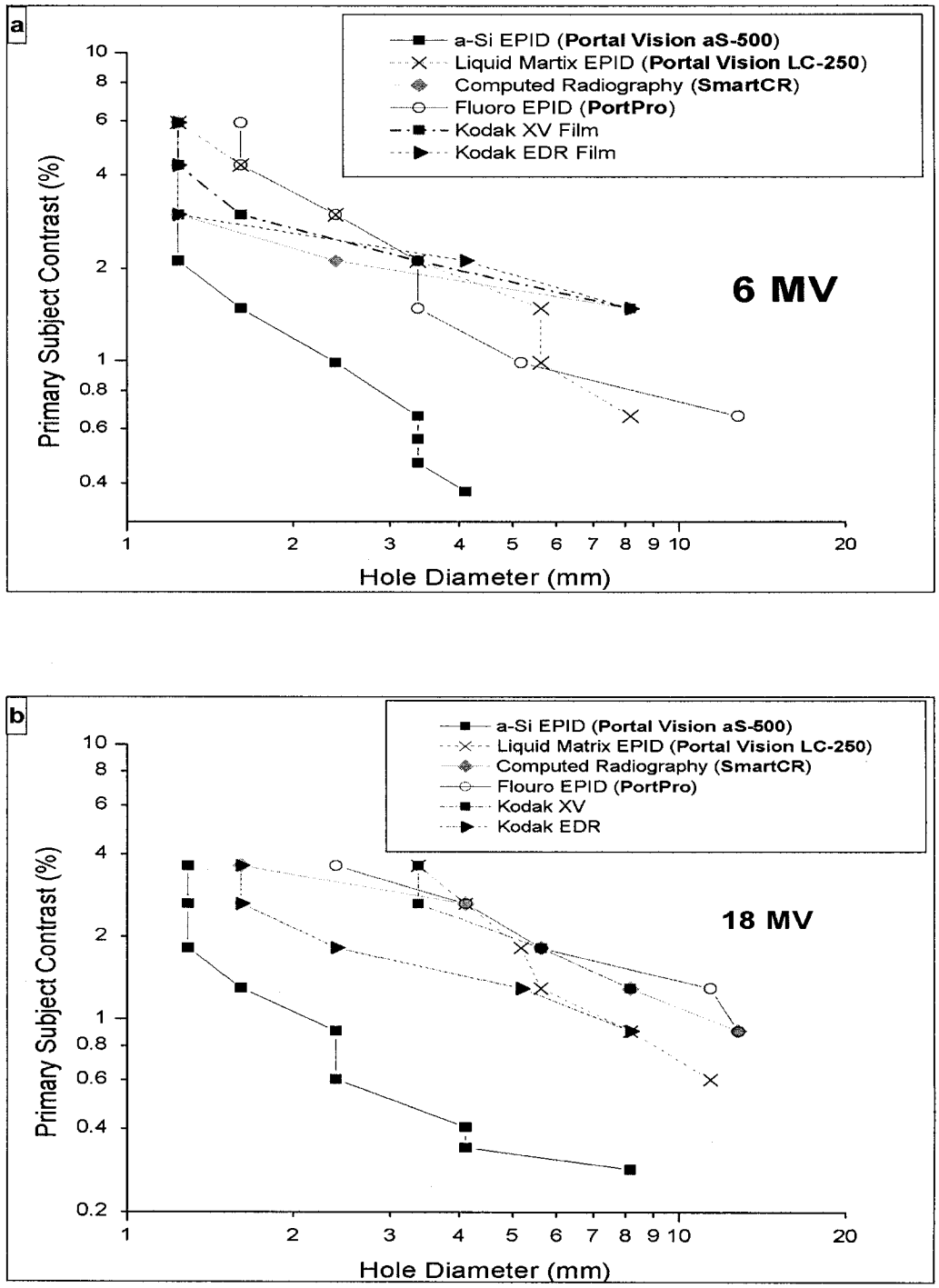

Fig. 6.1. Contrast-detail results produced for (a) 6 MV and (b) 18 MV photon beams with all the imaging modalities investigated in this thesis project: Portal Vision aS-500 amorphous silicon EPID, Portal Vision LC-250 liquid matrix EPID, PortPro fluoro based EPID, SmartCR computed radiography system, Kodak XV and Kodak EDR films. Primary subject contrast is related to hole depth. A detail description of the contrast detail phantom is given in section 5.4.1.

Results of Figure 6.1(a) illustrate that Kodak EDR film performs slightly better than Kodak XV for small, high contrast objects. The role is reversed at large, low contrast objects where Kodak XV film achieves slightly better results than Kodak EDR film.

The SmartCR computed radiography (CR) system gives better subject contrast than both film systems throughout the whole region of the phantom surface, but is more noticeable in the medium-contrast, medium-hole region. For small, high-contrast objects, both film systems and the CR produce better subject contrast than the liquid matrix and the fluoro based EPIDs whereas for large, low-contrast objects, both EPIDs generate better subject contrast.

Figure 6.1(b) shows the results obtained using an 18 MV photon beam for all the imaging systems. Once again the aS-500 produces higher subject contrast than the other systems. To fully characterize the aS-500, a phantom with larger range of hole diameters and depths is needed. Another system that should be noted is the Kodak EDR film, which after the aS-500 EPID provided the highest contrast detail than the other imaging modalities. For both aS-500 EPID and Kodak EDR film, fewer holes in the contrast-detail phantom are visualized for 18 MV than for 6 MV. However, the curves for the 6 and 18 MV irradiations are almost identical indicating that both systems perform equally well.

Portal Vision LC-250 liquid matrix EPID matches the image quality of Kodak EDR film at the large, low contrast region whereas at the small, high contrast region the liquid matrix EPID equals the performance of the other three imaging modalities (Kodak XV film, Fluoro EPID, and CR system).

6.3.2. Signal-to-noise ratio

A simple, but effective method was used to measure the signal-to-noise-ratio (*SNR*) for the imaging modalities employed in this study[1]. The *SNR* was determined by dividing the average pixel value of the middle 9 × 9 pixels of a flat field image by the standard deviation of these values. The standard deviation is given by Eq. (6.1) as:

$$SD = \sqrt{\frac{\Sigma\left(\bar{x} - x_i\right)^2}{\left(N-1\right)^2}}, \tag{6.1}$$

where N is the number of pixels averaged, $\bar{x}$ is the average value of the middle 9 × 9 pixels. The *SNR* measurements were performed for various Source to Detector Distances (*SDD*s) to study the behaviour of the *SNR* with radiation intensity.

Figure 6.2(a) shows the *SNR* as a function of *SDD* for the imaging devices for 6 MV photon beam. It is important to note that all the points satisfy Rose's criteria for visibility (*SNR* > 5). The portal Vision aS-500 amorphous silicon EPID provided higher *SNR* values when compared to other imaging modalities. The *SNR* values for aS-500 decrease slightly with increasing *SDD*. As the detector is brought closer to the source, photon exposure increases per unit area on the detector surface, resulting in increased signal detection, leading to higher *SNR*s. As mentioned in section 2.3.3, the flat panel light sensor of aS-500 is directly attached to the scintillator, which reduces lateral light migration and improves the efficiency of the signal detected. Superior light detection efficiency and the absence of light migration in aS500 will result in a higher *SNR* than other systems whose scintillator is not adjacent to the detector (i.e. The PortPro EPID).

As mentioned in section 2.3.1.1, the PortPro EPID suffers form a phenomenon called glare which can comprise more than 25% of the total measured signal. This spurious signal could be attributed to the low *SNR* values seen in figure 6.2(a). Moreover, the CCD camera of the PortPro is located at a considerable distance from the x-ray detector, causing light spreading. Poor detection of the light signal further decreases the *SNR* of the PortPro EPID.

The Portal Vision LC-250 Matrix Ion chamber EPID shows high *SNR* values that decrease linearly with increasing *SDD*. This result for the Matrix ion chamber follows the general trend reported by van Herk[2]. Similar to the aS-500 EPID, the movement of the detector closer to the source results in increased signal detection. Increased signal detection in will lead to higher *SNR* at small *SDD*s. The *SNR* of the liquid matrix EPID is also affected by the lateral migration of electron in the liquid. This lateral migration is significant since the electrons can move freely in the dense liquid medium.

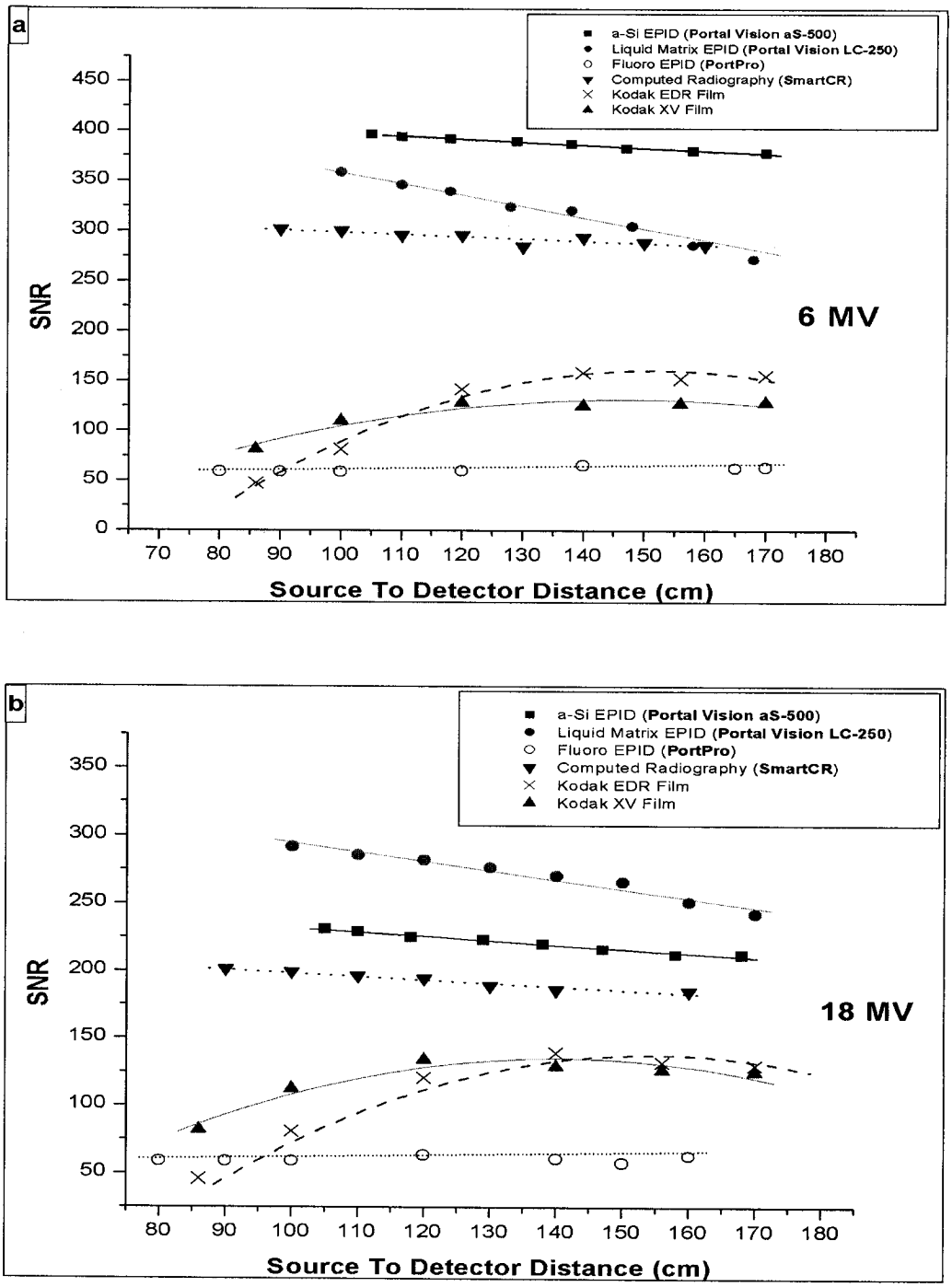

Fig. 6.2. SNR values as a function of Source to Detector Distances between 80 cm and 160 cm for (a) 6 MV and (b) 18 MV photon beams measured for all the imaging modalities employed in this project.

The *SNR* values for Kodak XV film and Kodak EDR film increase up to an *SDD* of 120 cm before approaching an almost constant value until an *SDD* of 160 cm. One has to note the fact that the *SNR* for the films also include the *SNR* of the film digitizer (Vidar Scanner) as well. In order to study the *SNR* properties of the scanner, a step-wedge film with known optical density values was digitized by the scanner. A 15 × 15 pixel area was analyzed to determine the *SNR* on each step wedge level. Figure 6.3 shows a plot of *SNR* as a function of given optical density values for the step-wedge film. The *SNR* increases to about an optical density value of 1.15 before decreasing rapidly.

One can conclude that as the film gets darker, the *SNR* increases, but when the film gets too dark, the *SNR* decreases rapidly. For very dark films, most of the light photons from the digitizer fail to transmit through the film and the insufficient detection of light photons leads to accumulation of noise. Increase in noise leads to lower *SNR* as shown in figure 6.3 after an optical density value of 1.15. The irradiated Kodak XV, and Kodak EDR films contained optical density values between 0.7 (*SDD* 170 cm) and 2.02 (*SDD* 80 cm). Films irradiated at small source to detector distances (*SDD* 80 cm to *SDD* 120 cm) were very dark with high optical density values. At these distances, the reduction in *SNR* is caused by the digitizer. As the *SDD* increases, the *SNR* also increases due to more light photons passing through the film. But for radiotherapy, the Source to Detector Distance range that is used varies between 120 cm and 160 cm since the patient is usually placed at a distance of 100 cm from the source with the detector positioned underneath the treatment couch. The film systems provide a uniform signal-to-noise-ratio within this *SDD* range as shown by Fig. 6.2(a). The *SNR* of the film digitizer heavily contributes to the total *SNR* of the film systems resulting in small total *SNR* values, especially for higher doses.

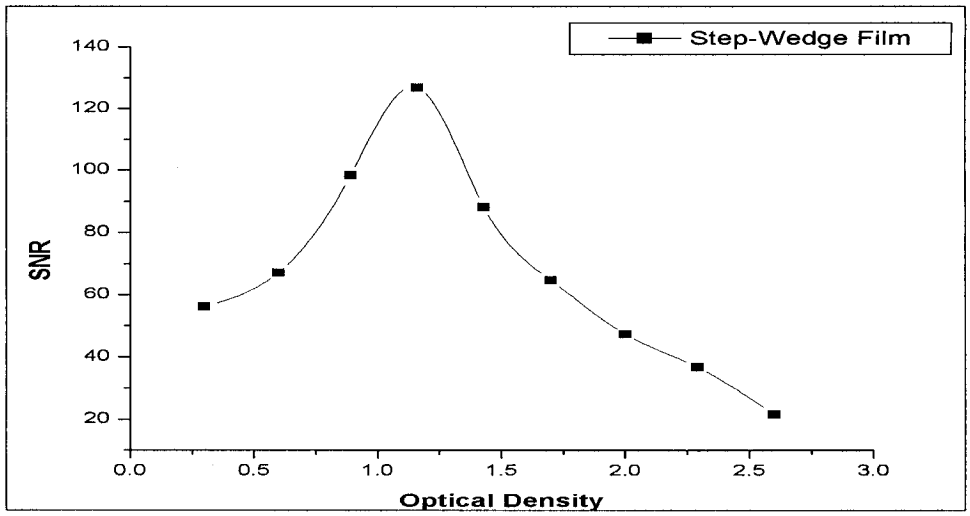

Fig. 6.3. Illustration of SNR values obtained for the Vidar-12 scanner using a step-wedge film. The middle 9× 9 pixel of each step-wedge region was analysed to determine the SNR. Optical density values were given by the manufacturer of the step-wedge film.

The *SNR* values for the SmartCr are significantly higher than for both the Kodak XV film and the Kodak EDR film with the values decreasing slightly with *SDD*. The same reasoning used for the aS-500 EPID and the matrix ion chamber EPID to explain the decrease of *SNR* with increase in the *SDD*s can be used to describe the *SNR* trend for the SmartCR system. Additionally, in contrast to the cassettes employed for films, the CR cassette has a thin sheet of lead behind the CR imaging plate to absorb the back scattered electrons. Scattered electrons will contribute to the noise in the image, so the reduction of scatter improves the *SNR* as demonstrated by the SmartCR system.

Figure 6.2(b) shows the *SNR* values obtained with an 18 MV photon beam. The *SNR* values for all the imaging modalities follow the same trend obtained with a 6 MV photon beam. The *SNR* values for the aS-500 EPID, the LC-250 EPID, and the SmartCR are lower at 18 MV due to reduced detective quantum efficiency (*DQE*). Higher energy photons have a lower probability of interaction so the *DQE* decreases at higher energies (refer to section 3.2.4). Reduced detection in signal causes lower *SNR*s for the same imaging system as seen from figure 6.2. For the PortPro EPID, the *SNR* values obtained at 18 MV photon beam remain the same as the *SNR* values obtained at 6 MV beam. As mentioned above, the glare, which accounts for about 25 % of the total measured signal, could considerably reduce the *SNR* of PortPro. The effect of reduction in *DQE* at 18 MV

is overshadowed by the glare which is present for both energies. Thus the *SNR* values observed at 6 MV are similar to the *SNR* values observed at 18 MV for PortPro EPID. However the opposite scenario occurs for aS-500 EPID. The flat panel light sensor for the aS-500 is directly attached to the x-ray detector, so the effect of *DQE* becomes the primary cause for reduction in the *SNR* at the beam energy of 18 MV. This could explain the reduction in *SNR* for aS-500 EPID when irradiated with 18 MV photon beam.

6.3.3. Spatial Resolution

Spatial resolution is a measure of how the image signal is blurred by the imaging systems. The spatial resolution of imaging systems depends on factors that are common to all the imaging modalities as well as factors that are device specific. Measurements were performed with the QC-3 phantom placed directly on top of the detector, and the source to phantom distance was varied. This test is intended to monitor the performance of the detector and to be independent of the linac source size. Figure 6.4(a) illustrates the spatial resolution obtained for all the imaging modalities as a function of the Source to Detector Distance with a 6 MV photon beam.

As evident from figure 6.4(a), the a-Si EPID has higher spatial resolution (0.38 lp/mm to 0.42 lp/mm) than the other systems over the entire range of the source to phantom distances. In this type of EPID, degradation of spatial resolution could be caused by the lateral migration of high energy electrons and the diffusion of light within the copper plate/phosphor screen or by the x-ray scatter and bremsstrahlung generated within the copper plate. But studies have shown that the primary reason for degradation of spatial resolution for aS-500 EPID is the actual pixel size of the flat panel light sensor [3-5].

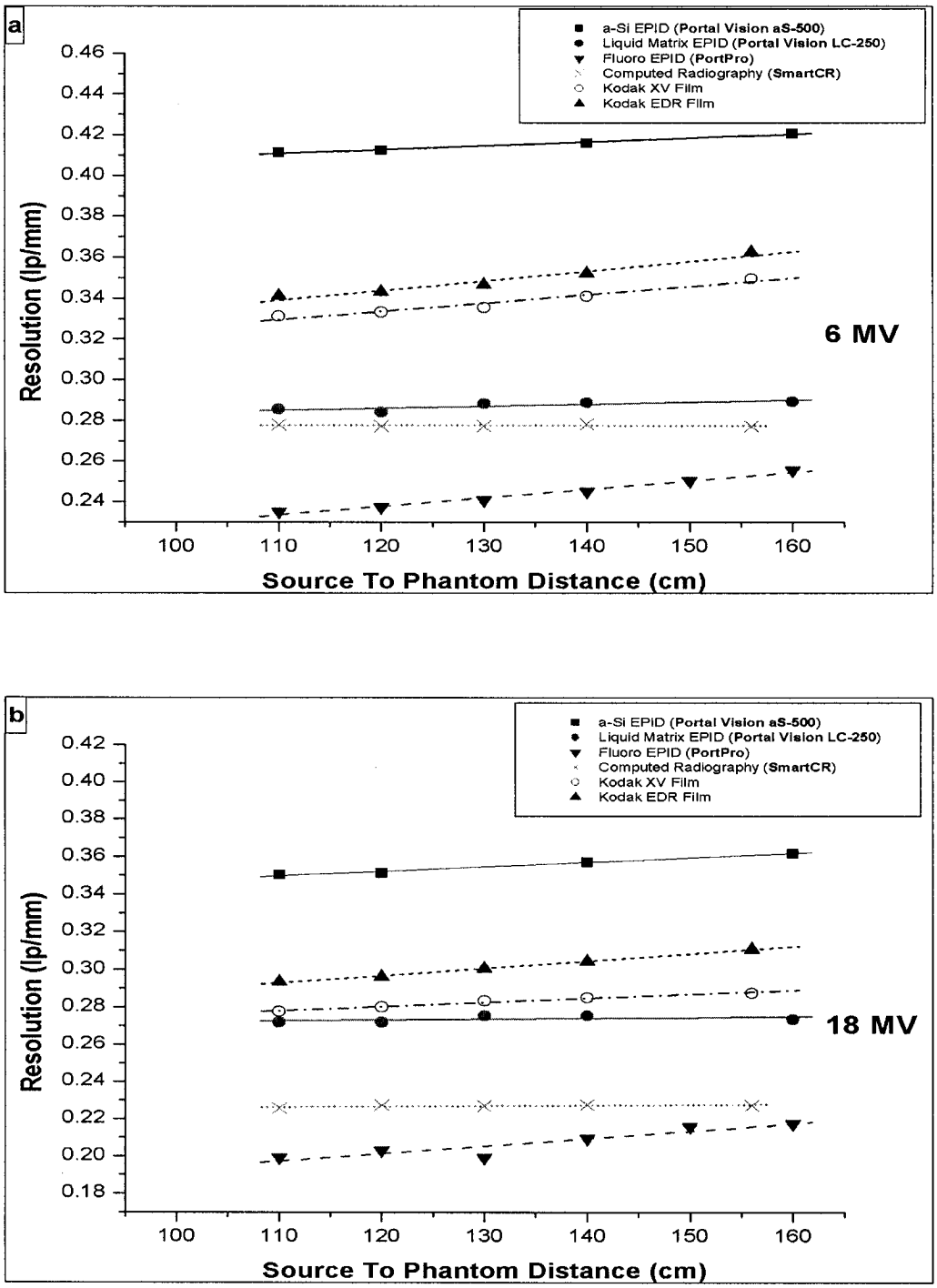

Fig. 6.4. Illustration of spatial resolution as a function of source to phantom distance for all the imaging modalities for (a) 6 MV and (b) 18 MV photon beams.

Since the flat panel light sensor is directly attached to the x-ray detector, light and electron migration does not influence spatial resolution considerably. The pixel dimension of the aS-500 EPID is 0.78×0.78 mm^2.

The Matrix ion chamber EPID has considerably lower spatial resolution (0.29 lp/mm to 0.30 lp/mm) than the aSi EPID. Reduction in spatial resolution can occur due to lateral electron migration in the ionization fluid. Since liquids have lower density than solids, the lateral migration of electrons occurs more freely in the ionization liquid of the matrix ion chamber than in the solid phosphor screen of the aSi EPID.

The electrode separation for the LC-250 matrix ion chamber EPID is 0.8 mm, which is a considerable distance for electron migration to occur. A study by van Herk *et al.* showed that pixel size of the detector is also a primary factor determining the spatial resolution[6]. Pixel dimension of the LC-250 is 1.27×1.27 mm^2, which is larger than the pixel dimension of the aS-500 EPID, which results in lower spatial resolution.

The comparison of the EPID systems shows that Fluoro EPID has the lowest spatial resolution (0.22 lp/mm – 0.26 lp/mm). Like the aSi EPID, the PortPro fluoro EPID utilizes the copper plate and the phosphor screen to generate light photons, so spatial resolution is affected by the lateral migration of the electrons and the light photons in the metal plate/phosphor screen. But the primary cause for reduction in spatial resolution in PortPro is the optical photon scatter (or glare) in the camera. As mentioned before, glare could be as much as 25% of the total signal resulting in very noisy images. This added noise would degrade the spatial resolution of the PortPro EPID considerably as shown in figure 6.4(a).

Both film systems (Kodak XV and Kodak EDR) exhibit similar spatial resolution with Kodak EDR showing slightly better results over the entire range of source to phantom distances. Spatial resolution of the film systems incorporate all the processes that are involved with developing and digitizing the films. Film's spatial resolution is mostly determined by the spatial resolution given by the film digitizer, which is 0.17 mm/pixel. Moreover, films were irradiated with the ready-pack envelopes inserted the film cassette as described in section 5.3.5. Even though the films were in direct contact with the copper plate, electron migration could still occur in the air gap between the ready pack envelop and the film emulsion surface, causing a reduction in spatial

resolution. Electrons can also spread while passing through film base. Even though the film base is quit thin, the low density of the film base (polyester) permits the electrons to spread easily. Since the film cassette also has a rear metal plate, the backscatter electrons also reduce the spatial resolution. Direct attachment of film with x-ray detector (copper plate) would cause resolution to be higher than fluoro and matrix ion chamber EPIDs but the process of digitizing, the presence of air gaps, and backscatter electrons cause the film systems to have a lower spatial resolution than the aSi EPID.

It should be noted that the spatial resolution for both Kodak XV and Kodak EDR film systems increases significantly if the experiment is performed with the naked eye instead of digitization. The spatial resolution of the Kodak XV and Kodak EDR films approaches to 5 lp/mm for the 6 MV photon beam and about 4.5 lp/mm for the 18 MV photon beam, which is higher than the spatial resolution offered by the aS-500 EPID. This is due to the fact that the film is a continuous, integrating, analogue dosimeter where the pixel size is determined by the finite size of the silver grains.

For the SmartCR, a laser beam scans the imaging plate to form an image by releasing the trapped electrons. The scan rate of the laser determines the number of pixels in each line. Each pixel of an imaging plate for the SmartCR has a dimension of 0.20×0.20 mm^2, and usually determines the maximum spatial resolution of the system. However, the physical limits imposed by the composition of the imaging plate and the size of the laser spot reduce the spatial resolution considerably. The diameter of the laser spot increases with depth in the phosphor layer, and is a major source of unsharpness. Spatial resolution can be increased by reducing the thickness of the imaging plate, but decreasing the thickness would lead to a lower *DQE* of the system. Typical CR plate has a thickness of 0.5 mm, which is considerably thicker than film. Increases in the laser focal spot size at depth and light migration causes the spatial resolution of the CR to be lower than other systems (0.23 lp/mm), except the PortPro EPID.

As one can see from figure 6.4, the spatial resolution for imaging modalities increases with the Source to Detector Distance. As the phantom and the detector are moved further away from the source, the projected penumbra width of the line pairs decreases due to the narrow beam geometry, which results in better spatial resolution. Figure 6.4(b) illustrates the spatial resolution obtained with an 18 MV photon beam for

all the imaging modalities. Spatial resolutions obtained for all imaging modalities with an 18 MV photon beam are lower than the resolution obtained with a 6 MV photon beam. A higher fraction of bremsstrahlung photons are produced at 18 MV than at 6 MV, which results in a spread of the signal due to scattered photon interactions. It is also important to recognize that there is reduced attenuation at higher megavoltage energies, which results in the reduced sharpness of the object and an apparent change in the projected object dimension. All these factors cause the resolution at 18 MV to be lower than that at 6 MV photon energy.

6.3.4. *Modulation Transfer Function (MTF)*

Spatial resolution of imaging systems in the form of signal transfer properties can be characterized by the detector's modulation transfer function (*MTF*)[7]. The *MTF* describes how well a system passes different spatial frequencies and it is calculated from the Fourier transform of the point spread function. Generally, for imaging, the point spread function and hence the *MTF* is greatly affected by the signal spread. The technique used to measure the *MTF* of the imaging devices is described in section 5.4.4.

The *MTF* curve for amorphous silicon is higher than the rest of the imagers for both 6 MV and 18 MV photon beams. The direct attachment of the flat panel light sensor to the x-ray detector results in minimal electron migration, which produces higher *MTF* values. As discussed previously, even though the XV film and the EDR film are directly adjacent to the copper plate of the film cassette, the low density of the film base permits the electrons to spread. Thus, the *MTF*s of the film system would be lower than the *MTF* of the a-Si EPID system as evident from figures 6.5(a) and (b).

The thick imaging plate of the Computed Radiography system permits considerable electron migration, causing the *MTF* curve to be even lower. Ionization liquid in the matrix ion chamber EPID permits considerable electron migration due to the low density of the ionization liquid, which results in a low *MTF* curve. The glare phenomenon, as explained previously, for Fluoro based EPID, causes the *MTF* curve of the Fluoro EPID to be much lower than other curves.

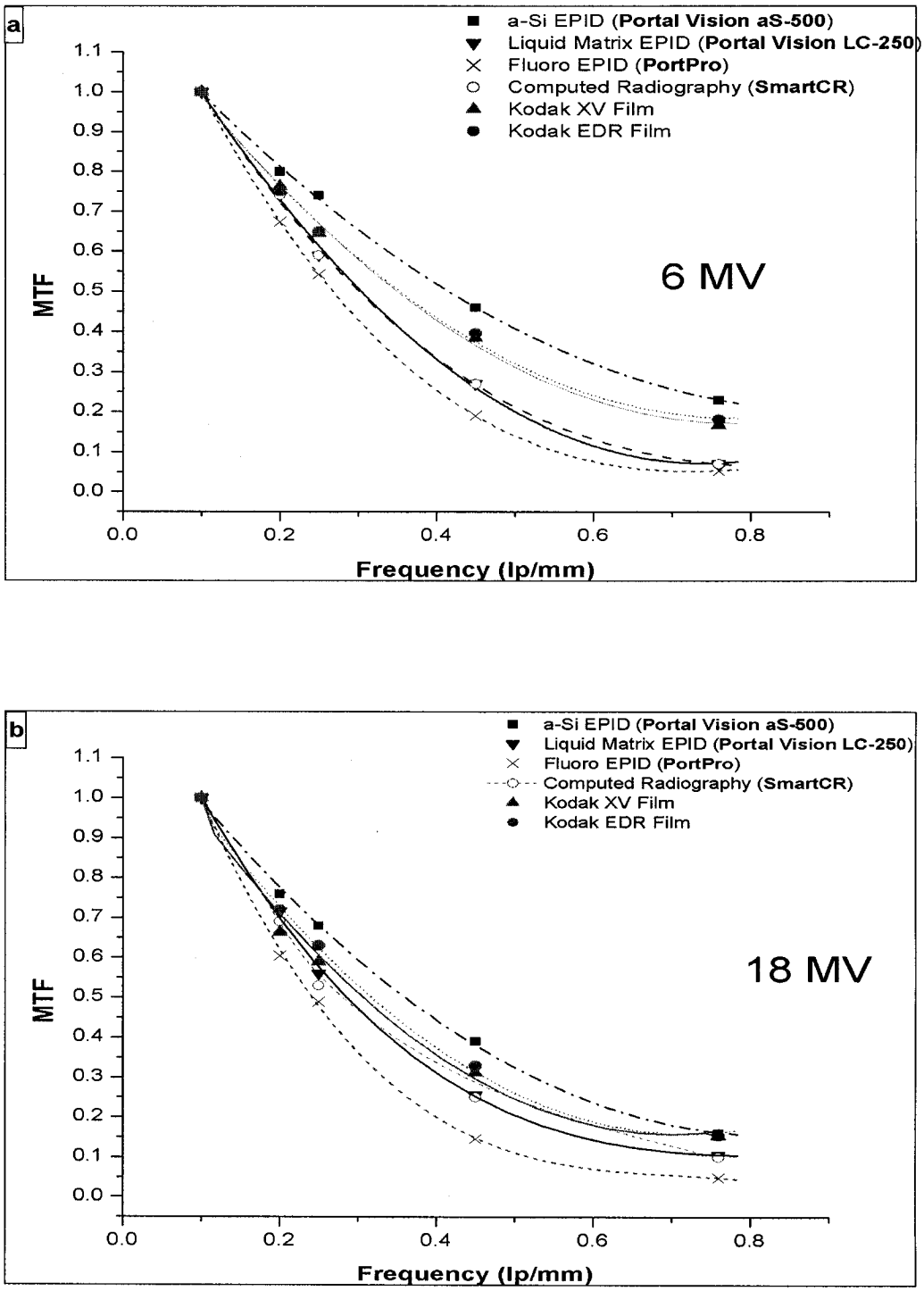

Fig. 6.5. Plotted are the MTFs for imaging modalities investigated in this project for (a) 6 MV and (b) 18 MV photon beam.

Figures 6.5(a) and 6.5(b) shows the *MTF* measurements obtained for different imaging modalities with 6 MV and 18 MV photon beams respectively. By carefully comparing both figures, one can see that for each imaging modality, the *MTF* for the 18 MV photon beam is slightly less than the *MTF* for a 6 MV photon beam. The electron spread within the detector influences the *MTF* considerably, and as the energy of the x-ray beam increases, the energy and hence the range of the electrons produced by the x-ray interactions increases, resulting in increased lateral spread in the detector. Thus, increasing x-ray energy leads to lower *MTF*'s as shown by the comparison of figures 6.5(a) and (b).

6.3.5. Gantry angle dependence

To effectively implement EPID systems for dosimetric verification of IMRT treatments and arc therapy, the response of the detector with gantry rotation should be investigated. Several studies have shown that the response is sinusoidal with gantry rotation[8-12]. Figure 6.6 shows the response of the detector as a function of gantry angle for all three types of EPID systems (a-Si EPID, Liquid matrix EPID, and Fluoro EPID) studied in this project.

The maximum deviation for all three EPIDs is only about 1%. The deviation could be caused by several factors such as the gantry sag, pressure of the iso-octane liquid in the liquid matrix EPID, and shift of the mirror and the CCD camera in the Fluoro based EPID. As for the a-Si EPID, the discrepancy may be due to the retractable arm sag. These results illustrate that acquiring images at various gantry angles does not influence the pixel values significantly, and is therefore not critical for patient localization.

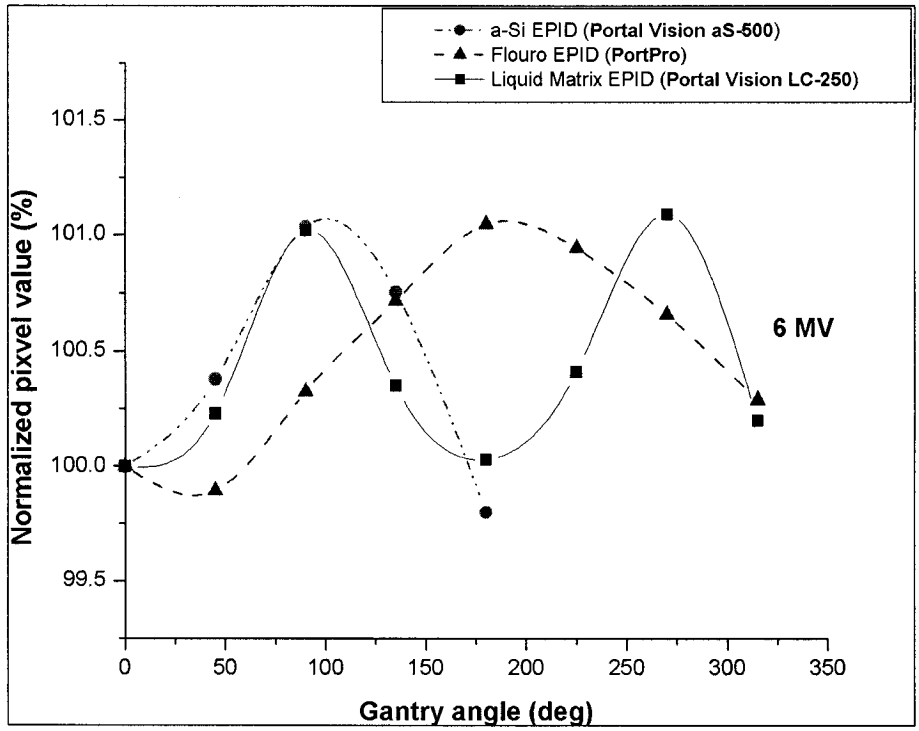

Fig. 6.6. Illustration of EPID response as a function of gantry angle. For each gantry angle, two images were taken and the middle 9× 9 pixels were averaged to determine the central signal response of the detectors. For a-Si EPID and Liquid Matrix EPID, images were acquired between the gantry angles of 0° and 315°. For Fluoro EPID, images were only obtained between 0° and 180° since Fluoro EPID is not physically attached to the gantry of the linear accelerator.

References

1. M. van Herk, J. Bijhold, B. Hoogervorst, and H. Meertens, "Sampling methods for a matrix ionization chamber system," Med. Phys. **19**, 409-418, (1992).
2. M. van Herk, "Physical aspects of a liquid-filled ionization chamber with pulsed polarizing voltage," Med. Phys. **18**, 692-702, (1991).
3. P. Munro, and D. C. Bouius, "X-ray quantum limited portal imaging using amorphous silicon flat-panel arrays," Med. Phys. **25**, 689-702, (1998).
4. A. L. Boyer, L. Antonuk, A. Fenster, M. Van Herk, H. Meertens, P. Munro, L. E. Reinstein, and J. Wong, "A review of electronic portal imaging devices (EPIDs)," Med. Phys. **19**, 1-16, (1992).
5. B. M. C. McCurdy, K. Luchka, and S. Pistorius, "Dosimetric investigation and portal dose image prediction using an amorphous silicon electronic portal imaging device," Med. Phys. **28**, 911-924, (2001).
6. M. van Herk, and H. Meertens, "A matrix ionization chamber imaging device for on-line patient setup verification during radiotherapy," Radiother. Oncol. **11**, 369-378, (1988).
7. K. Luchka, R. Rajapakshe, and S. Shalev, "Quality Asuurance of EPI Systems," Proc. 7th. Int. Workshop on Electronic Portal Imaging, Vancouver, 8-11, (2002).
8. K. Doi, G. Holje, L-N Loo, H-P Chan, J. M. Sandrik, R. J. Jennings, and R. F. Wagner, "*MTF*'s and Wiener spectra of radiographic screen-film systems," HHS Publ. No. 82-8187 (FDA), (1979).
9. D. M. Roback, and B. J. Gerbi, "Evaluation of electronic portal imaging device for missing tissue compensator design and verification," Med. Phys. **22**, 2029-2034, (1995).
10. M. Partridge, P. M. Evans, and M. A. Mosleh-Shirazi, "Linear accelerator output variations and their consequences for megavoltage imaging," Med. Phys. **25**, 1443-1452, (1998).
11. F. F. Yin, M. C. Schell, and P. Rubin, "Input/output characteristics of a matrix ion-chamber electronic portal imaging device," Med. Phys. **21**, 1447-1454, (1994).
12. H. Meertens, M. van Herk, J. Bijhold, and H. Bartelink, "First clinical experience with a newly developed electronic portal imaging device," Int. J. Radiat. Oncol. Biol. Phys. **18**, 1173-1181, (1990).

Chapter 7

Results and Disscussion II: Portal Dosimetry

7.1. INTRODUCTION

This chapter discusses the results obtained from the portal dosimetric experiments. In the first part of the chapter, the dose response characteristics of the EPID and the film systems are discussed. In the second part of the chapter, the aS-500 EPID is validated for IMRT dosimetry, and clinical examples are presented and compared with film quality assurance measurements.

7.2. CHARACTERISTIC CURVES

7.2.1. Amorphous silicon EPID (Portal Vision aS-500)

The dose response (pixel value as a function of dose per frame) was investigated for the aS-500 EPID for its various acquisition modes. The dose response was characterized in terms of beam energy, dose-rate, and sampling mode. In the *standard* sampling mode, six frames are averaged to form an image, whereas in the *high* sampling mode, ten frames are averaged to form an image. Figure 7.1 shows characteristic curves obtained for both sampling modes, 6 and 18 MV photon beams, at a repetition rate of 300 MU/min. From the graphs it is evident that the dose response is linear for both energies, and both acquisition modes. The dose per frame was measured with an ion chamber positioned at the same distance as the aSi EPID and solid water was used to provide 1.5 and 3.5 cm buildup at 6 and 18 MV respectively. Also evident from the graph is that acquisition mode has little effect on dose response. In fact, for each energy, the dose response is consistent for both acquisition modes to within 1 %.

Results from figure 7.1 also illustrate that the characteristic curves obtained for two different energies deviate slightly. The two curves spread further apart at higher doses

implying that the response of the imaging device to incident radiation is dependent on beam energy. This may be related to the insufficient build up material to provide charged particle equilibrium for the 18 MV photon beam. The material above the sensitive volume of the detector, including the components of the EPID itself, was equivalent to 1 cm water for 6 MV and 1.4 cm of water for 18 MV. Insufficient buildup material would cause the signal measured with 18 MV photon beam to be lower than the signal measured with 6 MV photon beam for the same number of monitor units and identical measuring conditions.

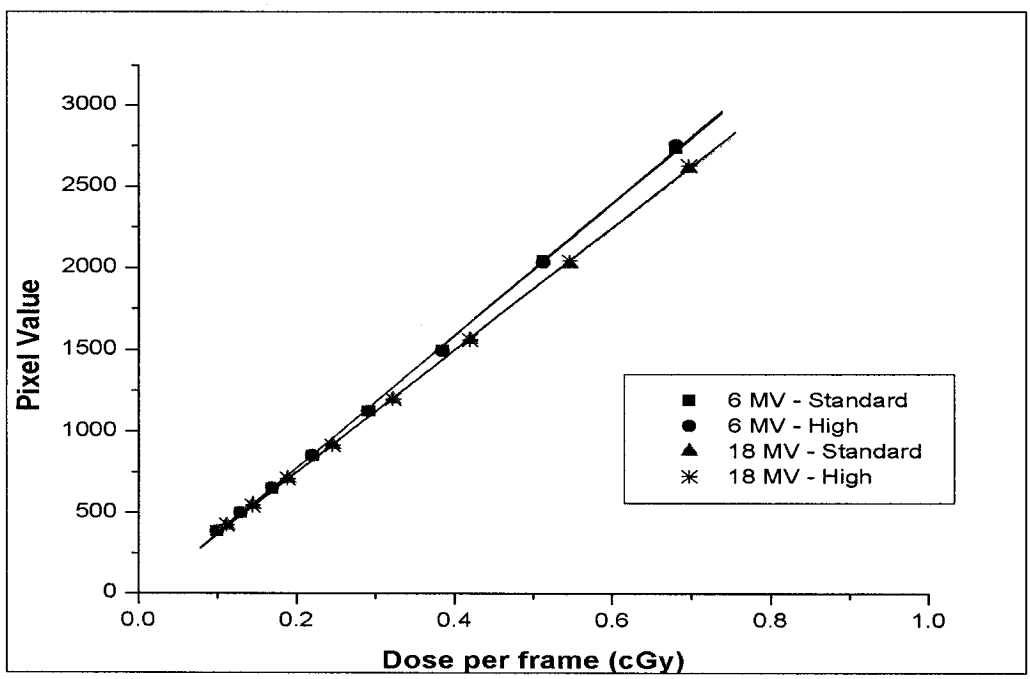

Fig. 7.1. The relationship between the pixel value and the dose per frame is shown for the aS-500 amorphous silicon EPID, obtained using four different acquisition modes (photon energies of 6 and 18 MV, standard and fast sampling modes, 300 MU/min) at the central axis.

The behavior of accelerator repetition-rate setting on the characteristic curve is shown in figure 7.2. Data are obtained using acquisition modes with 6 MV photon beam, a *standard* sampling mode, and repetition-rate settings of 100, 200, 300, and 400 MU/min. A linear fit was made through all the data points. The relationship between pixel value and dose for all the repetition-rates in figure 7.2 lie on the linear fit. This indicates that the electronic gain settings for all the repetition rates for a particular energy

are same. As one can see from figure 7.2, the dose per frame increases linearly with repetition rate.

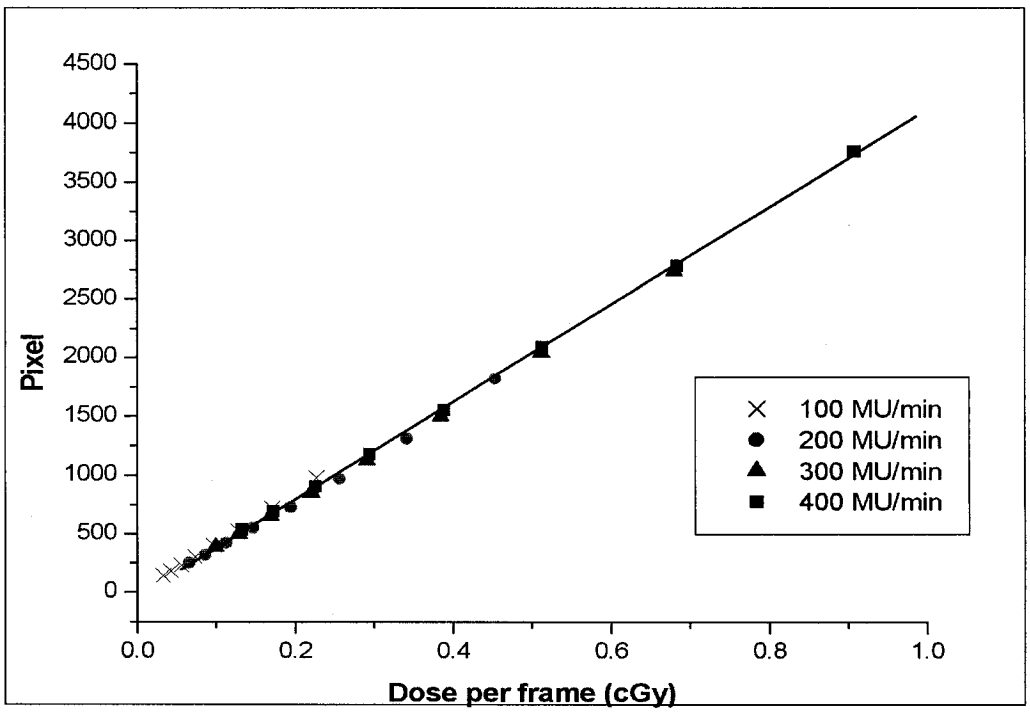

Fig. 7.2. Characteristic curves of a amorphous silicon EPID obtained using acquisition modes with a 6 MV photon beam, a standard sampling mode, and different repetition-rate settings. A linear fit was made through all the data points.

7.2.2. Liquid Matrix EPID (Portal Vision LC-250)

For Portal Vision aS-500 EPID, dose response was characterized as a pixel value as a function of dose rate at the detector. Shown in Figure 7.3 are sets of characteristic curves of the Portal Vision LC-250 (Varian Oncology Systems, Palo Alto, CA) matrix ion-chamber EPID at the central axis for 6 and 18 MV photons and both *standard* and *fast* sampling modes. All the data in figure 7.3 were measured using a repetition-rate setting of 300 MU/min and increasing thicknesses of lead to obtain different dose rates at the detector surface. Results indicate that the pixel value obtained from the imaging device is a square root function of the incident radiation intensity (dose rate) for both *standard* and

fast sampling modes. Smooth curves represent fits to the data using equation 4.1 in section 4.4.1.

The effect of acquisition mode on the characteristic curve is also illustrated in figure 7.3 for repetition-rate setting of 300 MU/min. It is clear that the detector response using the *standard* sampling mode is substantially different from that from the *fast* sampling mode. One reason for this difference is related to effective electronic gains, which are set differently for different acquisition modes. For the LC-250 EPID, the signal magnification (electronic gain) set in the *standard* sampling mode is about 2.5 times larger than that in the *fast* sampling mode. This results in 8 times greater signal averaged for the *standard* sampling mode than in the *fast* sampling mode, within the HV cycle time. In this specific type of detector, the larger the number of signals averaged, the higher the ion collection efficiency[1].

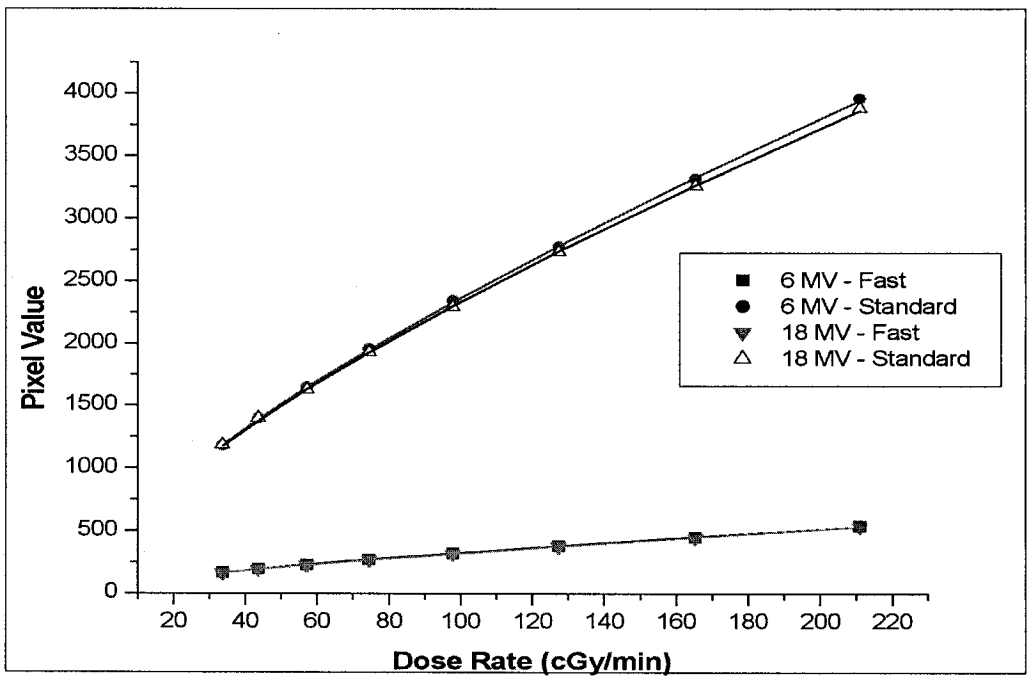

Fig. 7.3. Characteristic curves of a matrix ion-chamber (EPID) obtained using four different acquisition modes (photon energies of 6 and 18 MV, standard and fast sampling modes, 300 MU/min) at the central axis. Smooth curves are fits using equation 4.1. Dose rate is measured using a Famer type ion chamber placed at the same location as the detector.

Data in figure 7.3 also illustrate that the characteristic curves obtained with two different energies are similar for both *standard* and *fast* sampling modes. This implies that the response of the imaging device to the incident radiation intensity is comparable for different photon energy spectra. As with the aS-500 EPID, the slight difference between characteristic curves obtained using two different energies may be related to the thickness of build up material (about 1 mm steal sheet) provided by the LC-250 EPID. This thickness is insufficient for charge particle equilibrium for 18 MV photon beam. A study by Yin *et al.* verified this concept by placing a plastic sheet with 10 cm thickness on top of the liquid matrix detector to give sufficient build up material[2]. The resulting characteristic curve measured for 18 MV photon beam was then found to overlie that one measured for a 6 MV photon beam.

The effect of accelerator repetition-rate setting on the characteristic curve is illustrated in Fig. 7.4. Data are obtained with a 6 MV photon beam, a *standard* sampling mode, and three different repetition-rate settings. All data are fitted with the equation 4.2.

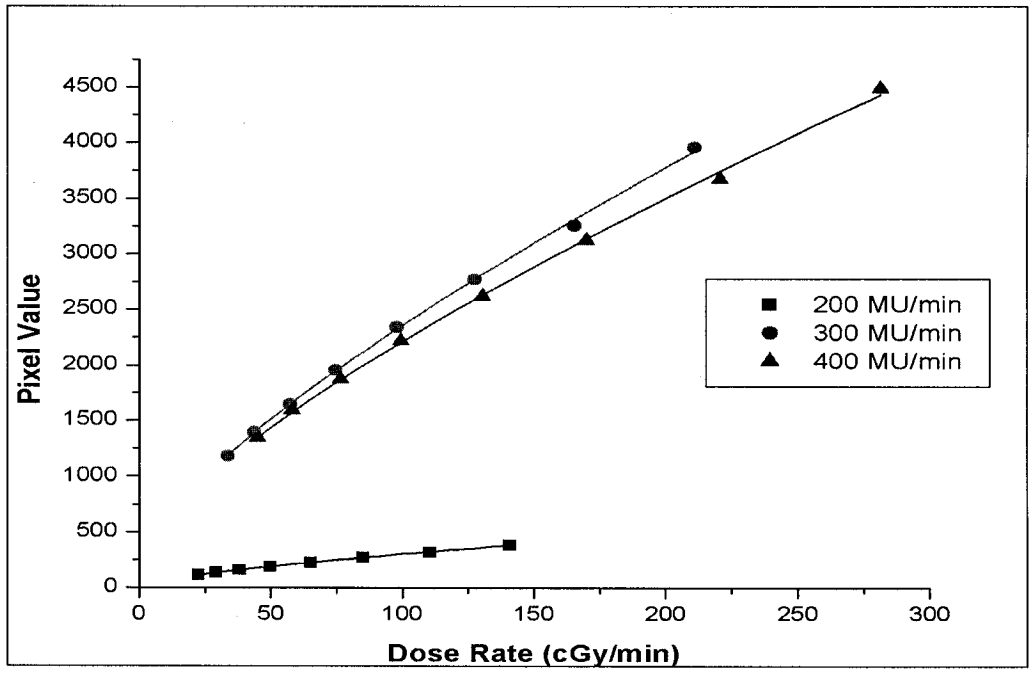

Fig. 7.4. Characteristic curves of a matrix ion-chamber EPID obtained using acquisition modes with a 6 MV photon beam, a standard sampling mode, and different repetition-rate settings. Smooth curves are fits using equation 4.1. Dose rate is measured using a Famer type ion chamber placed at the same location as the detector.

Results indicate that data obtained using different repetition-rate settings differ from one another; especially the data obtained using the repetition-rate setting of 200 MU/min. This implies that the response of the imaging device varies substantially with repetition-rate settings. These differences are related to the internal settings of effective electronic gains for different acquisition modes.

7.2.3. *Fluoro based EPID (PortPro)*

The dose response of the PortPro Fluoro based EPID was also investigated. The PortPro EPID only comprises of one sampling mode (*standard* mode) with an acquisition time of 135 ms per frame. All images were acquired after the live images on the screen became stable. Total of four frames were acquired and averaged to form the final image. Figure 7.5 illustrates that the characteristic curve obtained with 6 MV and 18 MV photon energies are similar, and both linear. Again, the lower response of the 18 MV photon beam is probably due to the lack of electrons resulting from insufficient build up material.

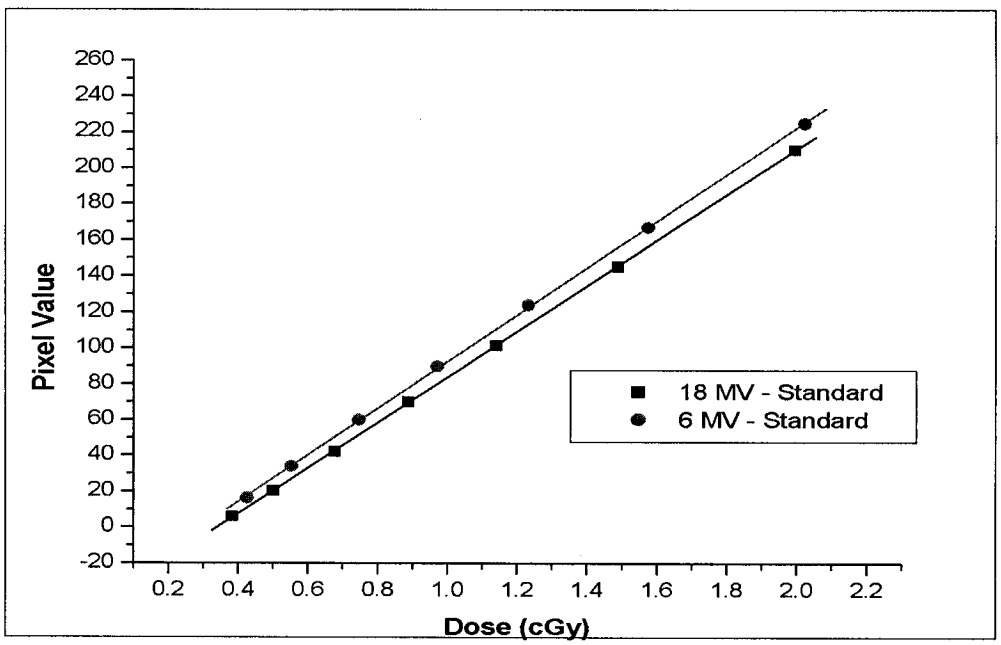

Fig. 7.5. Characteristic curves of the PortPro Fluoro Based (EPID) obtained for photon energies of 6 and 18 MV, standard sampling mode, 300 MU/min at the central axis. Dose is measured using a Famer type ion chamber placed at the same location as the detector.

The effect of accelerator repletion-rate setting on the dose response curve is illustrated in figure 7.6. The data points illustrated in this figure are obtained using acquisition modes with a 6 MV photon beam and four different repetition-rate settings. All data points, except the highest data point for the repetition-rate of 400 MU/min, coincide on the same linear fit implying that different repetition-rate settings of the accelerator provide same pixel value on the images.

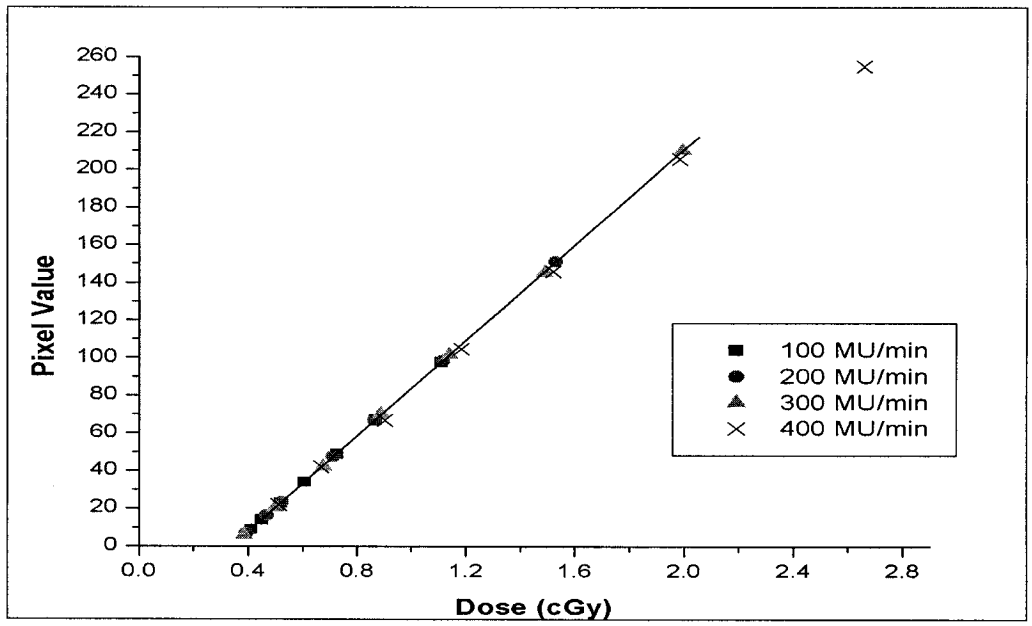

Fig. 7.6. Characteristic curves of a Fluoro Based EPID obtained for a 6 MV photon beam, and different repetition-rate settings.

The deviated data point in figure was only measurable with the 400 MU/min mode, due to the limited acquisition time used for the experiment (4 x 135 ms). The point is significant because it demonstrates the beginning of the signal saturation at higher doses.

7.2.4. *Film systems*

Net optical density as a function of dose was investigated for the Kodak XV and Kodak EDR film systems. Figure 7.7 illustrates the variation in optical density as a function of dose for both film systems. Included in this plot are the data for 6 MV and 18 MV photon beams for a 10 × 10 cm^2 field size at a depth of dose maximum (1.5 cm for 6 MV, and 3.5 cm for 18 MV) within the solid water phantom. The dose response of Kodak EDR film is seen to increase linearly with dose until approximately 350 cGy, beyond which the curves deviate from linearity, the gradient decreases and the film saturates at a dose level of 650 cGy. Kodak EDR film response is quite different from that of Kodak XV films, whose dose response curves are slightly concave downward in shape and saturate at a lower dose, about 200 cGy. It is also noted in figure 7.7 that Kodak EDR film shows an increased sensitivity with increase in energy at higher doses. This result is corroborated in table 7.4 where the optical density ratios for 18 MV to 6 MV beams, are presented for dose levels of 50 cGy and 150 cGy for Kodak XV and at 50 cGy, 150 cGy, and 350 cGy for Kodak EDR film.

From table 7.1, we can summarize that the Kodak XV films are energy independent between 6 MV and 18 MV photon energies to within 2 %. The Kodak EDR films show similar characteristics till 150 cGy, but start to show energy dependence for higher doses. The data presented in figure 7.7 and table 7.4 for Kodak XV and Kodak EDR films are in good agreement with those of Chetty *et al*[3].

Dose Level	XV film [OD(18 MV)/OD(6 MV)]	EDR film [OD(18 MV)/OD(6 MV)]
50 cGy	1.01	1.02
150 cGy	1.02	1.03
350 cGy	-	1.07

Table 7.1. Optical desity ratios, 18 MV versus 6 MV, for field size 10 × 10 cm^2 at dose levels Of 50, 150, and 350 cGy for Kodak XV and Kodak EDR films.

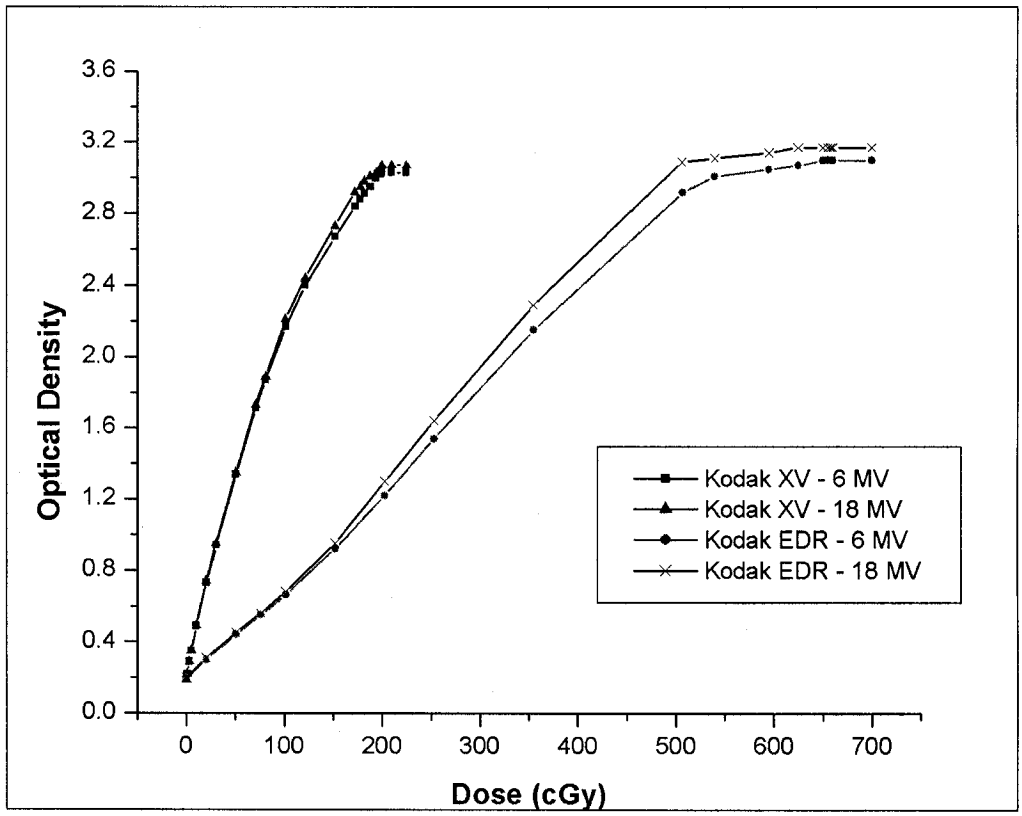

Fig. 7.7. Dose response curves for Kodak ERD and XV films for 6 MV and 18 MV photons, for a 10 × 10 cm² field size at a depth of dose maximum.

7.3. DOSIMETRIC EVALUATION OF AMORPHOUS SILICON EPID

The first part of the thesis was conducted to select the most appropriate EPID system to perform dosimetric studies. Amorphous silicon EPID was chosen for its good image quality, fast acquisition time, linear dose response, and dose rate independence. All of the remaining dosimetric studies were only performed with amorphous silicon EPID.

7.3.1. *Field size dependance*

Dose response of the amorphous silicon aS-500 EPID was measured for different field sizes in order to evaluate the pixel value dependence on field size. Figure 7.8 shows the normalized pixel values for different collimator field sizes from 4 × 4 to 20 × 20 cm^2 with detector at 120 cm SDD. The dose in solid water at the depth of dose maximum was also measured with a Farmer type ion-chamber and is also shown in figure 7.8. The EPID pixels and the ion-chamber readings were normalized to the readings obtained for the 10 × 10 cm^2 field size. Figure 7.8 show for both the EPID and ion chamber experiments, as expected, a rapid increase in scatter contribution (from the collimator and phantom) to the central axis pixel values and ion chamber readings for field sizes up to 10 × 10 cm^2. Beyond this field size the readings increase gradually towards saturation. To better understand the pixel response of aS-500 EPID on field size, the obtained dose values of the aS-500 were divided by the Relative Dose Factor (RDF) of the accelerator. Ideally the resulting plot of "RDF" normalized dose value versus field size would produce a horizontal line at normalized pixel value of 100 %.

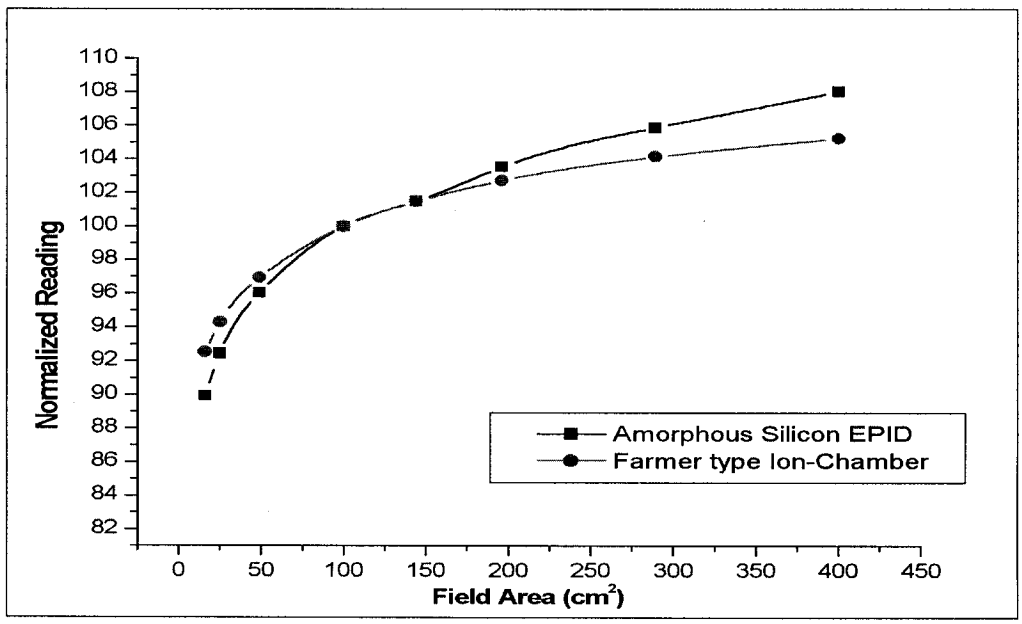

Fig 7.8. Relative pixel value vs. field area for collimator field sizes from 4 × 4 to 20 × 20 cm^2 at 140 cm SDD with 6 MV photon beam. Normalized ion-chamber reading vs field area is also given for the above field sizes. All data points are normalized to the reading obtained at a field size of 10 × 10 cm^2.

The results plotted in figure 7.9 show that the ratio of doses for EPID signal and ionization chamber increase with increasing field size. This can be explained by the presence of side scatter material without a substantial amount of backscatter material in the EPID.

As mentioned before, aS-500 EPID consists of a 1.5 mm of copper plate overlaying a phosphor screen with the flat panel light sensor directly attached to the phosphor screen. Interaction of x-rays with copper plate produces a large amount of scattered electrons. The over response of the detector for larger field sizes is caused by the large amount of side-scattered electrons. With decreasing field size, the amount of side scatter decreases, and therefore, the ratio of the dose determined by the EPID and the ion-chamber also decreases.

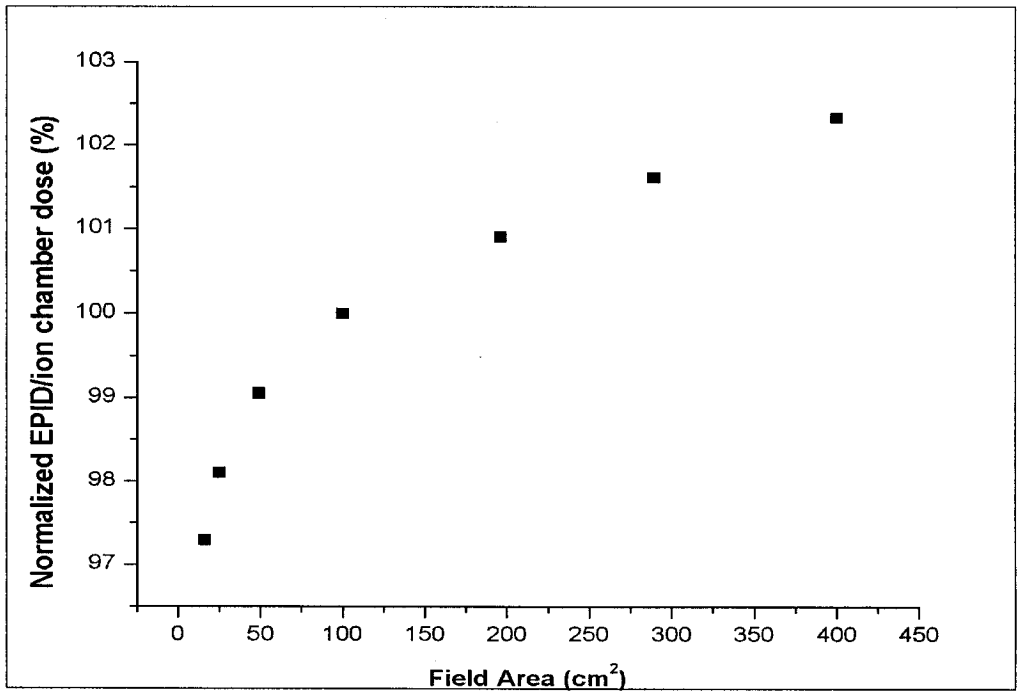

Fig 7.9. Ratio of dose determined with aS-500 EPID to dose measured with a Farmer type ionization chamber for various field sizes. The data is normalized to the ratio obtained at a field size of 10 × 10 cm².

7.3.2. *Static field profile comparisons*

In order to test the relative dosimetry capabilities of the aS-500 flat panel detector, static field profiles extracted from the images were compared with the corresponding ion chamber profiles. A series of data frames were acquired with the flat panel detector for various field sizes. For each data frame taken with radiation "on," a dark frame, obtained under the same conditions but with radiation "off," was acquired and subtracted. In this way, fluctuations primarily due to channel-to-channel variations in preamplifier signal offset and partially due to pixel-to-pixel differences in pixel dark current were largely reduced. The resulting data can then be displayed in various ways, including the extraction of one-dimensional profiles in any direction at any position within the radiation field. For comparison with the flat panel data, beam profiles were obtained with commercial ion chamber as described in section 5.4.2.1. Figures 7.10 (a) and 7.10 (b) show open field profiles obtained at 6 MV and 18 MV, respectively, for both the flat panel detector and ion chamber for 10×10 cm^2 and 20×20 cm^2 field sizes.

At 6 MV, differences of up to 5% lower response inside the field boundaries are observed between flat panel data and the ion chamber data, and differences up to 4 % higher response outside the field boundaries. These differences are due to relatively higher signal response of the phosphor screen to low energy scatter component of the radiation which will increase the background signal in an image acquired by the detector[4]. Compared to air-filled ion chamber, the higher average atomic number ($Z_{eff} \sim 60$ for Gd_2O_2S:Tb) and the higher density of the phosphor screen leads to a detector response which is more strongly dependent on the energy of the radiation interacting in the detector[5]. Moreover, optical photon scatter (or glare) can also cause an increase in background signal. This glare phenomenon is well known in Fluoro based systems due to the presence of mirrors and lenses. The aS-500 detector does not possess any mirrors or lenses, however, the translucent phosphor layer can cause glare effect (which would be much smaller than that due to multiple reflection). This effect is studied by McCurdy *et al.* and they found that the background signal could increase by 3-4 % for 6 MV photon beam, assuming a uniform increase in the scattered dose contribution across the entire detector[6].

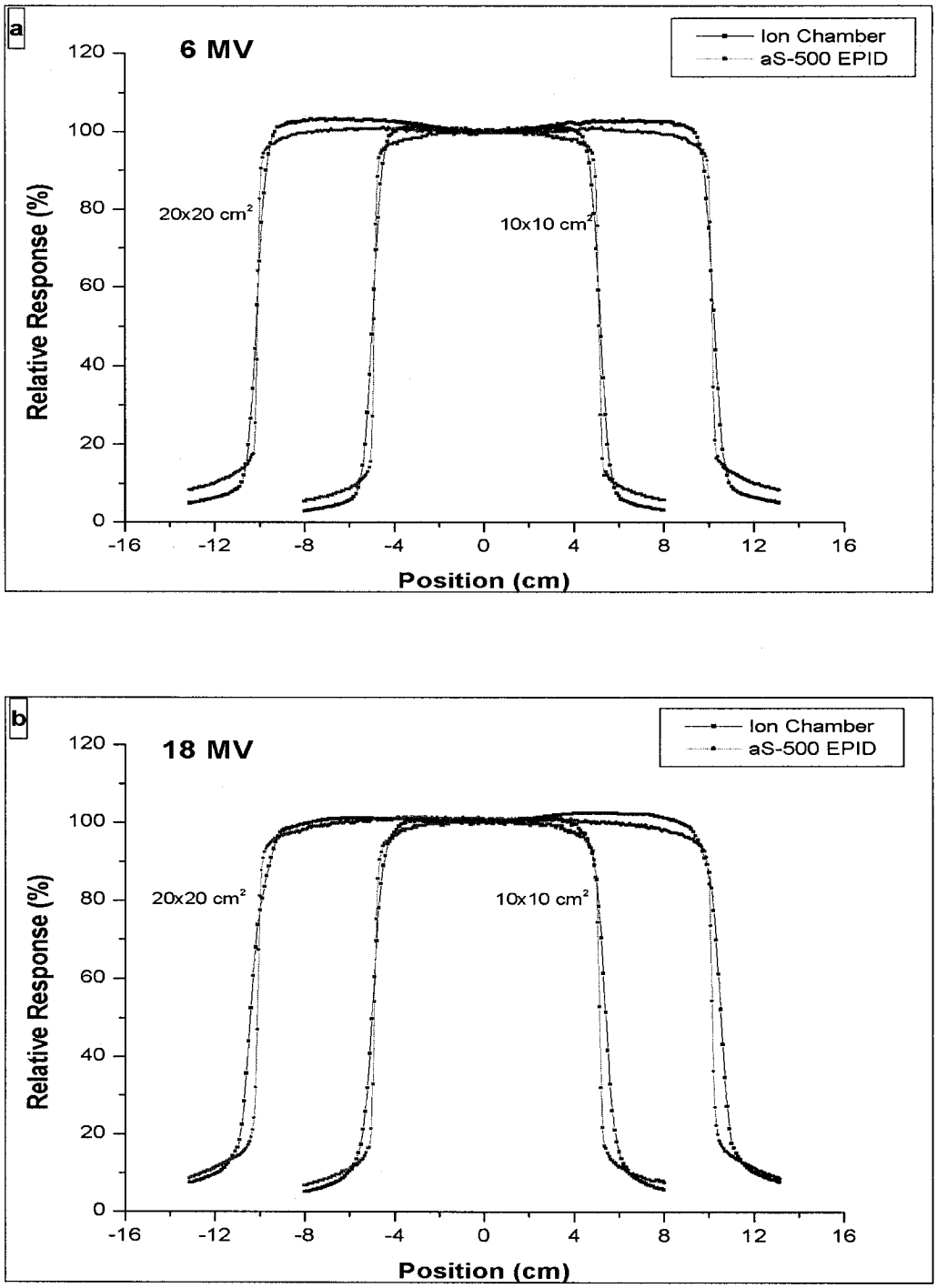

Fig 7.10. Field profiles obtained with the aS-500 Amorphous Silicon flat panel detector with field sizes 10 × 10 cm² and 20 × 20 cm² at beam energies of (a) 6 MV and (b) 18 MV. For comparison, data from a standard Farmer type ion chamber system is shown. All the data were taken at an SDD of 100 cm at the depth of dose maximum for each energy.

The overall increase in background signal would cause the off axis ratios obtained from the flat panel detector to be lower than that obtained with an ion chamber at the edge of the field. At the penumbra region, the increase in background will cause an increase in the off axis ratio as evident from figure 7.10(a).

For the 18 MV beam profile data shown in figure 7.10(b), the difference between the response of the flat-panel detector and that of an ion chamber is less pronounced than at 6 MV, particularly outside the field boundaries. At 18 MV the scatter component is of higher energy, which leads to a lower probability of interaction and therefore to a less enhanced flat-panel detector response (as compared to 6 MV beam).

At both 6 MV and 18 MV, small differences in the slope of the flat-panel and ion chamber data are observed at the field edges. The EPID profiles were more rounded and dropped more rapidly than the ion chamber profiles. These differences are consequence of the higher spatial resolution provided by the flat-panel detector, a 0.78 mm pixel pitch compared to a 6 mm inner diameter of the ion chamber, leading to better field edge definition.

Figures 7.11(a) and 7.11(b) show wedge profiles obtained at 6 MV and 18 MV, respectively, using a 10×10 cm^2 field size, at a depth of d_{max}, and with 45° and 60° static wedges. Wedge profiles obtained with the flat-panel detector show much better agreement with the corresponding ion chamber measurements than the open beam profile comparisons with its corresponding ion chamber measurements. This could be attributed to the fact that there is a shift in photon spectrum towards the higher energy due to attenuation of low energy photons by the wedge resulting in beam hardening. The scattered dose from the static wedge would be minimal because the imager is located about 120 cm from the x-ray source. This is due to the fact that further away the imager is from the source, the smaller the fraction of the total scatter that reaches the imager because of the imager's fixed size. Therefore, the effect of the shift in photon energy spectrum overshadows the effect of the over response of the detector to low energy scattered photons, resulting in better agreement with the ion chamber measurements. The higher spatial resolution provided by the flat-panel detector is also seen clearly from the sharp fall-off in profiles within field boundaries.

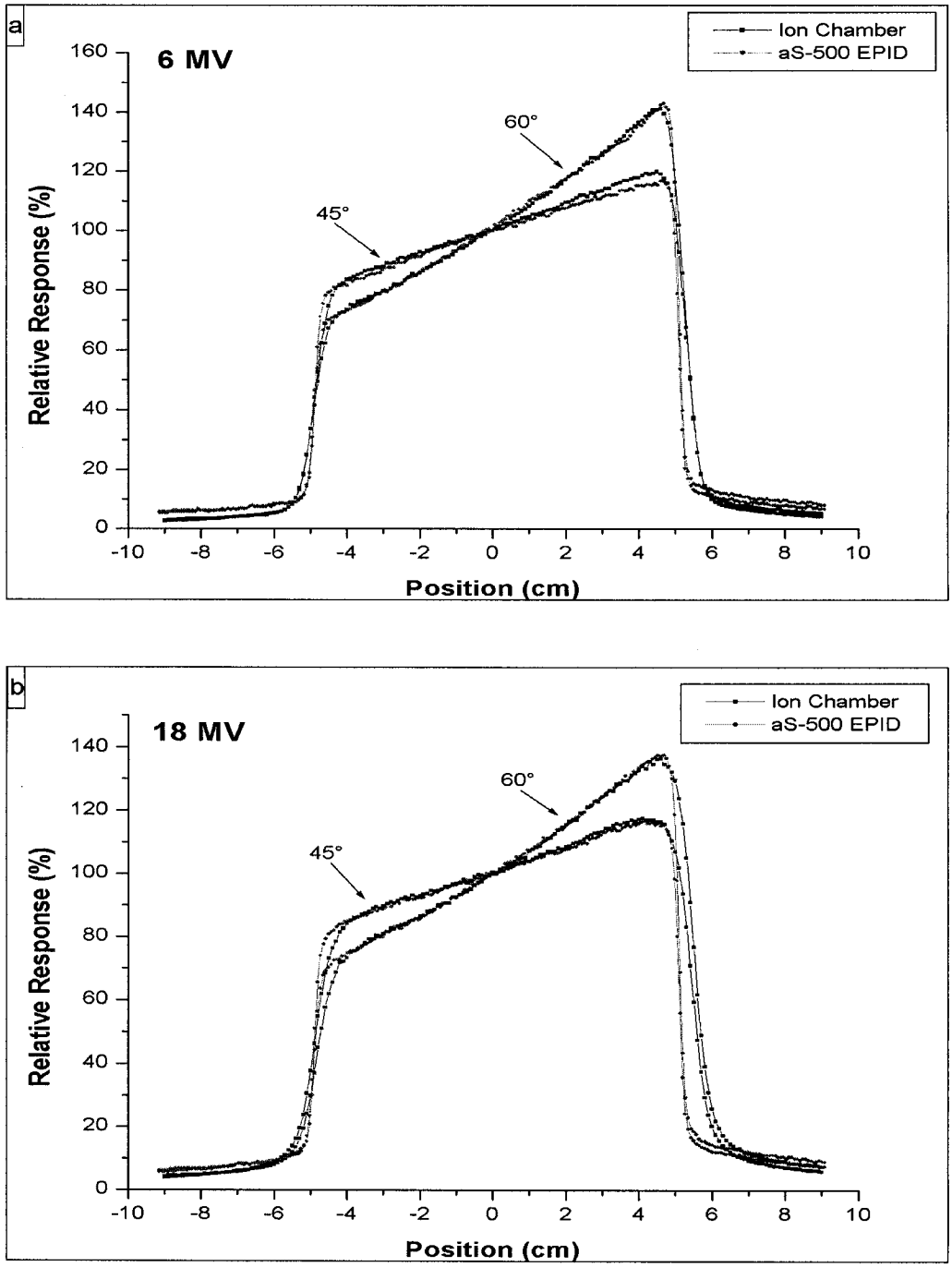

Fig. 7.11. Field profile plots obtained with the aS-500 Amorphous Silicon flat panel detector using 45° and 60° wedges and 10 × 10 cm² field at (a) 6 MV, and (b) 18 MV. For comparison, data from a standard Farmer type ion chamber system is shown. All the data were taken at an SDD of 100 cm at a depth of dose maximum at each energy.

7.3.3. *Dynamic field comparison*

The method for obtaining dynamic images with the aS-500 imager is described in section 5.4.3. All the dynamic images were taken with a dose rate setting of 100 MU/min since the detector's acquisition time is not fast enough to obtain dynamic images with higher dose rates. As mentioned before, the acquisition time of the imager is 200 ms, but with the entire image processing (acquire an image and display it on the monitor), the actual acquisition time is about 350 ms.

Figure 7.12 (a) illustrates the profiles obtained at 6 MV, using a 10 × 10 cm^2 field size, at a depth of d_{max}, and with 45° and 60° dynamic wedges for both ion chamber and aS-500 detector. Figure 7.12 (b) illustrates the profile obtained at 18 MV with 60° dynamic wedges for both ion chamber and aS-500 detector. As one can see from figure 7.12 (a), there is a good agreement between the imager and the ion chamber (<1%) under the thick portion of the wedge, but the profiles differ up to 4 % under the thin portion of the wedge. This again could be attributed to the low energy scattered photons. The dynamic wedge treatment is performed by delivering an open beam followed by delivering the beam with moving jaw to produce the wedge effect. The portion of the treatment with a moving collimator contributes an additional scatter component to under the closing field. These low energy photons will cause the detector to over respond especially at the thin portion of the wedge effect. This is also evident from the higher penumbra for aS-500 as compared to ion chamber measurement under the thin end of the wedge effect as opposed to under the thick end of the wedge effect.

The profiles obtained with the 18 MV beam show less discrepancy between the ion chamber and aS-500 within the field boundaries. This again could be attributed to the higher energy beam resulting in a higher energy scatter component, which in turn leads to a lower probability of interaction and therefore to a less enhanced flat-panel detector response. Sharper penumbra for aS-500 detector is caused by the higher spatial resolution provided by the detector than the ion chamber.

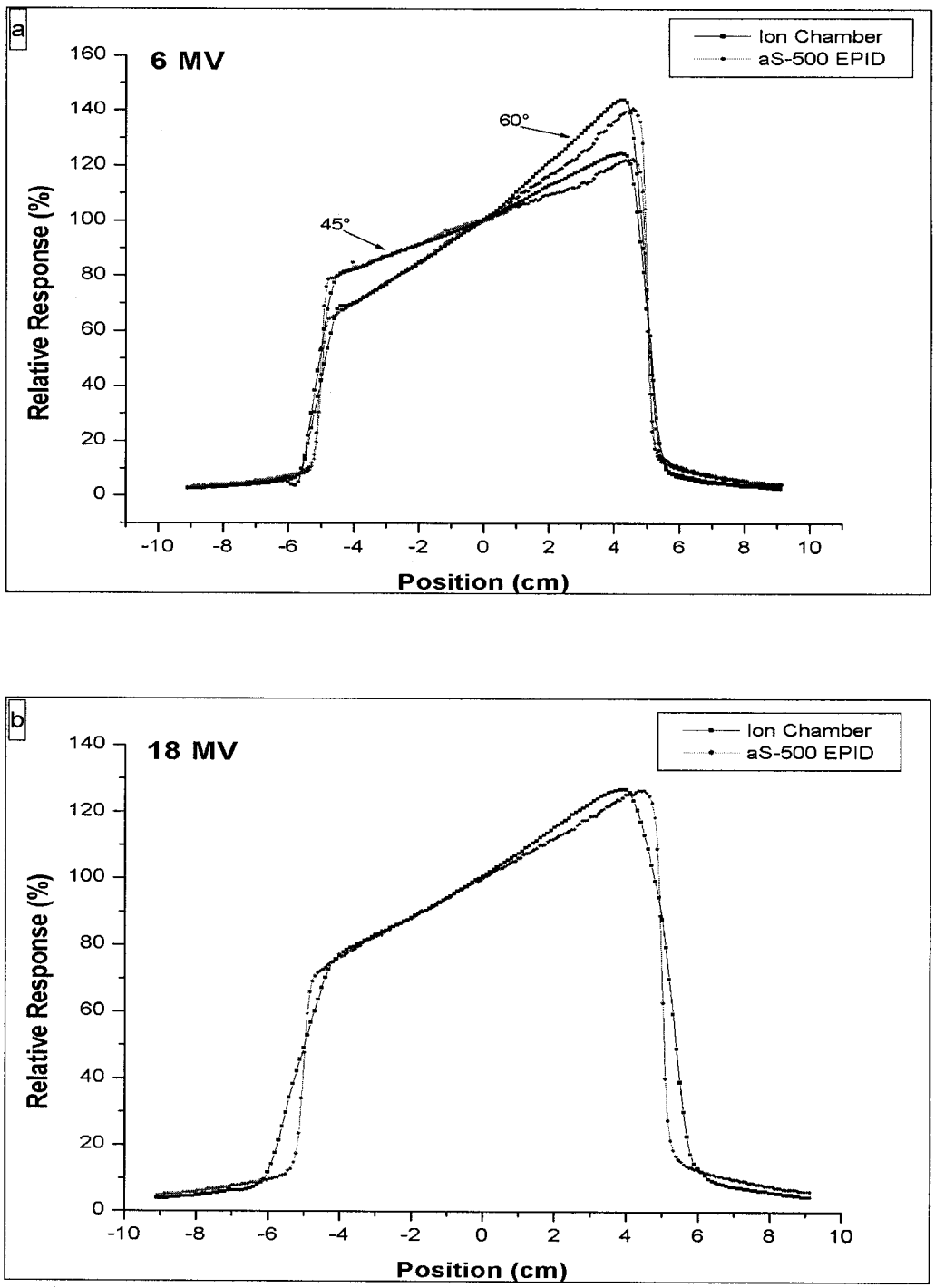

Fig.7.12. Field profile plots obtained with the aS-500 Amorphous Silicon flat panel detector using 45° and 60° dynamic wedges and 10 × 10 cm² field at (a) 6 MV, and 60° dynamic wedge at (b) 18 MV. For comparison, data from a standard Farmer type ion chamber system is shown. All the data were taken at an SDD of 100 cm at a depth of dose maximum with a dose rate of 100 MU/min.

7.3.4. *Intensity modulated radiation therapy (IMRT) study*

To compare relative isodose profiles produced by the aS-500 EPID with relative isodose profiles obtained from film measurements, the film system has to be validated to be used as a standard. Kodak XV film was used for this comparison. Film profile measurements were performed with 60° and 45° dynamic wedges with a field size of 10×10 cm^2 and were compared with ion chamber scans in a water tank to validate our choice of film as the standard. The film profiles agreed to within 2 % with the ion chamber measurements.

The IMRT beams were delivered and recorded with the aS-500 flat panel imager by acquiring sequences of images. Each image was produced by acquiring several frames using an integration time of 200 ms. These frames then could be summed to give images of the complete intensity-modulated beam. An independent measurement of the delivered dose in the phantom was acquired by placing the Kodak XV film between solid water phantoms. The film was taken in the same geometric position as the flat panel detector. Details of the procedure for acquiring the flat panel and film images and plotting the isodose curves are described in section 5.6.

Figure 7.13 shows isodose plots obtained for four IMRT patient treatments. Isodose lines for the aS-500 EPID and Kodak XV film are overlaid to compare how well the isodose curves of aS-500 match with the isodose curves of the film system. All images have been normalized to their value on the central beam axis and figure 7.13 shows results obtained without a patient or phantom in the beam.

(a)

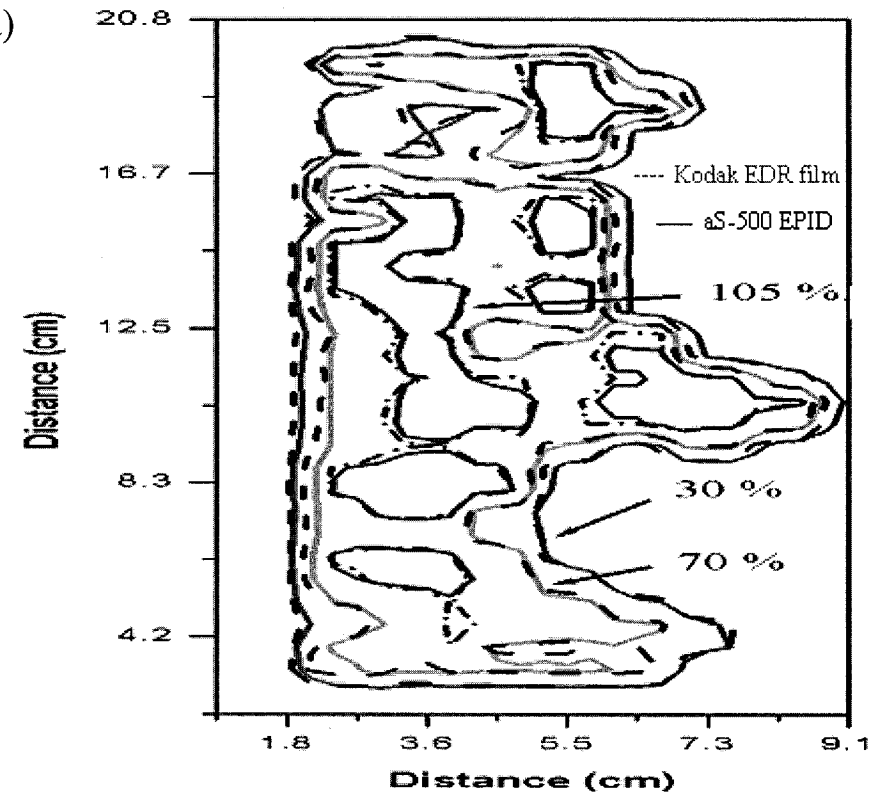
20.8
16.7
12.5
8.3
4.2
Distance (cm)
1.8
3.6
5.5
7.3
9.1
Distance (cm)
---- Kodak EDR film
— aS-500 EPID
105 %
30 %
70 %

(b)

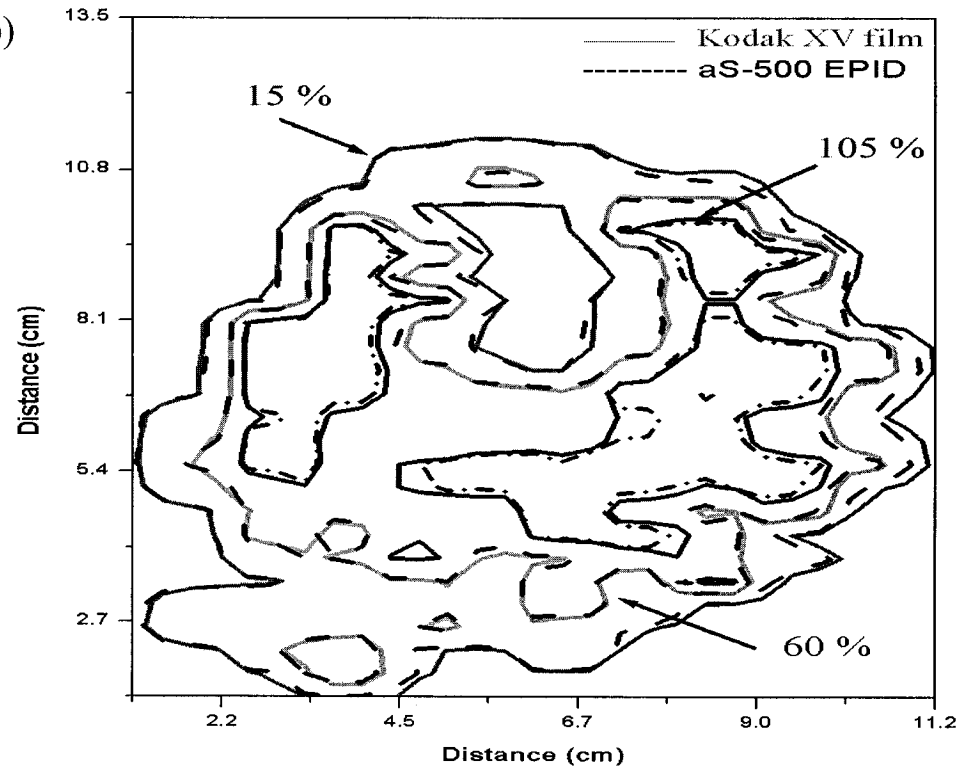
13.5
10.8
8.1
5.4
2.7
Distance (cm)
2.2
4.5
6.7
9.0
11.2
Distance (cm)
Kodak XV film
--------- aS-500 EPID
15 %
105 %
60 %

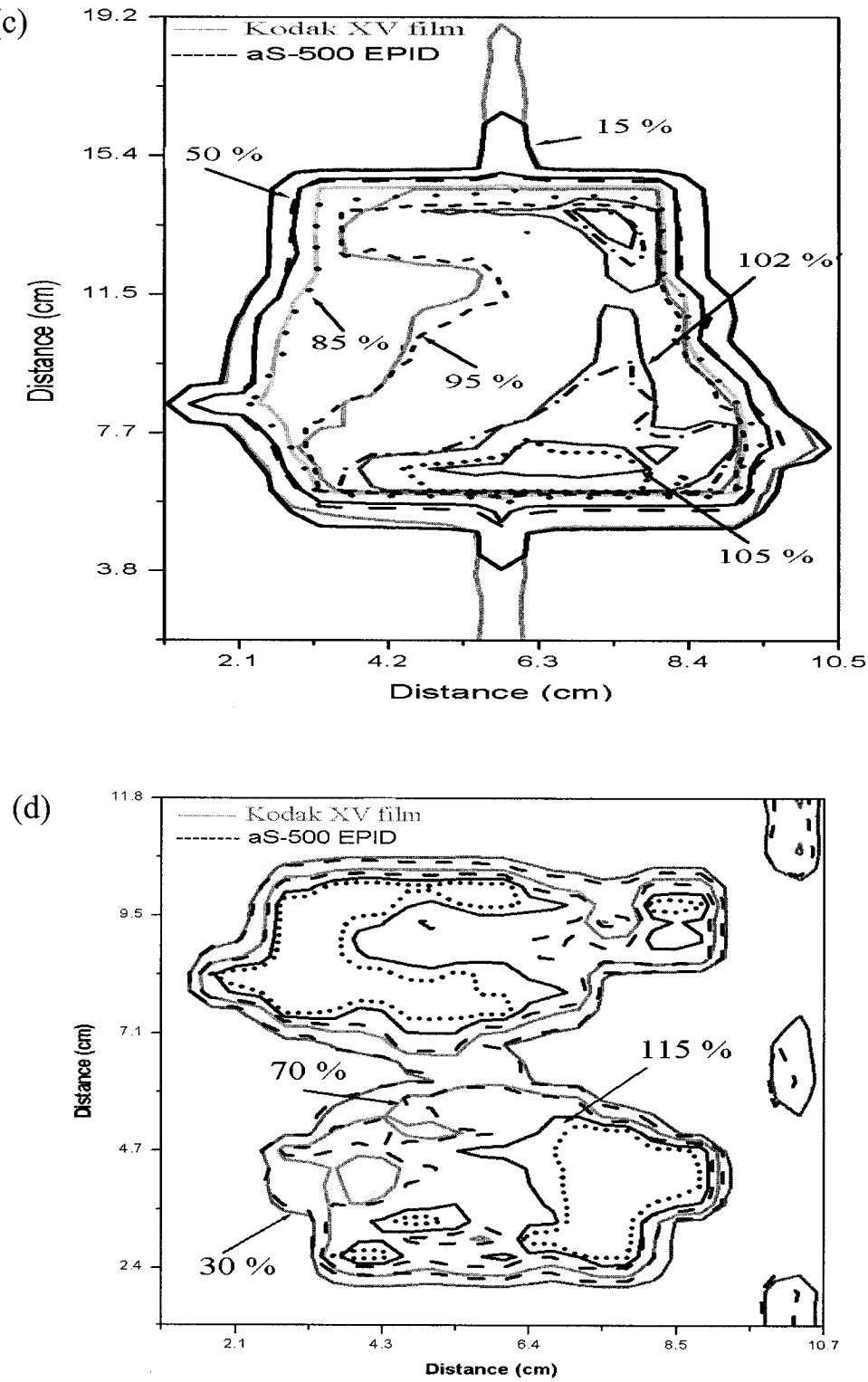

Fig. 7.13. Isodose contour plots for four different studies measured with Kodak XV film (solid) and aS-500 EPID (dashed). All images were obtained with 6 MV photon beam at SDD of 120 cm. All data have been normalized to the central axis point. Studies (a), (b), (c), and (d) comprised of 51, 43, 8, and 37 sub-fields.

Table 7.2 illustrates the proposed values of the confidence limits and action levels for IMRT treatment given by Palta *et al*[7]. According to table 7.2, the measured and the planned isodose lines of 95 % of all the IMRT plans implemented in a clinic has to fall within the confidence limit (P = 0.05). If the differences exceed the action level, then the method of comparison of IMRT plans has to be re-evaluated.

Region	Confidence Limit (P=0.05)	Action level
δ_1 (high dose, small dose gradient)	±3%	±5%
δ_2 (high dose, large dose gradient)	10% or 2 mm	15% or 3 mm
δ_3 (low dose, small dose gradient)	4%	7%
$\delta_{90-50\%}$ (dose fall off)	2 mm	3 mm

Table. 7.2. List of Confidence Limit and Action level for IMRT planning. Limits are given for the i) high dose, small dose gradients, ii) high dose, large dose gradient, iii) low dose, small dose gradient, and iv) dose fall off regions[7].

The first study illustrated in figure 7.13(a) shows the 30%, 70%, and 105% isodose lines for both the aS-500 image and the film image. Isodose lines between the two imaging systems agree within ± 2 mm in most places. The maximum deviation for contour line of 30 % is only 2.5 mm. The 70% and 105% contour lines are also well reproduced in most places, with the figure showing maximum deviation in dose distribution shifted by 3-4 mm. Moreover, if the normalization point falls on a high dose gradient, a small shift in the normalization point between the two images would cause a large miss alignment in isodose lines especially in the high dose gradient regions. Phantom miss- alignment could cause shifts up to 2 mm.

The contour lines of 15%, 60%, and 105% for the second study are overlaid in figure 7.13(b) for both aS-500 EPID and Kodak XV film. This IMRT treatment plan contained 43 segments at the gantry angle of 0°. As one can see from figure 7.13(b) the overlaid isodose lines produced good results with agreement to within ± 2 mm in most places. The largest deviation of about 4 mm is observed between the aS-500 EPID and film contour lines in certain places for the contour line of 105%, although this could be attributed to the high dose gradients present at 105%.

The last two studies illustrated in figures 7.13 (c) and 7.13 (d) respectively show deviations up to 7 mm between aS-500 EPID and Kodak XV film contour lines, especially at the high dose regions. There could be several sources of errors in these comparisons, including the accuracy of film developing and scanning process, and errors associated with positioning the phantom between the two measurements. Since only the last two studies showed large deviations, the above sources of errors were thought to be minor and the normalization point for both of the images were investigated. Upon further examination, the normalization points were found to be situated at a high dose gradient region for these studies. As mentioned before, a large discrepancy in dose may be seen if the normalization point is in a high dose gradient region.

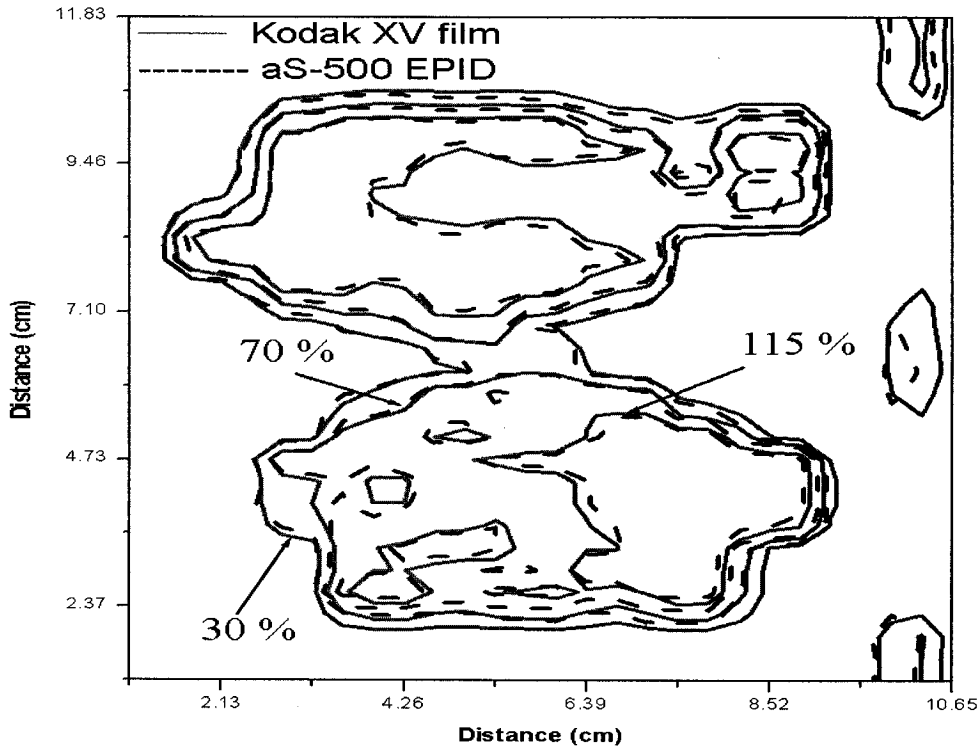

Fig. 7.14. Isodose contour lines for the last study (fig 7.13 (d)) re-normalized at a high dose low dose gradient region for both images obtained with aS-500 EPID and Kodak XV film respectively.

In order to verify whether the normalization point produced the deviation between two sets of isodose lines, both images were re-normalized at a high dose low dose gradient region for the last study. The resulting comparison is illustrated in figure 7.14. The agreement of the isodose contours are very good, being within ± 2 mm in most

places. As evident from these results, choosing a normalization point is very crucial to compare isodose lines of two images. These results also confirm that the method for obtaining the aS-500 and Kodak XV images are very good.

Problem of normalization can be also addressed with a global normalization parameter. This technique involves normalizing the image to an array of pixels. The average value of a pixel array situated on a high dose low gradient region can be used as a normalization value instead a single point on the image.

References

1. M. van Herk, "Physical aspects of a liquilled-filed ionization chamber with pulsed polarizing voltage," Med. Phys. **18**, 692-702, (1991).
2. F. F. Yin, M. C. Shell, and P. Rubin, "Input/ouput characteristics of a matrix ion-chamber electronic portal imaging device," Med. Phys. **21**, 1447-1454, (1994).
3. I. J. Chetty, and P. M. Charland, "Investigation of Kodak extended dose range (EDR) film for megavoltage phonton beam dosimetry," Phys. Med. Biol. **47**, 3629-3641, (2002).
4. H. P. Chan, and K. Doi, "Studies of x-ray energy absorption and quantum noise properties of x-ray screens by use of Monte Carlo simulation," Med. Phys. **11**, 37-46, (1984).
5. Y. E. Mohri, L. E. Antonuk, J. Yorkston, K. –W. Jee, M. Maolinbay, K. L. Lam, and J. H. Siewerdsen, "Relative dosimetry using active matrix flat-panel imager (AMFPI) technology," Med. Phys. **26**, 1530-1541, (1999).
6. B. M. C. McCurdy, K. Luchka, and S. Pistorius, "Dosimetric investigation and portal dose image prediction using an amorphous silicon electronic portal imaging device," Med. Phys. **28**, 911-924, (2001).
7. J. R. Palta, S. Kim, J. G. Li, and C. Liu, "Tolerance limits and action levels for planning and delivery of IMRT," : AAPM 2003 summer school proceedingds, (Medical Physics Publishing, Colarado Springs, 2003).

Chapter 8

Conclusion

8.1. SUMMARY

The goals of this project were to evaluate the imaging performance of various portal imaging devices used in modern radiotherapy facilities, and to use such a device for IMRT dosimetry. The imaging modalities evaluated were the Portal Vision aS-500 amorphous silicon EPID, Portal Vision LC-250 liquid matrix EPID, PortPro fluoro based EPID, Kodak XV film, Kodak EDR film, and Fuji SmartCR computer radiography system.

The performance of each device was evaluated in terms of detector parameters and image quality parameters. The detector parameters investigated included: acquisition time, minimum dose to obtain an image, saturation dose, and pixel depth. The image quality parameters employed to evaluate the modalities were: subject contrast, signal-to-noise ratio, resolution, modulation transfer function, and gantry angle dependence.

In terms of detector parameters, the aS-500 EPID generally outperformed the other imaging modalities. The aS-500 EPID images can be obtained with just 1 monitor unit, an acquisition time of 200 ms with a pixel depth of 16 bit. The PortPro EPID produces images with a faster acquisition time (135 ms) but requires 3 – 4 MUs for the image to stabilize before acquisition. On the other hand, the LC-250 EPID generates higher image quality than PortPro EPID but with a much longer acquisition time (2.56 s). The LC-250 EPID also requires about 4 MUs to generate an image with a pixel depth of 16 bit. In terms of saturation dose, the images obtained with both LC-250 EPID and aS-500 EPID were fully saturated at a dose level of 140 cGy, where as the images obtained from PortPro EPID saturate at much lower dose value of 5 cGy.

The Kodak XV film, Kodak EDR film, and SmartCR computed radiography systems were also investigated in terms of detector parameters. The film systems produce analog images based on the integration of dose. The Kodak XV film was found to have a shorter

dose range (5 cGy – 200 cGy) than the Kodak EDR film (20 cGy – 625 cGy). The SmartCR system has a very short dose range with images saturating at a dose level of 20 cGy and it also produces images with 16 bit pixel depth. Overall, among the EPID systems investigated, the aS-500 amorphous silicon EPID was found to have the most suitable detector parameters for dosimetric purposes.

Next, image quality was investigated for the above imaging modalities. Upon obtaining images to evaluate the image quality parameters, the aS-500 EPID illustrated higher subject contrast, signal-to-noise ratio, and spatial resolution than the other imaging modalities. The aS-500 EPID produced images with high contrast and less noise than the other two EPIDs, and the small pixel dimension enables the detector to acquire images with better spatial resolution at both 6 MV and 18 MV photon beam energies. The PortPro EPID produced very poor image quality parameters due to the large amount of noise resulting from glare. The film systems showed good spatial resolution leading also to good MTF curves, but they demonstrate poor subject contrast and low SNR values. The SNR of the film is mostly degraded due to the film scanner's inability to detect an adequate signal from darker films, in turn increasing noise level in the digitized film images. The SmartCR shows poor spatial resolution and poor subject contrast, but generates a high SNR.

A qualitative analysis of image quality was performed by acquiring images of the Rando phantom (The Phantom Laboratory, New York, USA) under clinical conditions for all the imaging modalities. Figures 8.1 and 8.2 illustrate the images taken with 6 MV and 18 MV photon beams respectively. Although, the printed images in this thesis are of reduced image quality, they represent the general trend that exists. Generally, the aS 500 EPID, SmartCR, and the LC-250 liquid matrix EPID, present similar quality images, whereas the film systems and the PortPro EPID provide reduced image quality images. Generally however, compared to diagnostic radiology images, the images from the megavoltage EPIDs and film systems were of poor quality. The image quality (primarily contrast) in megavoltage portal imaging is limited by the lack of photoelectric interactions in the megavoltage energy range, and attempts to improve the image quality by employing different detectors have not yielded clinically significant improvements especially considering the costs involved.

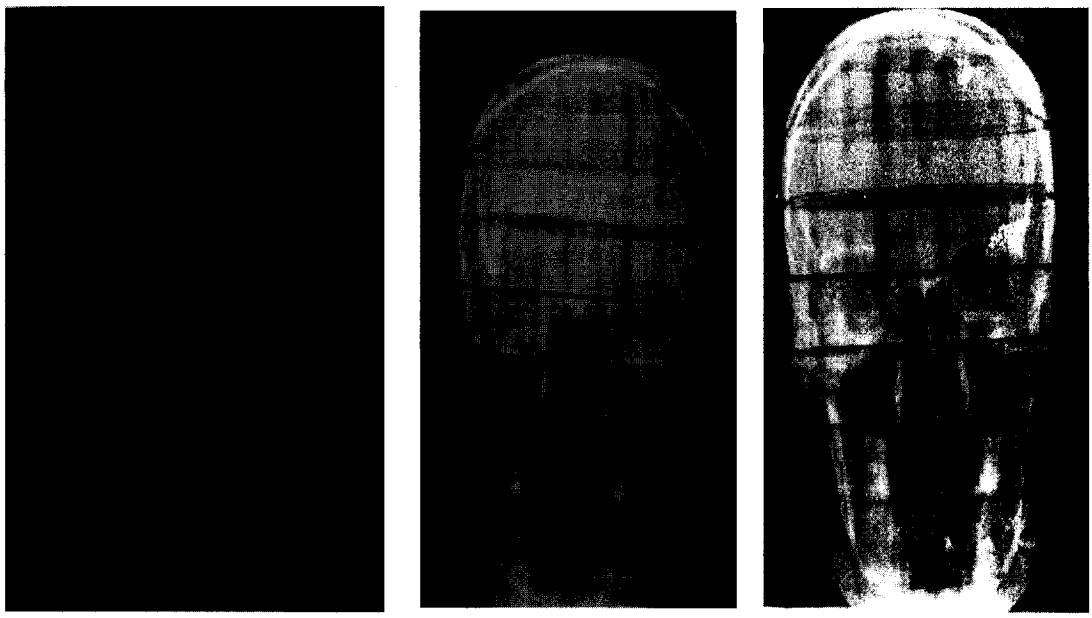

(a) XV film (b) aS-500 (c) SmartCR

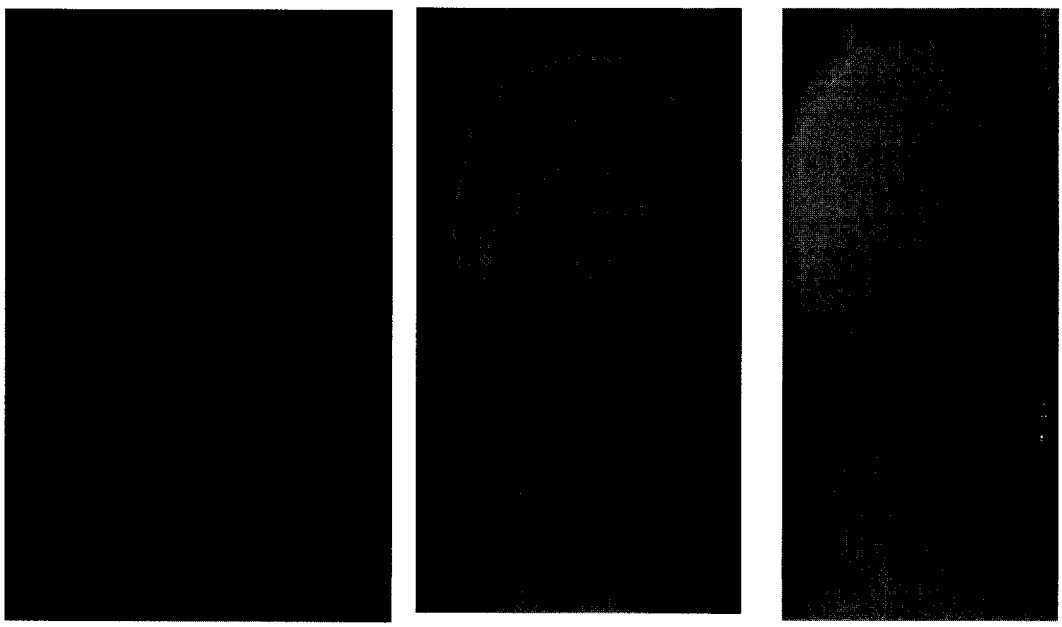

(d) EDR film (e) LC-250 (f) PortPRo

Fig 8.1. Images of Rando head obtained with 6 MV photon beam. All images are taken with the Rando head positioned at SSD 100 cm and the detectors at an SDD of 120 cm.

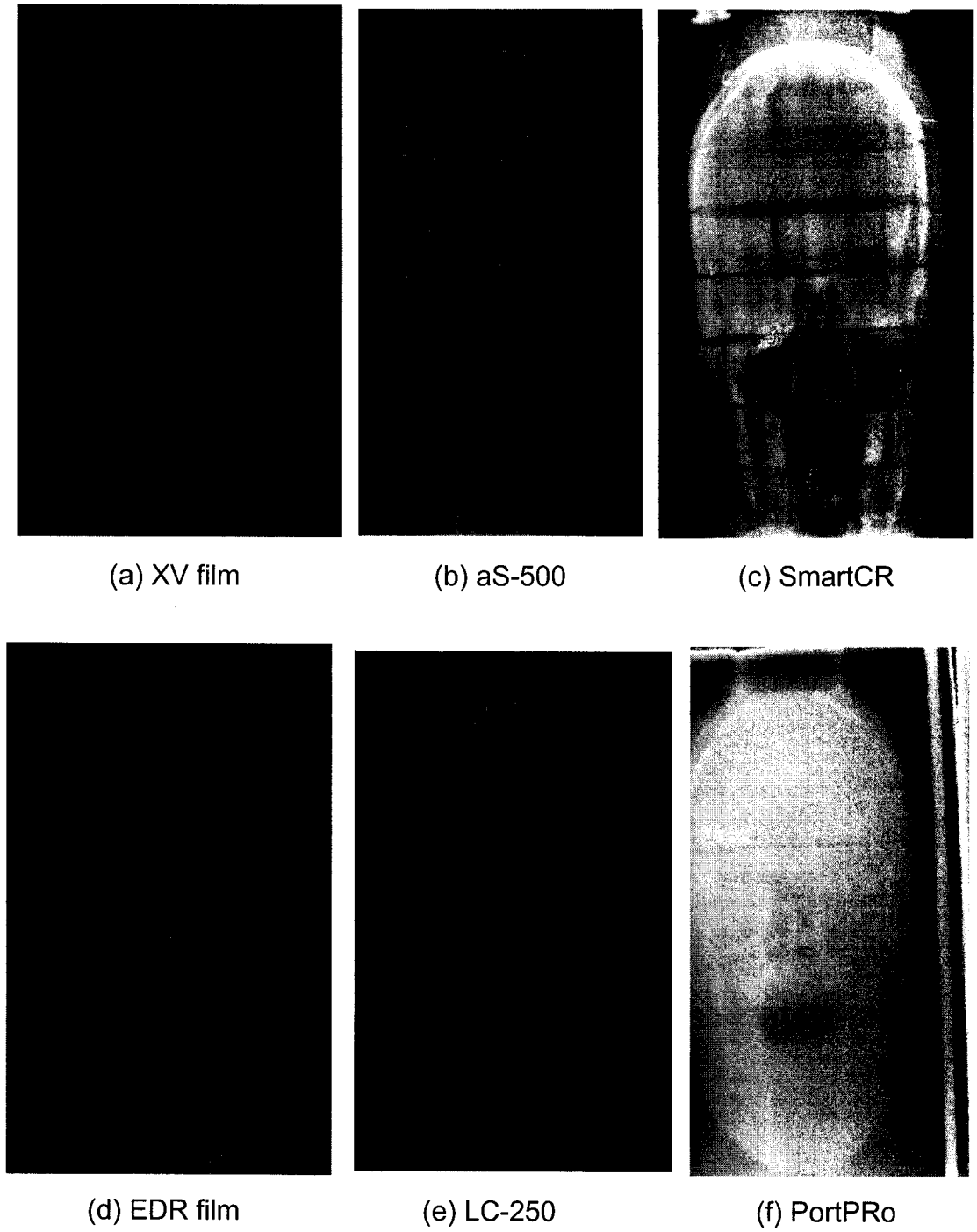

Fig 8.2. Images of Rando head obtained with 18 MV photon beam. All images are taken with the Rando head positioned at SSD 100 cm and the detectors at an SDD of 120 cm.

For example, aS-500 EPID may cost up to twice as much as other EPIDs, but the resulting improvement in image quality is marginal. The startup costs for EPID systems (Hardware, computers, networks, installation, etc.) may be considerable compared to a simple implementation of a film system, but in the long run they may be more economical (no need to purchase and develop a new film for every exposure). Some of the costs may be recovered in an increase in efficiency (faster to use), and a decrease in operational costs (one time equipment purchase), as seen when comparing EPIDs to film systems. The availability of a digital image instantly for review and analysis is also an appealing feature of EPIDs, especially in a busy clinical environment.

The second part of the thesis involved the dosimetric evaluation of the aS-500 EPID for the purposes of IMRT quality assurance. Generally the fast acquisition, high resolution, energy and dose rate independence, together with a good dose response range (0 cGy – 140 cGy) make the aSi EPID a good candidate for IMRT dosimetry. IMRT quality assurance tests were performed for four clinical cases using the aS-500 EPID. The same experiments performed with Kodak XV film were used as a standard for comparison. The agreement between the dose distributions measured with the two imaging systems was generally good, with isodose lines agreeing to within ± 2 mm in most cases. In some places, there were differences as high as 3 to 4 mm, which could have been caused by the phantom miss-alignment or dose normalization issues. If the normalization point falls in a region of high dose gradient, a small shift in normalization point between the two images would cause a large discrepancy in the position of isodose lines. By renormalizing in a low dose gradient region, it was shown that position of the isodose lines could be corrected. As is evident from these results, choosing a normalization point is very crucial to compare isodose lines of two images.

The use of aS-500 for IMRT QA does have some drawbacks. The fast (200ms) multiple frame acquisition together with the low saturation dose of the imager (140 cGy) may compromise the QA process. Generally the EPID can only approximate an integrating dosimeter by a acquiring a large number of discrete frames and summing them. For example, IMRT treatments are generally delivered with a dose rate of at least 300 MU/min, but the QA images must be acquired with a dose rate of 100 MU/min because the detector's acquisition time is not fast enough to obtain dynamic images with

higher dose rates. Also, it is sometimes impossible to deliver the number of monitor units that the patient receives because the dose delivered could saturate the imager, and therefore a lower monitor unit setting must be used. Another limitation of using EPIDs to perform IMRT QA treatment plan is that the image can only be obtained at a single plane perpendicular to the beam. There are dosimetric inconsistencies as well, profile comparisons between the aS-500 EPID and ion chamber showed that the aS-500 EPID over-responds as much as 4 % to the low energy scattered photons. Since the IMRT treatments comprise of small fields, the scatter from the MLC would not contribute to the total measured signal considerably.

8.2. FUTURE WORK

Although great strides have been made with Electronic Portal Imaging Devices, a great deal of research remains to be done in this field. Improvements currently under development by various manufactures promise portal images of improved quality. These improvements in image quality are essential for the success of portal imaging. Nevertheless, much development needs to be directed toward making portal imaging more convenient and reliable.

Tomographic imaging techniques are being adapted for use in radiotherapy treatment verification. Conventional Computed Tomography (CT) uses fan beam geometry, with the patient translating through the beam. The cone beam CT reconstructs the images using a 3-D fan beam or "cone beam" for data acquisition. The advantage of course is the fine resolution obtained on all slices imaged due to the true 3-D volume acquisition and reconstruction. The cone beam technology is being applied to radiotherapy for treatment position verification. The treatment time "cone beam" CT can be compared to the treatment planning CT and the patient position adjusted accordingly[1]. Currently there are commercially available megavoltage or kilovoltage imaging options. The kilovoltage option requires additional hardware, where the megavoltage imager uses the existing megavoltage source and portal imager. The biggest impact is the ability to verify the position of anatomic structures otherwise not seen on megavoltage transmission port films.

A cheap and effective ultrasound system such as BAT (B-mode Acquisition and Targeting) system (Nomos Corporation, Sewickley, PA) combines easy to obtain ultrasound data acquired pre-treatment to CT contours acquired during the planning process to achieve similar results. The advantage is the patient receives no additional dose, however the ultrasound images may be difficult to interpret, and require manual intervention to acquire them.

For portal dosimetry with EPIDs, a simple, yet effective application would consist of a direct comparison of a measured portal dose image with a theoretically predicted portal dose image. Discrepancies between the measured and predicted image could indicate treatment delivery errors, which may be corrected once identified. Ideally the comparison step would be fully computerized using software and performed within the first few monitor units delivered in a treatment fraction[2].

Transit dosimetry using the a-Si EPID could involve the removal of scatter from the measured portal image, then backprojecting the remaining primary component through the patient computed tomography (CT) data set which allows a calculation of deposited dose in the patient[3]. Alternatively, the primary fluence from a measured a-Si portal dose image could be derived and the resulting fluence could be back projected through the patient to yield the primary fluence distribution in the patient. This distribution can be then convolved with dose deposition kernels to derive the dose distribution in the patient[4].

Finally, the clinical implementation of EPIDs will continue to be both an opportunity and a challenge. The centers that have embraced this technology have demonstrated that important improvements in geometric accuracy are possible.

References

1. D. A. Jaffray, "X-ray-Guided IMRT," : AAPM 2003 summer school proceedingds, (Medical Physics Publishing, Colarado Springs, 2003).

2. M. Kroonwijk, K. L. Pasma, S. Quint, P. C. M. Koper, A. G. Visser, and B. J. M. Heijmen, "In vivo dosimetry for prostate cancer patients using an electronic portal imaging device (EPID); detection of internal organ motion," Radiother. Oncol. **49**, 124-132 (1998).

3. T. McNutt, T. R. Mackie, P. Reckwerdt, and N. Papanikolaou, "Calculation of portal dose distributions from portal dose images using the convolution/superposition method," Med. Phys. **23**, 1381-1392 (1996).

4. P. M. Evans, E. M. Donovan, N. Fenton, V. N. Hansen, I. Moore, M. Partridge, S. Reise, B. Suter, J. R. Symonds-Tayler, and J. R. Yarnold, "Practical implementation of compensators in breast radiotherapy," Radiother. Oncol. **49**, 255–265 (1998).

Bibliography

(N.B. The numbers in square parentheses refer to the pages in which the references are cited.)

AAdeyemi, and J. Lord, "An audit of radiotherapy patient doses measured with in vivo semiconductor detectors," The Brit. J of Radio. **70**, 399–408, (1997). [48]

P. R. Almond, P. J. Biggs, B. M. Coursey, W. F. Hanson, M. S. Huq, R. Nath, and D. W. O. Rogers, "AAPM's TG-51 protocol for clinical reference dosimetry of high-energy photon and electron beams," Med. Phys. **26**, 1847-1870, (1999). [62]

L. E. Antonuk, "Electronic portal imaging devices: a review and historical perspective of contemporary technologies and research," Phys. Med. Biol. **47**, R31-R65, (2002). [4,18,20,40,44]

L. E. Antonuk, J. Boudry, W. Huang, D. L. McShan, E. J. Morton, and J. Yorkston, "Demonstration of megavoltage and diagnostic x-ray imaging with hydrogenated amorphous silicon arrays," Med. Phys. **19**, 1455-1465, (1992). [26,27,29]

G. T. Barnes, "The use of bar pattern test objects in assessing the resolution of film/screen systems," in The Physics of Medical Imaging: Recording System Measurements and Techniques, edited by A. G. Haus (AIP, New York, NY, 1979). [70]

A. Bel, P. H. Vos, P. T. Rodrigus, C. L. Creutzberg, A. G. Visser, J. C. Stroom, and J. V. Lebesque, "High-precision prostate cancer irradiation by clinical application of an offline patient setup verification procedure, using portal imaging," Int. J. Radiat. Oncol., Biol., Phys. **35**, 321–332, (1996). [4]

A. Bel, R. Keus, R. E. Vijlbrief, and J. V. Lebesque, "Setup deviations in wedged pair irradiation of parotid gland and tonsillar tumors, measured with an electronic portal imaging device," Radiother. Oncol. **37**, 153–159, (1995). [4]

S. Benner, B. Rosengren, H. Wallman, et al., "Television monitoring of a 30 MV x-ray beam," Phys Med Biol. **7**, 29-34, (1962). [6]

J. Bijhold, J. V. Lebesque, A. A. Hart, and R. E. Vijlbrief, "Maximizing setup accuracy using portal images as applied to a conformal boost technique for prostatic cancer," Radiother. Oncol. **24**, 261–271, (1992). [4]

R. Boellaard, "In vivo dosimetry with a liquid-filled electronic portal imaging device," PhD thesis, Free University, Amsterdam, (1998). [52]

R. Boellaard, M. van Herk, and B. J. Mijnheer, "A convolution model to convert transmission dose images to exit dose distributions," Med. Phys. **24**, 189–199, (1997). [52]

R. Boellaard, M. van Herk, and B. J. Mijnheer, "First clinical test using a liquid-filled electronic portal imaging device and convolution model for the verification of the midplane dose," Radiother. Oncol. **47**, 303-312, (1998). [53]

R. Boellaard, M. van Herk, and B. J. Mijnheer, "The dose response relationship of a liquid-filled electronic portal imaging device," Med. Phys. **23**, 1601-1611, (1996). [52]

A. L. Boyer, L. Antonuk, A. Fenster, M. Van Herk, H. Meertens, P. Munro. L. E. Reintein, J. Wong, "A review of electronic portal imaging devices (EPIDs)," Med. Phys. **19**, 1-16, (1992).

[7,8,36,39,41,43,44,89]

S. C. Bushong, *Radiologic Science for Technologists* 6th Edition (Mosby-Year Book, 1997). [1,2]

J. R. Cameron, N. Suntharalingam, and G. N. Kenney, *Themoluminecent Dosimetry* (University Wisconcin Press, Madison, 1968). [48]

Canadian Cancer Society Web Site. Web Page : Canadian Cancer Statistics (http://www.cancer.ca). [2]

H. P. Chan, and K. Doi, "Studies of x-ray energy absorption and quantum noise properties of x-ray screens by use of Monte Carlo simulation," Med. Phys. **11**, 37-46, (1984). [18,109]

J. Chavaudra, G. Marinello, A. M. Brule, and J. Nguyen, "Practical use of lithium borated in thermoluminecent dosimetry," J Radiol Electrol Med Nucl. **37**, 435-445, (1976). [48]

I. J. Chetty, and P. M. Charland, "Investigation of Kodak dose range (EDR) film for megavoltage photon beam dosimetry," Phys. Med. Biol. **47**, 3629-3641, (2002). [56,105]

M. Ciocca, L. Landoni, C. Italia, P. Montanaro, P. Canesi, and R. Valdagni, "Quality control in the conservative treatment of breast cancer: patient dosimetry using silicon detectors," Radiother.Oncol. **22**, 304–307, (1991). [48]

C. L. Creutzberg, V. G. Althof, H. Huizenga, A. G. Visser, and P. C. Levendag, "Quality assurance using portal imaging: The accuracy of patient positioning in irradiation of breast cancer," Int. J. Radiat. Oncol., Biol., Phys. **25**, 529–539, (1993). [4]

T. S. Curry III, J. E. Dowdey, and R. C. Murry. *Christensen's Physics of Diagnostic Radiology* 4th Edition (Lippincott Williams & Wilkins, Media, 1990). [2,12,13,55]

M. L. P. Dirkx, M. Kroonwijk, J. C. J. deBoer, and B. J. MHeijmen, "Daily dosimetric quality control of the MM50 racetrack microtron using an electronic portal imaging device," Radiother. Oncol. **37**, 55–60, (1995). [49]

K. Doi, G. Holje, L-N Loo, H-P Chan, J. M. Sandrik, R. J. Jennings, and R. F. Wagner, "*MTF*'s and Wiener spectra of radiographic screen-film systems," HHS Publ. No. 82-8187 (FDA), (1979). [95]

R. T. Droega, "A megavoltage MTF measurement technique for meatl screen-film detectors," Med. Phys. **6**, 272-279, (1979). [42,44]

R. T. Droege, "A practical method to routinely monitor resolution in digital images," Med. Phys. **10**, 337-343, (1983). [68,70]

P. B. Dunscombe, K. Fox, S. Loose, and K. Leszczynski, "The investigation and rectification of field placement errors in the delivery of complex head and neck fields," Int. J. Radiat. Oncol., Biol., Phys. **26**, 155–161, (1993). [4]

P. B. Dunscombe, S. Loose, and K. Leszczynski, "Sizes and sources of field placement error in routine irradiation for prostate cancer," Radiother. Oncol. **26**, 174–176, (1993). [4]

A. Dutreix, "When and how can we improve precision in radiotherapy?," Radiother Oncol. **2**, 275-292, (1984). [3]

Eliav – Medical Imaging Syatems Web Site. Web Page: PortPro – Digital imaging for radiotherapy (http://www.eliav.com/portpro.htm). [64]

M. M. Elkind, "DNA damage and cell killing: cause and effect?," Cancer, **56**, 2351-2363, (1985). [3]

M. Essers and B. J. Mijnheer, "In vivo dosimetry during external photon beam radiotherapy," Int. J.Radiat. Oncol. Biol. Phys. **43**, 245–259, (1999). [48]

M. Essers, B. R. Hoogervorst, M. van Herk, H. Lanson, and B. J. Mijnheer, "Dosimetric characteristic of a liquid-filled portal imaging device," Int. J. Radiat. Oncol. Biol. Phys. **33**, 1265-1272, (1995). [52]

M. Essers, J. H. Lanson, and B. J. Mijnheer, "In vivo dosimetry during conformal therapy of prostatic cancer," Radiother. Oncol. **29**, 271–279, (1993). [48]

M. Essers, J. H. Lanson, G. Leunens, T. Schnabel, and B. J. Mijnheer, "The accuracy of CT-based inhomogeneity corrections and in vivo dosimetry for the treatment of lung cancer," Radiother.Oncol. **37**, 199–208, (1995). [48]

M. Essers, R. Keus, J. H. Lanson, and B. J. Mijnheer, "Dosimetric control of conformal treatment of parotid gland tumors," Radiother. Oncol. **32**, 154–162, (1994). [48]

P. M. Evans, E. M. Donovan, N. Fenton, V. N. Hansen, I. Moore, M. Partridge, S. Reise, B. Suter, J. R. Symonds-Tayler, and J. R. Yarnold, "Practical implementation of compensators in breast radiotherapy," Radiother. Oncol. **49**, 255–265, (1998). [51,128]

P. M. Evans, V. N. Hansen,W. P. MMayles, W. Swindell, M. Torr, and J. R. Yarnold, "Design of compensators for breast radiotherapy using electronic portal imaging," Radiother. Oncol. **37**, 43–54, (1995). [51]

A. Ezz, P. Munro, A. T. Porter, J. Battista, D. A. Jaffray, A. Fenster, and S. Osborne, "Daily monitoring and correction of radiation field placement using a video-based portal imaging system: A pilot study," Int. J. Radiat. Oncol., Biol., Phys. **22**, 159–165, (1992). [4]

T. Falco, "Analysis of metal/film and novel metal/a-SE portal detectors," PhD thesis, McGill University, Montreal, (1999). [65,67]

Fuji Medical Imaging Web Site. Web Page: Computed Radiograpys SmartCR (http://www.fujimed.com/medical/cr_smartcr_specs.html). [64]

J. Gildersleve, D. P. Dearnaley, P. M. Evans, M. Law, C. Rawlings, and W. Swindell, "A randomised trial of patient repositioning during radiotherapy using a megavoltage imaging system," Radiother. Oncol. **31**, 161–168, (1994). [4]

M. Goitein, and J. Buss, "Immobilization errors: Some theoritical considerations," Radiology, **117**, 407-412, (1975). [3]

E. E. Grein, R. Lee, and K. Luchka, "An investigation of a new amorphous silicon electronic portal imaging device for transit dosimetry," Med. Phys. **29**, 2262-2268, (2002). [46,50]

S. E. Griffiths, R. G. Pearcey, and J. Thorogood, "Quality control in radiotherapy: The reduction of field placement errors," Int. J. Radiat. Oncol., Biol., Phys. **13**, 1583–1588, (1987). [4]

E. Grusell, and G. Rikner, "Evaluation of temperature effects in p-type silicon detectors," Phys. Med.Biol. **31**, 527–534, (1986). [48]

V. N. Hansen, P. M. Evans, and W. Swindell, "Extraction of primary signal from EPIDs using only forward convolution," Med. Phys. **24**, 1477-1484, (1997). [51]

V. N. Hansen, P. M. Evans, and W. Swindell, "The application of transit dosimetry to precision radiotherapy," Med. Phys. **23**, 713-721, (1996). [51]

H. F. Hare, S. W. Lippincott , and D. Sawyer, "Physical and clinical aspects of supervoltage rotational therapy," Radiology. **57**, 157-168, (1951). [5]

A. G. Haus, *Historical developments in film processing and medical imaging*, in Haus AG(ed):Film Processing and Medical Imaging (Wisconsin, Medical Physics Publshing, 1993). [5]

A. G. Haus, S. M. Pinsky, and J. E. Marks, "A technique for imaging patient treatment area during therapeutic radiation exposure," Radiology. **97**, 653-656, (1970). [5]

Healthy Lifestyle Centre. Web page: Treatment Procedures – Cancer 2002 (http://jhhs.client.web-health.com/web-health/topics/GeneralHealth/generalhealthsub/ Radiationtherapy.html). [3]

B. J. M. Heijmen, A. G. Visser, and H. Huizenga, "In-vivo dose measurements using an electronic portal imaging device: a feasibility study," Radiother. Oncol. **24**, (supplement):S25, (1992). [49]

B. J. M. Heijmen, J. C. Stroom, H. Huizenga, and A. G. Visser, "Application of a fluoroscopic portal imaging system with a CCD camera for accurate in-vivo dosimetry," Med. Phys. **20**, 870, (1993). [49]

B. J. M. Heijmen, K. L. Pasma, MKroonwijk, A. GVisser, and H. Huizenga, "Prediction of portal dose images for in vivo dosimetry in radiotherapy," Med. Phys. **22**, 992, (1995). [49]

M. G. Herman, R. A. Abrams, and R. R. Mayer, "Clinical use of on-line portal imaging for daily patient treatment verification," Int. J. Radiat. Oncol., Biol., Phys. **28**, 1017–1023, (1994). [39,41,42]

S. Heukelom, J. H. Lanson, and B. J. Mijnheer, "Comparison of entrance and exit dose measurements using ionization chambers and silicon diodes," Phys. Med. Biol. **36**, 47–59, (1991). [4]

S. Heukelom, J. H. Lanson, G van Tienhoven, and B. J. Mijnheer, "In-vivo dosimetry during tangential breast treatment," Radiother. Oncol. **22**, 269–279, (1991). [48]

R. A. Holroyd, and D. F. Anderson, "The physics and chemistry of room-temperature liquid-filled ionization chambers," Nucl. Instr. and Meth. **A236**, 294-299, (1985). [21]

H. Huizenga, P. C. Levendag, P. M. De Porre, and A. G. Visser, "Accuracy in radiation field alignment in head and neck cancer: A prospective study," Radiother. Oncol. **11**, 184–187, (1988). [4]

M. A. Hunt, T. E. Schultheiss, G. E. Desobry, M. Hakki, and G. E. Hanks, "An evaluation of setup uncertainties for patients treated to pelvic sites," Int. J. Radiat. Oncol., Biol., Phys. **32**, 227–233, (1995). [4]

M. A. Hunt, G. J. Kutcher, C. Burman, D. Fass, L. Harrison, S. Leibel, and Z. Fuks, "The effect of setup uncertainties on the treatment of nasopharynx cancer," Int. J. Radiat. Oncol., Biol., Phys. **27**, 437–447, (1993). [4]

ICRU Report No. 33: *Radiation Quantities and Units. Techinical report*, International Commision on Radiation Units and Measurements, Washigton, DC, (1980). [3]

D. A. Jaffray, J. J. Battista, A. Fenster, and P. Munro, "X-ray scatter in megavoltage transmission radiography: Physical characteristics and influence on image quality," Med. Phys. **21**, 45–60, (1994). [12]

D. A. Jaffray, "X-ray-Guided IMRT," : AAPM 2003 summer school proceedingds, (Medical Physics Publishing, Colarado Springs, 2003). [127]

H. E. Johns and J. Cunningham, The Physics of Radiology 4th Edition (Charles C. Thomas, Sprignfield, 1983). [39]

M. C. Kirby and P. C. Williams, "Clinical aaplications of composite and realtime megavoltage imaging," Cli. Oncol. **7**, 308–316, (1995). [49]

M. C. Kirby, and P. C. Williams, "The performance of a fluoroscopic electronic portal imaging device modified for portability," Br. J. Radiol. **72**, 1000-1005, (1999). [53]

M. C. Kirby and P. C. Williams, "The use of an electronic portal imaging device for exit dosimetry and quality control measurements," Int. J. Radiat. Oncol. Biol. Phys. **31**, 593–603, (1995). [49,54]

A. H. Knowlton, *General principles of radiation therapy* (Hall Medical Publishers, Boston, 1982). [2]

M. Kroonwijk, K. L. Pasma, S. Quint, P. C. M. Koper, A. G. Visser, and B. J. M. Heijmen, "In vivo dosimetry for prostate cancer patients using an electronic portal imaging device (EPID); detection of internal organ motion," Radiother. Oncol. **49**, 124-132, (1998). [51,128]

T. Lahtinen, H. Puurunen, P. Simonen, A. Pekkarinen, and A. Väänänen, *Dosimetry in radiotherapy* (International Atomic Energy Agency, Vienna, 1988). [48]

P. C. Lee, J. M. Sawicka, and G. P. Glasgow, "Patient dosimetry quality assurance program with a commercial diode system," Int. J. Radiat. Oncol. Biol. Phys. **29**, 1175–1182, (1994). [49]

J. Leong, and D. Shimm, "A method for consistent precision radiation therapy," Radiother Oncol. **3**, 89-92, (1985). [53,54]

J. Leong, "Use of digital fluoroscopy as an on-line verification device in radiation therapy," Phys. Med. Biol. **31**, 985-992, (1986). [5,18,49]

G. Leunens, J van Dam, A. Dutreix, and E van der Schueren, "Quality assurance in radiotherapy by in vivo dosimetry. 1. Entrance dose measurements, a reliable procedure," Radiother. Oncol. **17**, 141–151, (1990). [48]

G. Leunens, J van Dam, A. Dutreix, and E van der Schueren, "Quality assurance in radiotherapy by in vivo dosimetry. 2. Determination of the target absorbed dose," Radiother. Oncol. **19**, 73–87, (1990). [48]

G. Leunens, J. Verstraete, J van Dam, A. Dutreix, and E van der Schueren, "In vivo dosimetry for tangential breast irradiation: role of the equipment in the accuracy of dose delivery," Radiother.Oncol. **22**, 285–289, (1991). [48]

A. S. Lichter, and T. S. Lawrence, "Recent advences in radiation oncology," The New England Journal of Medicine. **332**, 370-372, (1995). [3]

A. Lirette, J. Pouliot, M. Aubin, and M. Larochelle, "The role of electronic portal imaging in tangential breast irradiation: A prospective study," Radiother. Oncol. **37**, 241–245, (1995). [4]

K. Luchka, R. Rajapakshe, and S. Shalev, "Quality Asuurance of EPI Systems," Proc. 7th. Int. Workshop on Electronic Portal Imaging, Vancouver, 8-11, (2002). [93]

B. M. C. McCurdy, K. Luchka, S. Pistorius, "Dosimetric investigation and portal dose image prediction using an amorphous silicon electronic portal imaging device," Med. Phys. **28**, 911-924, (2001).

[7,46,50,89,109]

T. R. McNutt, T. R. Mackie, P. Reckwerdt, and B. R. Paliwal, "Modeling dose distributions from portal dose images using the convolution/superposition method," Med. Phys. **23**, 1381–1392, (1996). [55]

T. R. McNutt, T. R. Mackie, P. Reckwerdt, and N. Papanikolaou, "Calculation of portal dose distributions from portal dose images using the convolution/superposition method," Med. Phys. **23**, 1381-1392, (1996).

[51,128]

H. Meertens, M. van Herk, J. Bijhold, and H. Bartelink, "First clinical experience with a newly developed electronic portal imaging device," Int. J. Radiat. Oncol. Biol. Phys. **18**, 1173-1181, (1990). [95]

Y. E. Mohri, L. E. Antonuk, J. Yorkston, K. –W. Jee, M. Maolinbay, K. L. Lam, and J. H. Siewerdsen, "Relative dosimetry using active matrix flat-panel imager (AMFPI) technology," Med. Phys. **26**, 1530-1541, (1999). [109]

R. H. Morgan, and R. E. Sturm, "The Johns Hopkins fluoroscopic screen intensifier," Radiology. **57**, 556-560, (1951). [6]

J. W. Motz, and M. Danos, "Imaging information content and patient exposure," Med. Phys. **5**, 8-22, (1978). [38,39,45]

C. Mitine, A. Dutreix, and E. van der Schueren, "Black and white in accuracy assessment of megavoltage images: The medical decision is often gray," Radiother. Oncol. **28**, 31–36, (1993). [4]

C. Mitine, A. Dutreix, and E. van der Schueren, "Tangential breast irradiation: Influence of technique of set-up on transfer errors and reproducibility," Radiother. Oncol. **22**, 308–310, (1991). [4]

C. Mitine, G. Leunens, J. Verstraete, N. Blanckaert, J. Van Dam, A. Dutreix, and E. van der Schueren, "Is it necessary to repeat quality control procedures for head and neck patients?," Radiother. Oncol. **21**, 201–210, (1991). [48]

P. Munro. *The Modern Technology of Radiation Oncology*, J. Van Dyk Ed (Medical Physics Publishing, Madison, 1999). [15]

P. Munro, "Portal imaging technology: Past, present, and future," Semin. Radiat. Oncol. 5, 115-133, (1995). [4-6,16-18,20,24,25]

P. Munro, and D. C. Bouius, "X-ray quantum limited portal imaging using amorphous silicon flat-panel arrays," Med. Phys. **25**, 689-702, (1998). [89]

P. Munro, J. A. Rawlinson, and A. Fenster, "Therapy imaging: A signal-to-noise analysis of a fluoroscopic imaging system for radiotherapy localization," Med. Phys. **17**, 763–772, (1990). [42,43,54,65]

P. Munro, J. A. Rawlinson, and A. Fenster, "Therapy imaging: Limitations of imaging with high energy x-ray beams," Proc. SPIE. **767**, 178-184, (1987). [42]

B. Nilsson, B. I. Rudén, and B. Sorcini, "Characteristics of silicon diodes as patient dosemeters in external radiation therapy," Radiother. Oncol. **11**, 279–288, (1988). [48]

A. Noel, P. Aletti, P. Bey, and L. Malissard, "Detection of errors in individual patients in radiotherapy by systematic in vivo dosimetry," Radiother. Oncol. **34**, 144–151, (1995). [48]

J. R. Palta, S. Kim, J. G. Li, and C. Liu, "Tolerance limits and action levels for planning and delivery of IMRT," : AAPM 2003 summer school proceedingds, (Medical Physics Publishing, Colarado Springs, 2003). [118]

G. Pang, and J. A. Rowlands, "Electronic portal imaging with an avalanche-multiplication-based video camera," Med. Phys. **27**, 676-684, (2000). [54]

M. Partridge, P. M. Evans, and M. A. Mosleh-Shirazi, "Linear accelerator output variations and their consequences for megavoltage imaging," Med. Phys. **25**, 1443-1452, (1998). [95]

M. Partridge, P. M. Evans, M. van Herk, L. S. Ploeger, G. J. Budgell, and H. V. James, "Leaf position verification during dynamic beam delivery: a comparison of three applications using electronic portal imaging," Med. Phys. **27**, 1601-1609, (2000). [21]

C. R. Perryman, J. D. McAllister, and J. A. Burwell, "Cobalt 60 radiography," Am J Roentgenol. **83**, 525-532, (1960). [5]

J. Rabinowitz, M. Broomberg, K. Goitein, J. McCarthy, and J. Leong, "Accuracy of radiation field alignment in clinical practice," Int. J. Radiat. Oncol., Biol., Phys. **11**, 1857–67, (1985). [4]

T. Radcliffe, G. Barnea, B. Wowk, R. Rajapakshe, and S. Shalev, "Monte Carlo optimization of metal/phosphor screens at megavoltage energies," Med. Phys. **20**, 1161-1169, (1993). [54]

R. Rajapakshe, K. Luchka, and S. Shalev, "A quality control test for electronic portal imaging devices," Med. Phys. **23**, 1237-1244, (1996). [68]

A. Rizzotti, C. Compri, and G. F. Garusi, "Dose evaluation to patients irradiated by 60 Co beams, by means of direct measurement on the incident and on the exit surfaces," Radiother. Oncol. **3**, 279–283, (1985). [48]

A. Rizzotti, G. Anselmo, and G. P. Glasgow, "Multiple simultaneous bilateral urothelial tumours of the renal pelvis," Br. J. Urol. **4**, 312–315, (1987) [48]

D. M. Roback, and B. J. Gerbi, "Evaluation of electronic portal imaging device for missing tissue compensator design and verification," Med. Phys. **22**, 2029-2034, (1995). [95]

D. W. Rogers, "Fluence to dose equivalent conversion factors calculated with EGS3 for electrons from 100 keV to 20 GeV and Photons from 11 keV to 20 GeV," Health Phys. **46**, 891-914, (1984). [42]

S. A. Rosenthal, J. M. Galvin, J. W. Goldwein, A. R. Smith, and P. H. Blitzer, "Improved methods for determination of variability in patient positioning for radiation therapy using simulation and serial portal film measurements," Int. J. Radiat. Oncol., Biol., Phys. **23**, 621–625, (1992). [4]

B. I. Rudén, "Evaluation of the clinical use of TLD," Acta Radiol. Ther. Phys. Biol. **15**, 447-464, (1976). [48]

SEER's Training Web Site. Web page: Introduction To Radiation Therapy 2003 (http://training.seer.cancer.gov/module_cancer_treatment/unit2_radiation1_intro.html). [3]

J. A. Seibert, "Computed Radiography Overview," presented at the Radiological Society Of North America, 84th Scientific Assembly and Annual Meeting, Chicago, (1998). [2,30-33]

S. Shalev, R. Rajapakshe, K. Luchka, *Thechniques for commisioning electronic portal imaging devices,* Proc. XII Int. Conf. on the use of computers in radiation therapy (Medical Physics Publishing, Madison, 1997). [68]

E. B. Springer, L. Pape, F. Elsner, et al., "High-energy radiography (Cobalt 60 and Cesium 137) for tumor localization and treatment planning," Radiology. **78**, 260-262, (1962). [5]

Statistics Canada Web Site. Web Page: Canadian Deaths (http://www.statcan.ca/). [2]

R. L. Stern, B. A. Fraass, A. Gerhardson, D. L. McShan, and K. L. Lam, "Generation and use of measurement-based 3-D dose distributions for 3-D dose calculation verification," Med. Phys. **19**, 165-173, (1992). [56]

R. A. Street, R. B. Apte, S. E. Ready, R. L. Weisfield, and P. Nylen, "Amorphous silicon sensor arrays for x-ray and document imaging," Mater. Res. Soc. Symp. Proc. **487**, 1455-1466, (1997). [27]

R. W. Swain, and R. J. Steckel, "Beam localization in cobalt and megavoltage therapy during treatment," Radiology. **86**, 529, (1966). [5]

W. Swindell, "Transit dosimetry," Brit J. Radiol. **66**, 1077, (1993). [49]

L. J. van Battum, and B. J. M. Heijmen, "Film dosimetry in water in 23 MV therapeutic photon beam," Radiother. Oncol. **34**, 152-159, (1995). [56]

F. Van den Heuvel, W. De Neve, D. Verellen, M. Coghe, V. Coen, and G. Storme, "Clinical implementation of an objective computer-aided protocol for intervention in intra-treatment correction using electronic portal imaging," Radiother. Oncol. **35**, 232–239, (1995). [4]

M. van Herk, "Physical aspects of a liquid-filled ionization chamber with pulsed polarizing voltage," Med. Phys. **18**, 692-702, (1991). [53,85,101]

M. van Herk, J. Bijhold, B. Hoogervorst, and H. Meertens, "Sampling methods for a matrix ionization chamber system," Med. Phys. **19**, 409-418, (1992). [84]

M. van Herk and H. Meertens, "A matrix ionization chamber imaging device for on-line patient setup verification during radiotherapy," Radiother. Oncol. **11**, 369–378, (1988). [42,43,91]

G. van Tienhoven, J. H. Lanson, D. Crabeels, S. Heukelom, and B. J. Mijnheer, "Accuracy in tangential breast treatment set-up: A portal imaging study," Radiother. Oncol. **22**, 317–322, (1991). [4]

Varian Oncology Systems, "Portal Vision aS500 Rel. 6 System Manual, (2000). [25,63]

Varian Oncology Systems, "Portal Vision LC250 Rel. 6 System Manual (2000). [63]

H. Wallman, and N. Stalberg, "A television-roentgen system for pendulum therapy," Br J Radiol. **31**, 576-577, (1958). [6]

C. Weltens, G. Leunens, A. Dutreix, J. Cosset, F. Eschwege, and E. van der Schueren, "Accuracy in mantle field irradiations: Irradiated volume and daily dose," Radiother. Oncol. **29**, 18–26, (1993). [4]

A. B. Wolbarst, *Physics Of Radiology* (Appleton & Lange, East Norwalk, 1993). [1,2]

J. W. Wong, E. D. Slessinger, R. E. Hermes, C. J. Offutt, T. Roy, and M. W. Vannier, "Portal dose images I: Quantitative treatment plan verification," Int. J. Radiat. Oncol. Biol. Phys. **18**, 1455–1463, (1990). [49,51,54]

B. Wowk, and S. Shalev, "Thick phosphor screens for on-line portal imaging," Med. Phys. **21**, 1269-1276, (1994). [18,42]

B. Wowk, S. Shalev, and T. Radcliffe, "Grooved phosphor screens for on-line portal imaging," Med. Phys. **20**, 1641-1651, (1993). [54]

F. F Yin, M. C. Schell, and P. Rubin, "A technique of automating compensator design for lung inhomogeneity correction using an electronic portal imaging device," Med. Phys. **21**, 1729–1732, (1994). [49]

F. F. Yin, M. C. Schell, and P. Rubin, "Input/output characteristics of a matrix ion-chamber electronic portal imaging device," Med. Phys. **21**, 1447-1454, (1994). [46,95,102]

X. Ying, L. Y. Geer, and J. W. Wong, "Portal dose images II: Patient dose estimation," Int. J. Radiat. Oncol. Biol. Phys. **18**, 1465–1475, (1990). [49]

Y. Zhu, X. Q. Jiang, and J. Van Dyk, "Portal dosimetry using a liquid ion chamber: Dose response studies," Med. Phys. 22, 1101-1106, (1995). [46,53]